

Instrumentation, Control, and Testing of a Small Wind Turbine Test Rig

by

Iman Khorsand Asgari  
BSc, Ferdowsi University of Mashhad, 2011

A Thesis Submitted in Partial Fulfillment  
of the Requirements for the Degree of

MASTER OF APPLIED SCIENCE

in the Department of Mechanical Engineering

© Iman Khorsand Asgari, 2015  
University of Victoria

All rights reserved. This thesis may not be reproduced in whole or in part, by photocopy  
or other means, without the permission of the author.

## **Supervisory Committee**

Instrumentation, Control, and Testing of a Small Wind Turbine Test Rig

by

Iman Khorsand Asgari  
BSc, Ferdowsi University of Mashhad, 2011

### **Supervisory Committee**

Dr. Curran Crawford (Department of Mechanical Engineering)  
**Supervisor**

Dr. Peter Wild (Department of Mechanical Engineering)  
**Departmental Member**

## Abstract

### **Supervisory Committee**

Dr. Curran Crawford (Department of Mechanical Engineering)

Supervisor

Dr. Peter Wild (Department of Mechanical Engineering)

Departmental Member

As a cost-effective test method, a vehicle-based test rig can be utilized in small wind turbine experimental work to facilitate turbine performance tests under a range of controlled wind speeds, as well as to validate turbulent flow models. The instrumentation of a custom trailer-based mobile wind turbine test rig has been modified to provide a platform for full rotor speed control. A control system coupled to an electric vehicle controller with regenerative braking technology was developed in five steps, namely: system modeling in Simulink, system identification, control system design and analysis, control system implementation in LabVIEW, and Proportional-Integral-Derivative (PID) controller tuning in real-time. A custom Graphical User Interface (GUI) was also developed. Furthermore, a Computational Fluid Dynamics (CFD) analysis was conducted to assess the potential impact of towing vehicle's disturbance on the free stream available to the rotor disc. This trailer rig will allow up to a 1kW wind turbine. It can be towed behind a vehicle to conduct steady state tests or it can be parked in an open area to collect unsteady field data. It has been tested in a towed scenario and the Blade Element Momentum (BEM) predictions were compared with the obtained aggregate performance curve.

## Table of Contents

Supervisory Committee .....	ii
Abstract .....	iii
Table of Contents .....	iv
List of Tables .....	vii
List of Figures .....	viii
Acknowledgments .....	x
Dedication .....	xi
Chapter 1. Introduction .....	1
1.1 Wind Turbine Technology .....	1
1.2 Background on Small Wind Turbine Testing .....	3
1.3 Thesis Objectives and Contributions .....	8
1.4 Thesis Overview .....	9
Chapter 2. Trailer-based Small Wind Turbine Test Rig .....	10
2.1 System Description .....	10
2.2 Sensors .....	14
2.2.1 Multi-axial Loadcell .....	15
2.2.2 Ultrasonic Anemometer .....	15
2.2.3 Cup Anemometer .....	17
2.2.4 Wind Direction Vane .....	18
2.2.5 Barometric Pressure Sensor .....	20
2.2.6 Temperature and Relative Humidity Probe .....	21
2.2.7 Incremental Encoders .....	22
2.3 Electrical System .....	23
2.3.1 Main Motor and Controller .....	23
2.3.2 Battery Bank and Converters .....	25
2.3.3 Dump Load Controller .....	26
2.4 Data Acquisition System .....	27
2.4.1 National Instruments CompactRIO Controller .....	29
2.4.2 National Instruments CompactRIO Chassis .....	30
2.4.3 National Instruments I/O Modules .....	31
2.5 System Integration .....	31
Chapter 3: Operating Parameters and Uncertainty Analysis .....	33
3.1 Uncertainty and Error Types .....	33
3.2 Methods .....	34
3.2.1 Statistical Summary .....	35
3.2.2 Precision (Random) Uncertainty .....	37
3.2.3 Bias (Systematic) Uncertainty .....	37
3.2.4 Total Uncertainty .....	38
3.3 Data Acquisition System Uncertainty Analysis .....	38
3.4 Sample Data for Initial Uncertainty Analysis .....	41
3.5 Uncertainty in Measurable Parameters .....	43
3.5.1 Torque, Thrust, Pitching, and Yawing Moments .....	43
3.5.2 Cup Wind Speed .....	48
3.5.3 Ultrasonic Measurands .....	50
3.5.4 Vane Wind Direction .....	51

3.5.5 Temperature and Relative Humidity (RH).....	51
3.5.6 Pressure.....	53
3.5.7 Rotor Speed.....	54
3.6 Uncertainty Propagation in the Final Results (Calculable Parameters).....	55
3.6.1 Power.....	56
3.6.2 Air Density.....	57
3.6.3 Power Coefficient.....	61
3.6.4 Thrust Coefficient.....	63
3.6.5 Tip speed ratio (TSR).....	64
3.7 Uncertainty Analysis Summary.....	65
Chapter 4: Wind Turbine Controls.....	69
4.1 Basics of Wind Turbine Control.....	70
4.1.1 Rotor Speed Choices: Fixed- and Variable-Speed.....	70
4.1.2 Power Curve and Control Regions.....	71
4.2 Power Control Methods.....	72
4.2.1 Passive Stall Control.....	73
4.2.2 Active Pitch Control.....	73
4.2.3 Passive Pitch Control.....	74
4.2.4 Active Stall Control.....	75
4.2.5 Yaw Control.....	75
4.3 Braking Systems.....	75
4.4 Test Rig Control System.....	76
4.5 System Modeling in Simulink.....	79
4.5.1 Turbine Simulink Model.....	79
4.5.2 Rotor Inertia Measurement using Bifilar Pendulum Test.....	83
4.6 System Identification.....	85
4.6.1 Speed Ramp-up and Coast-down Data Collection for Identification.....	87
4.6.2 Torque-voltage Slope Identification using a Clamp Ammeter.....	90
4.7 Control System Design and Analysis.....	91
4.7.1 Control Objectives.....	91
4.7.2 Generator Torque Control using a PI Controller.....	92
4.7.3 Combined Drivetrain and Torque Controller Simulink Model.....	93
4.9 LabVIEW-based Controller Tuning in Real-Time.....	99
Chapter 5: 3D CFD Simulation of the Testing Platform in ANSYS.....	103
5.1 CFD Simulation Objectives.....	103
5.2 Background.....	103
5.3 Theoretical Model.....	105
5.4 Computational Domain and Geometry.....	106
5.5 Boundary Condition and Grid Layout.....	107
5.6 Results and Discussions.....	110
Chapter 6: Controlled Velocity Track Tests.....	114
6.1 Test Site and Weather Conditions.....	114
6.2 Test Method.....	115
6.3 Test Results and Discussions.....	117
Chapter 7: Conclusion and Recommendations.....	127
7.1 Conclusion.....	127

7.2 Recommendations for Future Work ..... 128

Bibliography ..... 131

Appendix ..... 137

    Appendix A. Loadcell Crosstalk Data and Certificate of Test and Calibration ..... 137

    Appendix B. Test Rig Operational Work Instructions ..... 144

        B.1 LabVIEW Graphical User Interface (GUI) Work Instruction ..... 144

        B.2 Control Cabinet (CTRL) Interface Work Instruction..... 149

## List of Tables

Table 1. Technical features of the test rig .....	13
Table 2. Measurands and sensors.....	14
Table 3. Custom ultrasonic anemometer output code elements .....	17
Table 4. DC/DC converters.....	26
Table 5. Data acquisition system components .....	29
Table 6. NI 9237 uncertainty [49].....	39
Table 7. NI 9201 uncertainty (noise excluded) [50] .....	40
Table 8. NI 9263 uncertainty [51].....	41
Table 9. Uncertainty of NI CRIO modules .....	41
Table 10. Sample test run timed loop measured and calculated data.....	42
Table 11. Sample test run timed loop and serial data for air density calculation.....	42
Table 12. Sample test run serial ultrasonic data.....	42
Table 13. Generic multi-axial loadcell specifications [21] .....	43
Table 14. Custom loadcell specifications [Appendix A] .....	45
Table 15. Cross-talk raw data [Appendix A] .....	45
Table 16. Cross talk performance (% full scale output).....	45
Table 17. Ultrasonic anemometer uncertainty .....	50
Table 18. Relative humidity and temperature uncertainty [33] .....	52
Table 19. Multi-plate radiation shield uncertainty [34] .....	52
Table 20. Pressure sensor uncertainty [32] .....	53
Table 21. CIPM-2007 constants [57] .....	59
Table 22. SD-based uncertainty analysis summary .....	66
Table 23. SEM1-based uncertainty analysis summary .....	67
Table 24. SEM2-based uncertainty analysis summary .....	67
Table 25. Rotor inertia bifilar pendulum test results .....	84
Table 26. AC phases current measurement data.....	90
Table 27. Comparison of PID gains in LabVIEW and Simulink .....	97
Table 28. PID effects on a closed-loop system response [73] .....	100
Table 29. Nominal targets of track test runs .....	116

## List of Figures

Figure 1. Conceptual layout of a modern wind turbine [2].....	3
Figure 2. Small wind turbine testing methods .....	6
Figure 3. SSDL's test rig from concept to realization.....	10
Figure 4. Metric geometry of the test rig [19] .....	11
Figure 5. Tower top assembly [19].....	12
Figure 6. Custom 3D printed nacelle .....	13
Figure 7. Multi-axial loadcell [21].....	15
Figure 8. Time of flight theory [23].....	16
Figure 9. Ultrasonic anemometer [24].....	16
Figure 10. Cup anemometer [26].....	18
Figure 11. Wind vane alignment [28] .....	19
Figure 12. NRCan's magnetic declination calculator [29].....	19
Figure 13. Wind direction vane [31].....	20
Figure 14. Barometric pressure sensor [32].....	21
Figure 15. Temperature and relative humidity probe [33].....	21
Figure 16. Hollow shaft encoder [35].....	22
Figure 17. Shaft encoder output signal schematic [35].....	22
Figure 18. Main motor and controller [39].....	23
Figure 19. Battery and charger.....	25
Figure 20. Dump load controller.....	26
Figure 21. Slew drive and DC motor.....	27
Figure 22. National Instruments data acquisition system .....	28
Figure 23. CompactRIO reconfigurable embedded system architecture .....	28
Figure 24. NI CRIO controller.....	30
Figure 25. Reconfigurable FPGA chassis .....	30
Figure 26. System integration .....	31
Figure 27. Graphical user interface of the test rig .....	32
Figure 28. Loadcell offset null in LabVIEW .....	46
Figure 29. Aerodynamic torque schematic .....	56
Figure 30. Performance curve for a modern three-blade turbine [56] .....	71
Figure 31. Power curve of a variable-speed wind turbine [62].....	72
Figure 32. Power curve comparison of 1.5 MW rated machines [56].....	74
Figure 33. Custom control system development flow chart .....	77
Figure 34. Mass-spring passive pitch control .....	78
Figure 35. Turbine Simulink model.....	80
Figure 36. Rotor aerodynamics subsystem .....	81
Figure 37. LSS One-mass (lumped) drivetrain dynamics subsystem .....	82
Figure 38. Torque controller subsystem .....	82
Figure 39. Tower dynamics subsystem.....	83
Figure 40. Bifilar pendulum test of the rotor .....	85
Figure 41. Throttle path ramp-up VI for system identification .....	88
Figure 42. Regeneration path coast-down raw test results .....	88
Figure 43. Comparison of the grey box model and the measured data.....	89
Figure 44. Torque-voltage slope identification using a clamp ammeter .....	90

Figure 45. Simulink PID block .....	93
Figure 46. Drivetrain and torque controller Simulink model .....	93
Figure 47. PI controller performance in steady and unsteady wind inflows .....	94
Figure 48. Steady and unsteady wind inflows .....	95
Figure 49. Closed-loop control system block diagram in LabVIEW .....	99
Figure 50. Control system performance at rated rotor speed.....	101
Figure 51. Regenerative braking and throttle torque actuation during towed test run ...	102
Figure 52. Ahmed vehicle model [74] .....	104
Figure 53. Simple tow vehicle model .....	106
Figure 54. Computational domain .....	107
Figure 55. Boundary condition and grid layout .....	108
Figure 56. Unstructured Octree mesh .....	109
Figure 57. Velocity contour .....	110
Figure 58. Pressure contour .....	111
Figure 59. Wind velocity ratio profile at the turbine rotor .....	112
Figure 60. Test site.....	114
Figure 61. Controlled velocity track tests (towed scenario) .....	116
Figure 62. A full track test raw measured data at 50 Hz.....	119
Figure 63. A full track test calculated power data .....	120
Figure 64. Average wind speed, torque, rotor speed, and thrust .....	121
Figure 65. Average power.....	122
Figure 66. Total uncertainty bounds in mean power coefficient vs tip speed ratio .....	122
Figure 67. Power coefficient vs. tip speed ratio performance curve .....	123
Figure 68. Uncertainty components of the power coefficient measurement .....	125
Figure 69. Uncertainty components of the tip speed ratio measurement.....	125
Figure 70. Producer/consumer loop one .....	146
Figure 71. Producer/consumer loop two.....	148
Figure 72. Producer/consumer loop three.....	148
Figure 73. Control cabinet interface .....	150

## **Acknowledgments**

First and foremost I would like to sincerely thank my supervisor Dr. Curran Crawford, for his guidance, patience, and support throughout this learning process. His teachings helped me to understand the theoretical aspects of the research work while developing a practical engineering approach to solve the technical problems systematically.

I would also like to extend my thanks to Alan Magni, Patrick Chang, Michael McWilliam, Michael Shives, Oliver Pirquet, Stefan Kaban, Kevin Andersen, Ryan Dunbar, Pouya Amid, and all my other colleagues at the University of Victoria's Institute for Integrated Energy Systems (IESVic) and the Sustainable Systems Design Laboratory.

## **Dedication**

To my parents, Maryam and Hamid, who shed the brightest light on my journey.

## **Chapter 1. Introduction**

As a controlled velocity testing method, a trailer-based small wind turbine test rig can be utilized to provide prototype testing of a developed small wind energy system as well as to validate design and analysis tools used to assess the turbine performance analytically.

The instrumentation of a trailer-based small wind turbine test rig developed at the University of Victoria's Sustainable Systems design Laboratory (SSDL), a member laboratory of the Institute for Integrated Energy Systems (IESVic), was completed. A speed control system was designed, analyzed, and tested. Utilizing this control system, the test rig was tested as a platform for real-time speed control as well as to conduct turbine performance assessment. The functionality of the whole system and safety cautions were also verified.

In this chapter, a brief background on wind turbine technology will be presented in 1.1. Methods of small wind turbine testing will be discussed in 1.2. Subsequently, the objectives and an overview of this thesis will be outlined in 1.3 and 1.4 respectively.

### **1.1 Wind Turbine Technology**

Wind energy has been harnessed beginning thousands of years ago by humans. Primarily, it was utilized to directly do mechanical work by propelling boats around the Nile River, grinding grain in Persia (where the first vertical-axis windmills were built), and pumping water (irrigation and drainage) in China [1]. In contrast to windmills which convert the energy in the wind into mechanical energy, in a modern wind turbine, the kinetic energy in the wind is initially converted to mechanical energy by the rotor blades and then into electric energy by the generator.

Wind turbine technology has evolved throughout the years. Several factors has influenced the pace of its technological (r)evolution such as the global awareness regarding the finiteness of fossil fuels, advert impacts of using such sources to deliver energy services on climate change, and a need to provide energy security (e.g. following the oil crises of the 1970's).

Wind turbines can be classified according to various criteria. They can be categorized based on their size (see 1.2), their operational speed, whether fixed or variable speed (see Chapter 4), and their architecture in terms of their axis of rotation with respect to the ground. In a Horizontal Axis Wind Turbine (HAWT), the axis of rotation is parallel to the ground as opposed to a Vertical Axis Wind Turbine (VAWT) in which the axis of rotation is perpendicular to the ground. They can also be classified based on their applications, whether it is on-shore or off-shore, grid-connected or stand-alone, etc. Modern three-bladed Danish-style HAWTs are the most common industrial wind turbines in use today. Typical components of such a MW-scale HAWT are illustrated in Figure 1 [2].

Today it is apparent that to address the global energy challenges that lay ahead, a transition from carbon-intensive energy systems towards low-carbon energy systems, such as wind, is inevitable. As part of the emerging global shift in energy systems, wind power has played – and will likely continue to play – an integral role. Indeed, according to Global Wind Energy Council (GWEC), the deployment of wind power has more than tripled since 2007, surpassing 318 GW of cumulative installed capacity [3]. Wind energy development had a record year in Canada through adding 1.6 GW of new installed capacity in 2013, ranking fifth globally [4]. As of July 2014, Canada's installed capacity was 8.52 GW, supplying approximately 3 % of the national electricity demand [4].

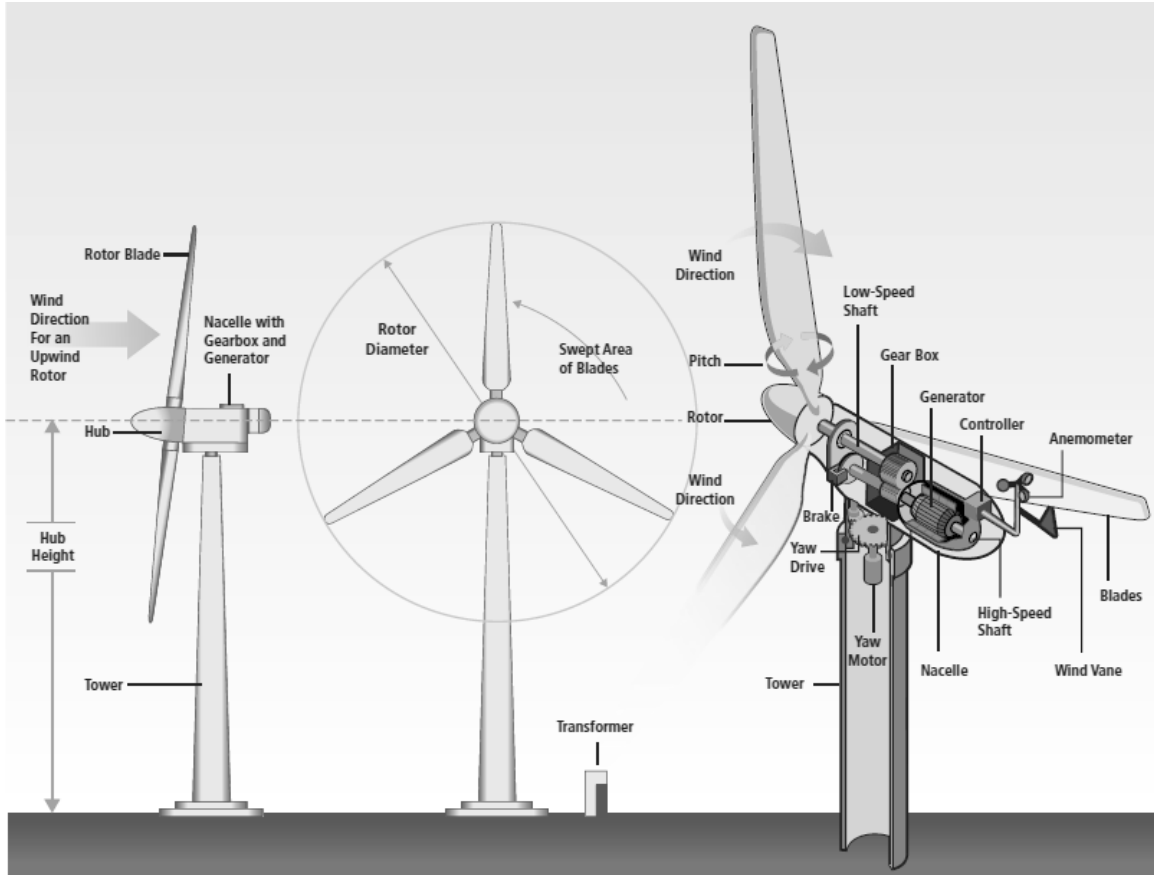


**Figure 1.** Conceptual layout of a modern wind turbine [2]

## 1.2 Background on Small Wind Turbine Testing

There is no fixed definition of what constitutes the size of a wind energy system (i.e. small-scale versus utility-scale systems), applicable to various jurisdictions. Regarding the wind turbine size designation, the third edition of the International Electrotechnical Commission (IEC) 61400-2 titled: “Wind Turbines – Part 2: Small wind turbines”, defines a small wind turbine as a turbine with a swept area smaller than or equal  $200 \text{ m}^2$ , corresponding roughly to less than 50 kW of power capacity rating (generating electricity at a voltage below 1000 V AC or 1500 VDC) for both on-grid and off-grid applications [5]. The American Wind Energy Association (AWEA) and Canadian Wind Energy Association (CanWEA) on the other hand, consider wind turbines with a capacity rating

of less than or equal to 100 kW and 300 kW, as small, respectively [6], [7]. Although there exist subdivisions to these definitions, the term small wind turbine will be used based on the IEC 61400-2 standard throughout this document.

Small wind energy systems have a broad range of applications both off-grid (for a battery storage system, sailboat, gulf kart, RV, cottage, home, farm, business, remote community, or remote station) and on-grid (for a cottage, home, farm, or business) [7]. While not limited to small wind turbines, the term distributed wind is used in terms of technology application based on a wind project's location relative to end-use and power-distribution infrastructure, rather than by technology or project sizes [8].

Compared to the technology developed for large wind turbines, small wind turbine technology is rather in its infancy. As wind turbine design and analysis tools, including the most commonly used Blade Element Momentum (BEM) which mathematically evaluates the performance of a turbine, have been primarily developed for utility-scale wind turbines, they need to be compared to test data to investigate the level of their accuracy in small HAWT performance prediction in reality and to implement required modifications accordingly. This model validation can be subsequently used in the standard-based certification process and finally commercialization of the product. The IEC 61400-2 (Ed. 3) provides detailed procedure to characterize the turbine type through various tests such as the tests to verify design data, mechanical loads testing, duration testing (reliable operation, dynamic behaviour, and reporting of duration test), mechanical component testing, safety and function, electrical, and environmental testing [5]. The IEC 61400-12-1 (Ed.1), titled: "Wind turbines - Part 12-1: Power performance measurements of electricity producing wind turbines" specifies a procedure to determine

the power performance characteristics of a single wind turbine and applies to the testing of wind turbines of all types and sizes connected to the electrical power network [9]. This standard also describes a procedure to be used for measuring the power performance characteristics of small wind turbines (as defined in IEC 61400-2) when connected to either the electric power network or a battery bank [9].

In the literature, three main methods have been identified to be used to acquire small HAWT experimental data, namely: field testing, wind tunnel testing, and track testing. The latter method can also be referred to as controlled-velocity, vehicle-based or trailer-based testing. As an example, field testing of a 10 kW National Renewable Energy Laboratory (NREL) small wind research turbine, which is a modified Bergey placed at the National Wind Technology Center (NWTC) in Colorado, is illustrated in Figure 2 (a) [10]. Figure 2(b) depicts a wind tunnel experimental set-up at the BLWT2 large wind tunnel facility located at the University of Western Ontario [11]. Figure 2(c) shows a track testing of a 1 kW Airdolphin small wind turbine in Japan [12].

Field testing, in which the wind turbine is installed on a tower and placed in a site to collect unsteady data over a period of up to a couple of months, is the best and the most reliable method to characterize small wind turbines. Although field testing assesses the actual unsteady performance, it takes the longest time to complete as testing in all wind speeds must be conducted in free air naturally [13].

Wind tunnel testing has the capability of steady state testing in a range of precisely controlled wind speeds in a short period. Assuming that negative aerodynamic issues induced by the wind tunnel walls (e.g. solid blockage) are mitigated, this method of

testing can still be expensive for small wind turbine testing. As a dynamically equivalent alternative for wind tunnel testing, track testing is a cost-effective method which also has the capability of conducting controlled-speed runs to collect experimental data in a short period. In this method, the turbine moves through the fluid, in contrast to the fluid moving around the turbine as is the case in wind tunnel testing [12], [14]-[19].

The choice of which controlled-velocity method to adopt depends on the application and its resources. Track testing is cheap, free of negative boundary layer effects, but its accuracy in velocity control is less than the case of using a wind tunnel. Moreover, road conditions and associated vibrations can impact the accuracy of the collected data when track testing. While being a more robust method, wind tunnel testing is expensive to test a full-scale small wind turbine.

The key point is that the rationale behind utilizing either track testing (towed scenario), or wind tunnel test results, is to obtain the simplest possible comparison data for analysis codes and design validations. Ultimately, the purpose of field testing of the test rig under study will be to achieve a nuanced understanding of the unsteady performance.



(a) Field testing [10]

(b) Wind tunnel testing [11]

(c) Track testing [12]

**Figure 2.** Small wind turbine testing methods

The track testing (controlled-velocity) results of an NREL's 8 kW turbine developed in response to the U.S. Department of Energy's small wind turbine program, was reported in [14]. In general, the turbine needs to be protected in high winds to prevent potential structural damage as well as the generator overheating. As a century-old passive control scheme, furling was used to limit the rotor over speeds [14]. Furling mechanism simply pivots the rotor out of wind physically once a certain rotor speed is reached. According to [14], despite a long history of field experience of furling machines, industry's analytical basis for furling was practically unavailable at the time and some issues arose in the testing procedure. The turbine used in NREL's experiment was designed for battery charging purposes and the generator control design utilized peak power coefficient tracking developed at NREL for small turbine applications explained in [14].

As shown in Figure 2(c), 1 kW Airdolphin was another case of track testing. The rotor and generator in this case were protected against overspeeding utilizing both aerodynamic stall regulation and electromagnetic braking function, producing power output under high wind speed ranges without any shutdown action [12]. When placed in a field test, this turbine survived under a typhoon condition at the Fukushima site where the maximum gust recorded was 47.4 m/s [12]. As for the yaw mechanism, this turbine used a swing rudder system, a fish tail like mechanism capable of reacting to quick changes in wind directions and increased output power [12]. Track testing was also utilized in [15] where a 1 kW Bergey turbine was tested using the furling as the over speed protection mechanism. More cases of using track testing method can also be found in [14], [16]-[19].

### 1.3 Thesis Objectives and Contributions

To facilitate small wind turbine experimental work, a custom trailer-based small wind turbine test rig has been designed and developed in-house, at the University of Victoria's SSDL. The design and development phase of this test rig was mostly completed prior to the current study. However, there was no main software application to interface the system, particularly to control the rotor speed reliably. Moreover, there were components required to be tested, programmatically modified and integrated (e.g. multi-axial loadcell and ultrasonic anemometer), and adequately characterized (e.g. electric vehicle controller) to meet the desired functionality. The main objectives of the present research work were to transform the developed test rig into a safe, functional system, and to test it for the very first time in a steady state scenario to assess the turbine performance. The contributions of this thesis to meet these objectives were sixfold:

1. the instrumentation of the test rig was modified and a custom, extensible, software application coupled to a Graphical User Interface (GUI) was developed, ensuring that all the integrated subsystems function properly as they interact in the context of the whole system,
2. a thorough analysis was conducted to quantify the uncertainty associated with the experimental measurements,
3. a control system was designed and implemented to facilitate full variable-speed control in real-time,
4. a Computational Fluid Dynamics (CFD) analysis was conducted to assess the potential impact of towing vehicle's disturbance on the free stream available to the rotor disc,

5. the system was tested in real-time to ensure safe operation and to verify the functionality of the control mechanisms,
6. a post-processing program was developed to assess the turbine by constructing the aggregate performance curve.

This test rig can now be used as a platform for full variable-speed control by utilizing its advanced instrumentation including the multi-axial loadcell, the ultrasonic anemometer, and the custom speed control system, making it unique compared to other vehicle-based test rigs in the literature (e.g. over speed protection utilizing regenerative braking technology and an active yaw mechanism rather than typically used furling mechanism). The significance of this test rig in small wind turbine testing application is that it not only has the capability of conducting steady state experiments over a range of wind speeds, but also it can be parked as a stand-alone turbine in a field to collect unsteady data.

#### **1.4 Thesis Overview**

First, the trailer-based small wind turbine test rig will be described in details in Chapter 2. Subsequently, operating parameters will be formulated and a thorough uncertainty analysis, incorporating both bias and precision uncertainty components, will be presented in Chapter 3. At the heart of this thesis, upon reviewing basics of wind turbine controls, the developed custom GUI and control system will be discussed in Chapter 4. The CFD study on the wake region behind the towing vehicle will then be covered in Chapter 5. Next, the results of the very first set of steady state controlled velocity track (towed) tests will be discussed in Chapter 6, in which the final aggregate performance curve of the turbine will be presented. Finally, in Chapter 7, the conclusion and recommendations for the future work will be outlined.

## Chapter 2. Trailer-based Small Wind Turbine Test Rig

In this chapter, the instrumentation of the small wind turbine test rig will be explained. The evolution of the project from a conceptual model in 2010 to the very first time track testing in 2014 is illustrated in Figure 3. From the design code used to manufacture the rotor blades to the implemented full variable-speed control system, this custom test rig has been developed in-house, at the SSDL. It can facilitate two test scenarios of steady (towed) and unsteady (stationary).

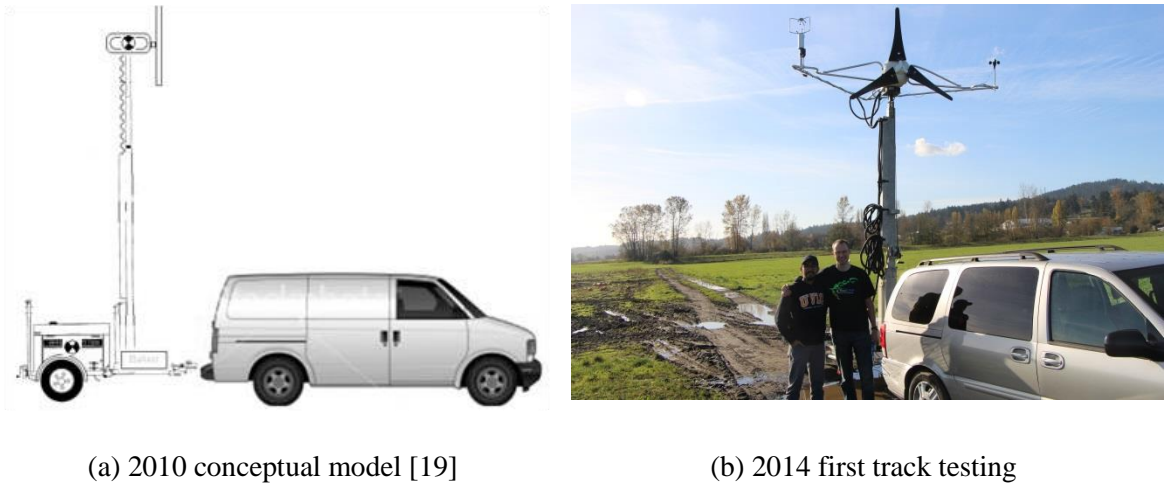
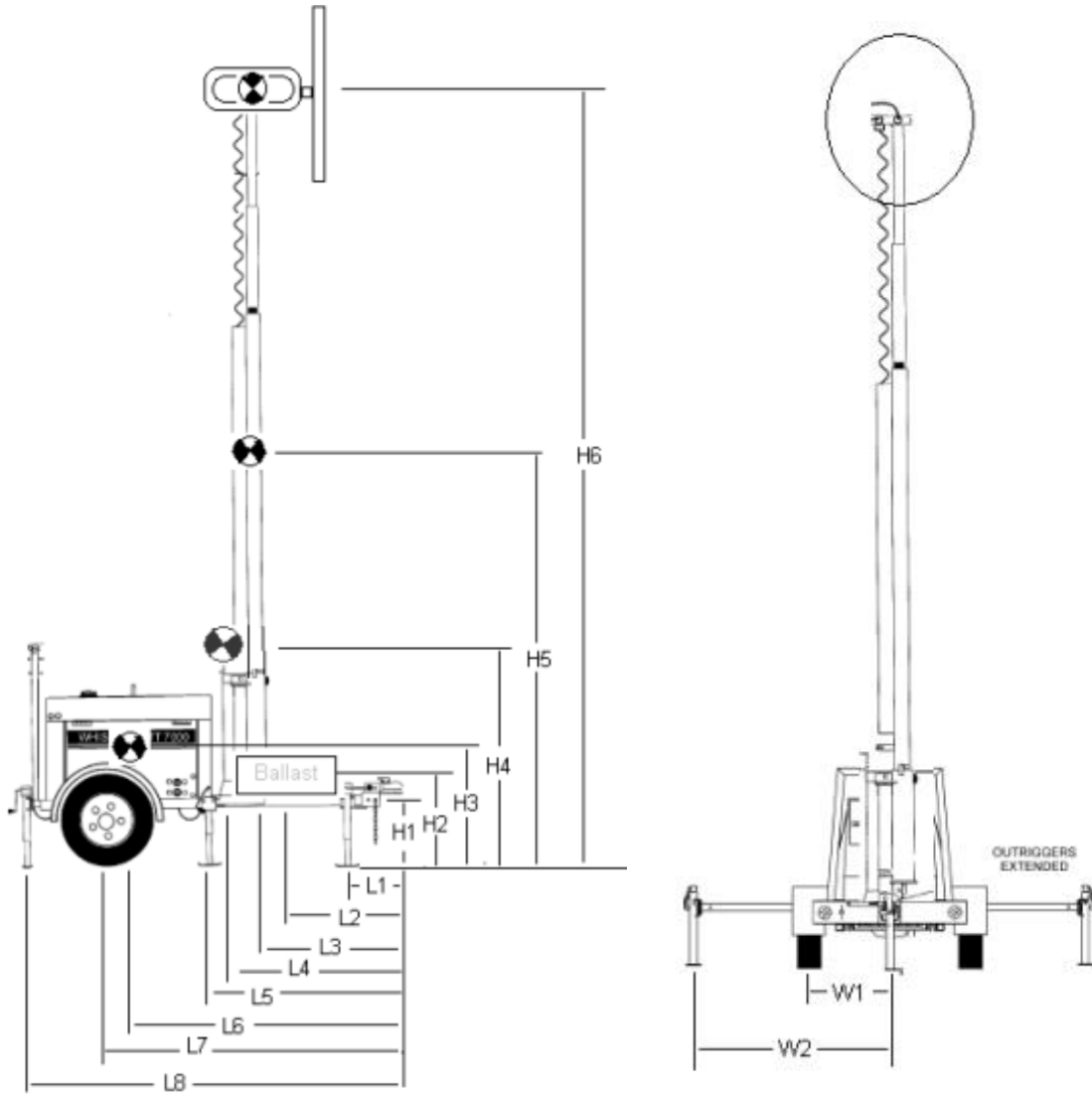


**Figure 3.** SSDL's test rig from concept to realization

### 2.1 System Description

As the foundation of the test rig, a trailer consists of a bed and erectable telescoping tower that can be raised up to a maximum of 9 m was used. The test rig's dimensional information is presented in Figure 4 [19]. Applications of this test rig are twofold: (1) as an alternative to a wind tunnel, it can be towed behind a vehicle to conduct steady state controlled-velocity experiments and (2) it can be parked in a field to collect data.

Shown in Figure 5, the tower top assembly consists of an AmpAir 600 rotor, a shaft encoder, a multi-axial loadcell, a permanent magnet AC generator coupled with a 5:1 planetary gear head, wind sensor, a slew drive, and a DC motor. In contrast to small wind turbines of this size that generally use a passive furling mechanism, this test rig is equipped with the instrumentation required to implement an active yaw mechanism.



H1	H2	H3	H4	H5	H6	L1	L2	L3	L4	L5	L6	L7	L8	W1	W2
(m)															
0.41	0.71	0.56	1.58	4.98	9.55	0.36	1.27	1.63	1.75	1.22	2.29	2.79	3.05	0.89	1.52

Figure 4. Metric geometry of the test rig [19]

Technical features of the test rig including rotor properties are summarized in Table 1.

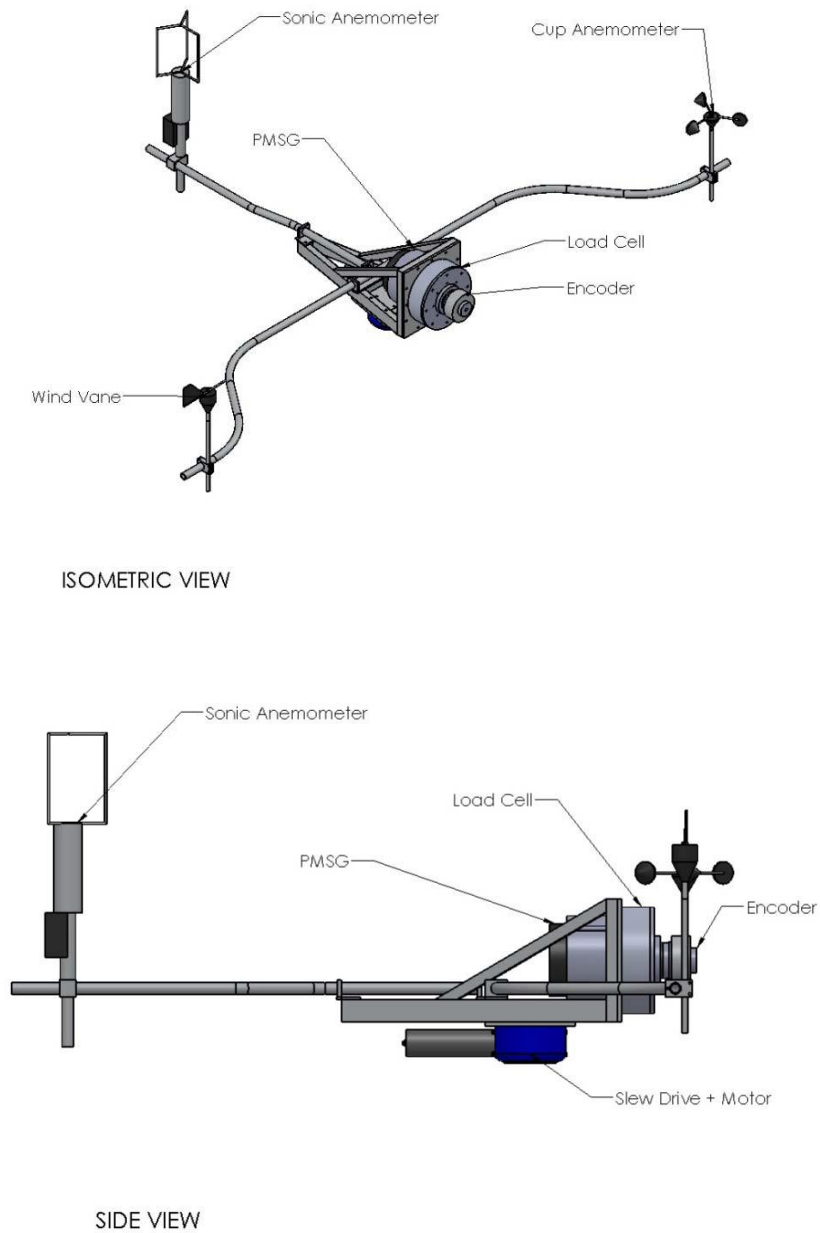


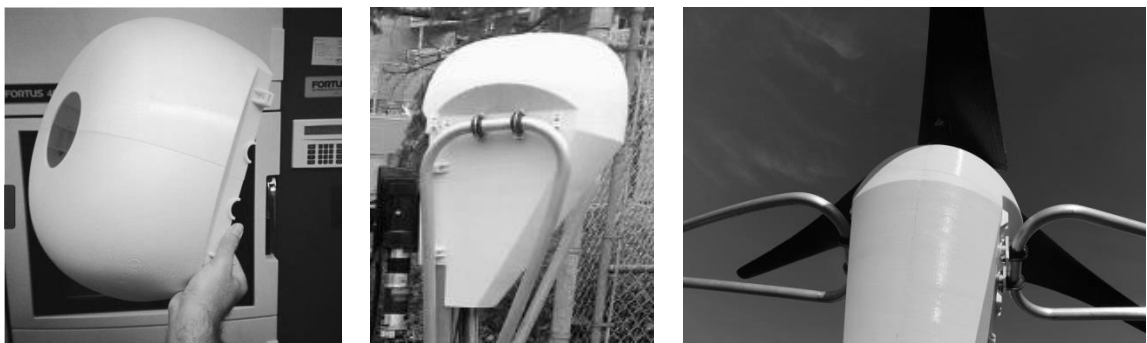
**Figure 5.** Tower top assembly [19]

As depicted in Figure 6, to protect the generator and other instrumentation at the tower head, a polycarbonate nacelle was printed in house, at the SSDL, utilizing the fused deposition modeling (FDM) technology. A Stratasys Fortus 400mc 3D production system [20] was used to print the nacelle in seven pieces.

**Table 1.** Technical features of the test rig.

Item	Feature
Type	Three-bladed, upwind, HAWT, off-grid
Rotor diameter	1.7 m
Hub height	4.5 m to 9 m
Blade material	Glass filled Polypropylene
Weight	16 Kg
Rated power	600 Watts
Cut-in wind speed	3 m/s
Generator	Brushless PMAC
Power/speed controls	Regenerative braking and throttle paired with a LabVIEW-based control system, blade spring-mass pitch control above 13 m/s
Brake	Generator short circuit ('stop' switch), LabVIEW e-stop
Yaw control	Active control using a DC motor and a slew drive

This test rig can be used autonomously using a 48 VDC battery bank protected against overvoltage, overheat, and overcurrent, using a dump load regulator combined with large air resistors and a fuse. An electric vehicle controller was paired with the PMAC generator, and the battery bank. When combined with a custom LabVIEW-based control system (covered in chapter 4), this test rig can be used as a platform for full real-time speed control, utilizing the electric vehicle controller's regenerative braking technology.

**Figure 6.** Custom 3D printed nacelle

## 2.2 Sensors

In this section, information regarding the sensors used on this test rig will be covered.

Manufacturers' specifications references provided under each sensor description can be accessed for more details. As an overview, a list of the measurands and sensors is presented in Table 2. It should be noted that this list includes neither the signals obtained from the electric vehicle controller (which will be recorded using the data acquisition system) nor the automatic battery temperature sensing used for overheat and overvoltage protection, as part of the battery management system.

**Table 2.** Measurands and sensors

Sensor	Measurand	Unit
Young Model 81000 ultrasonic anemometer	Ultrasonic wind speed	m/s
	Wind direction angle	degree
	Wind elevation angle	degree
	Speed of sound	m/s
	Sonic temperature	C°
Young Model 61302V barometric pressure sensor	Pressure	hPa
NRG #40C cup anemometer paired with a #892E interface	Cup wind speed	m/s
NRG #200P wind direction vane	Wind direction angle	degree
IH103 4096 PPR incremental hollow shaft encoder	Rotor rotational speed	rpm
HC2-S3-L temperature and relative humidity probe paired with a Young Model 41003 radiation shield	Temperature	C°
	Relative humidity	%
Novatech F232 multi-axial loadcell	Thrust ( $F_z$ )	N
	Torque ( $T_z$ )	N.m
	Moment ( $M_x$ )	N.m
	Moment ( $M_y$ )	N.m
Midwest 512 PPR optical encoder	Yaw position	degree

### 2.2.1 Multi-axial Loadcell

As shown in Figure 7, a four-axis loadcell made by Novatech Industries was used to measure the aerodynamic forces applied on the rotor, including the thrust force  $F_z$  and three moments  $T_z$ ,  $M_x$ , and  $M_y$ . Detailed manufacturer specifications can be found in [21]. Calibration and cross-talk data provided by the manufacturer is included in Appendix A. Final output power of the turbine can be calculated using the torque reading out of this sensor and the rotor rotational speed reading out of the encoder that will be described in 2.2.7. Full uncertainty analysis that includes all the functional equations, pertinent elemental uncertainties in each measurand, and associated uncertainty propagation in the final results during the data reduction will be discussed in Chapter 3.

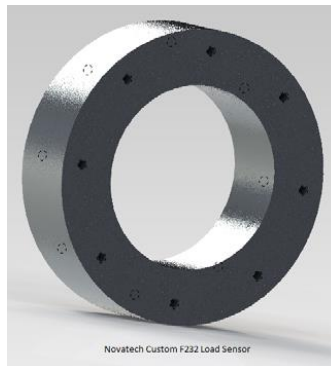


**Figure 7.** Multi-axial loadcell [21]

### 2.2.2 Ultrasonic Anemometer

Ultrasonic anemometers measure the wind velocity based on the transient time of flight of ultrasonic acoustic signals [22]. Transducers on ultrasonic anemometer fire ultrasonic pulses, which are equal in still air and are greater when wind blows in the opposite direction [23]. Based on the variation in the time of flight of the signals along with the path length between the transducers, the wind speed and direction can be calculated by the system [23]. This time of flight theory is illustrated in Figure 8 [23].

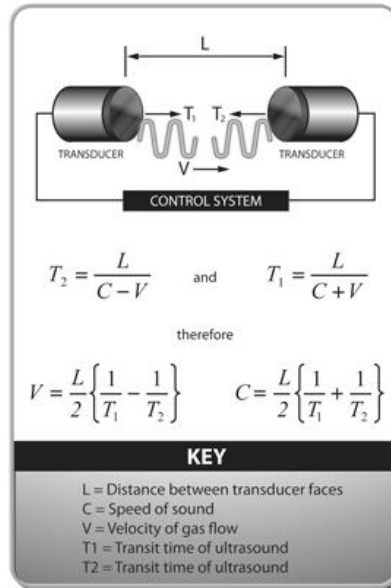


**Figure 8.** Time of flight theory [23]

Shown in Figure 9, as an ideal device for high resolution turbulent investigations and three-dimensional wind measurement, the Young Model 81000 ultrasonic anemometer used on the rig is a 3-axis wind sensor with no moving parts [24]. The sensor resistance to corrosion is enhanced via stainless steel members supporting the three opposing transducers pairs [24]. The speed of sound, which is corrected for crosswind effects, is also used to measure the sonic temperature [22].



**Figure 9.** Ultrasonic anemometer [24]

Custom ASCII (American Standard Code for Information Interchange) serial output format was defined for the device to collect desired data. Moreover, very fine temporal resolution can be obtained via varying the output frequency between 4 and 32 Hz. The anemometer was programmed using a serial communication with a desktop computer in Hyper Terminal. Custom output rate was set to 20 Hz and custom ASCII-printable serial output format was constructed using the code 5789AB as defined in Table 3.

**Table 3.** Custom ultrasonic anemometer output code elements

Code element	Output measurand
5	Orthogonal U, V, and W wind velocities (m/s)
7	3D wind speed (m/s)
8	Wind direction angle (0-360°)
9	Wind elevation angle (-60 to +60°)
A	Speed of sound (m/s)
B	Sonic temperature (C°)

### 2.2.3 Cup Anemometer

The 3-cup anemometer consists of a 3-cup assembly connected to the vertical shaft. Wind pressure is converted to rotational torque through the interaction between incoming wind and the cups' aerodynamic shape (at least one cup always confronts the wind flow) [25]. Subsequently, the rotational movement is converted to an electric signal through the transducer in the anemometer [25]. Demonstrating long-term reliability and calibration stability, NRG #40C 3-cup anemometer, shown in Figure 10, is the most popular cup anemometer for wind resource measurement [25].

This 3-cup anemometer is constructed of rugged Lexan cups molded in one piece for repeatable performance [26]. It has a range of 1 m/s to 96 m/s (2.2 mph to 215 mph). It outputs low level AC sine wave signals with a frequency linearly proportional to wind speed. A #892 Amp Interface could then be used to convert the AC sine wave to a high-

level square-wave signal at the same frequency [27]. Based on the cup anemometer output signal range of 125 Hz, the slope of the transfer function can be calculated as:

$$m = \frac{\text{speed range}}{\text{frequency range}} = \frac{96}{125} = 0.768 \text{ m/s/Hz} \quad (2.1)$$

According to the manufacturer specification [26] however, the slope would be 0.765 m/s/Hz with an offset of 0.35 m/s to formulate a measurable wind speed as:

$$\text{wind speed} \left( \frac{m}{s} \right) = 0.765 \times \text{frequency (Hz)} + 0.35 \quad (2.2)$$



**Figure 10.** Cup anemometer [26]

#### 2.2.4 Wind Direction Vane

Wind direction is measured using a wind vane which typically uses a fin connected to a vertical shaft [25]. Aligning itself into the wind constantly, the wind vane searches for a force equilibrium position mostly using a potentiometer type transducer that outputs an electrical signal corresponding to the position of the vane with respect to a known reference point [25]. Generally, the vane should be oriented to a specified reference point like the true north. In order to align the vane to the true north, Magnetic Declination should be taken into account. Instead of pointing to a true geographic pole, a compass points to a magnetic pole and magnetic declination is this difference between a true geographic bearing and a magnetic bearing [28]. Magnetic declination, which is measured as the number of degrees of bias uncertainty that a compass indicates, varies

over different geographical positions and over time (slightly) in a same position (up-to-date map of declinations should be used) [28]. A magnetic declination of 15 degrees west is depicted in Figure 11 [28].

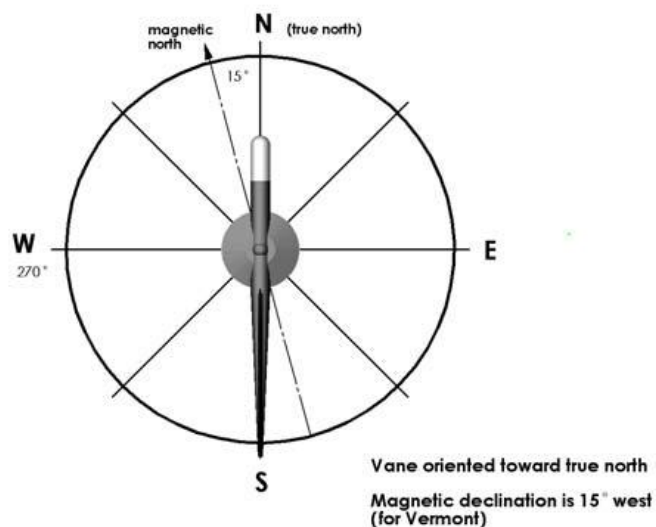


**Figure 11.** Wind vane alignment [28]

Various options are available to calculate the magnetic inclination. As can be seen in Figure 12, using the Natural Resources Canada's magnetic declination calculator, Victoria's magnetic declination can be calculated to be 16 degrees east [29], which means the compass shows 16 degrees east of the true north. When using the test rig in a towed scenario, the vane can be aligned to the trailer itself.



**Figure 12.** NRCan's magnetic declination calculator [29]

Due to its simple design and low maintenance requirements, the NRG #200P, shown in Figure 13, is a popular and industry standard wind vane sensor [25]. This sensor is a 360° mechanical continuous rotation potentiometric vane which measures wind direction relative to the orientation of the fixed base on the sensor (the vane is directly connected to a precision conductive plastic potentiometer located in the main body) [31]. Corrosion resistance and a high strength-to weight ratio is achieved featuring thermoplastic and stainless steel components [31]. The output signal is an analog DC voltage from a 10k-ohm conductive plastic potentiometer which ranges from 0 to excitation voltage (excluding deadband).



**Figure 13.** Wind direction vane [31]

### **2.2.5 Barometric Pressure Sensor**

Shown in Figure 14, RM Young 61302V barometric pressure sensor is a versatile electronic barometer which measures pressure in a range of 500 to 1100 hPa [32]. In addition to high accuracy, it has low power consumption and a wide temperature range, making it an ideal choice for battery-powered remote applications [32]. It was used in serial mode using RS-232 with continuous ASCII text output with a baud rate of 9600. Embodied in a fiber-reinforced thermoplastic, this sensor was placed inside the data acquisition box.



Model 61302V © 2009 Campbell Scientific (Canada) Corp.

**Figure 14.** Barometric pressure sensor [32]

### 2.2.6 Temperature and Relative Humidity Probe

Illustrated in Figure 15, the HC2-S3-L temperature and RH probe manufactured by Rotronic Instrument Corp. measures the air temperature with a Pt100 RTD (IEC751, 1/3 DIN, Class B) and relative humidity (RH) based on the HygroClip2 technology [33]. The temperature and relative humidity sensors are protected against errors caused by direct and reflected solar radiation using a multi-plate radiation shield [34]. Moisture accumulation from precipitation and dew are also minimized by the enlarged top plate and steep edge profile [34]. UV stabilized white thermoplastic plates have high reflectivity, low thermal conductivity, and maximum weather resistance [34].



**Figure 15.** Temperature and relative humidity probe [33]

### 2.2.7 Incremental Encoders

An incremental (also known as optical) rotary encoder provides repeating periodic counting track to record positional changes that can measure both the distance and direction of travel. A directional reference and a count would be the basis of the measurement. Shown in Figure 16, the IH 103 encoder used to measure the main rotor speed, employs two outputs called A and B, which are 90 degrees out of phase (and hence called quadrature outputs) [35]. The output signal schematic is illustrated in Figure 17. In the clock wise direction A leads B [35].

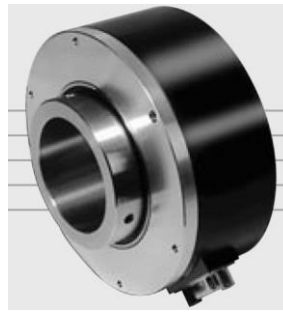


**Figure 16.** Hollow shaft encoder [35]

As for the turbine yaw mechanism, a 512 PPR encoder along with a slew drive and a DC motor were designed to be used to control the turbine yaw actively [36]. This sensor was not used in the course of this study due to mechanical issues as well as connection failure during the initial set of runs.

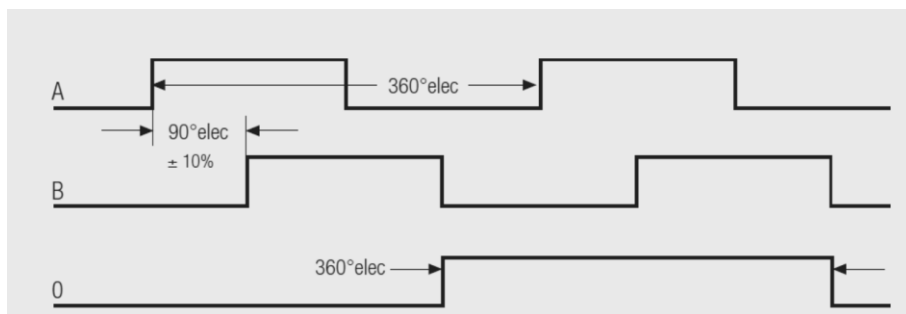


**Figure 17.** Shaft encoder output signal schematic [35]

## 2.3 Electrical System

The electrical system of the test rig comprises a brushless permanent magnet AC hub motor/generator, an electric vehicle controller capable of regenerative braking, a brushed DC motor for an active yaw of a slew drive, a 48 VDC lead acid battery bank, a diversion load and diversion load controller, contactors, power relays, power and data switches, fuses, busbars, and all pertaining wiring [37].

### 2.3.1 Main Motor and Controller

The main generator is an electric vehicle motor/generator coupled with a controller. Shown in Figure 18 (a), the ME0907, 8-pole, brushless, Y-connected, permanent magnet AC motor/generator is 90% efficient, has high durability, and minimized electromagnetic interface [38].

This motor was paired with a Sevcon Gen4 controller, illustrated in Figure 18 (b), a complex controller with regenerative braking capability [39]. This combination is typically used for small electric vehicles such as golf carts or electric sailboats.



(a) PMAC motor/generator



(b) Sevcon Gen4 controller

**Figure 18.** Main motor and controller [39]

Gen4 controller's main function is to control the power to the three phases of the PMAC motor/generator [39]. Motor's rotor position information, sent to the controller using a digital sensor, allows the controller to energize the motor phases appropriately based on the measured position of the magnets on the rotor [39].

The controller was programmed to be used in two modes, namely: throttle (motor) and regeneration (generator). In the throttle mode, the 48 VDC of the battery bank is inverted into a three-phase AC by the controller to spin up the turbine rotor, essentially acting as a motor. In the regeneration mode, the three-phase AC signal generated by back driving the motor is rectified back to DC and fed back to the battery bank.

In other words, suppose the intent is that the wind turbine tracks a fixed rotational speed. When the aerodynamic power is less than friction losses, the battery bank is used in the throttle mode to spin up the turbine rotor. On the other hand, when the net torque is positive, through regenerative braking in the regeneration mode, the kinetic energy in the wind converted into electricity is sent to the battery bank for storage. The latter is corresponding to the power production mode of the wind turbine. Details about the control system design and implementation using this motor controller, CompactRIO, and a LabVIEW-based controller will be explained in Chapter 4.

It should be noted that drivetrain of this test rig includes a 5:1 planetary gear head required to match the expected low speed (turbine side) operation with the high speed (generator side) motor/generator functionality requirements specified by the manufacturer.

### 2.3.2 Battery Bank and Converters

This test rig has the capability to operate autonomously using a 48 VDC battery bank capable of powering all subsystems. This battery bank is equipped with a Battery Management System (BMS) consisting of a dump load controller paired with two large air resistors, to protect the battery bank against overcharge.

A Littelfuse CF8, 250 A at 58 VDC, terminal fuse was also used to provide overcurrent protection. As discussed in 2.3.1, when operating in free stream as an actual turbine, the wind power is stored in this battery bank utilizing the regenerative braking, acting within the main control system.

This battery bank contains four 12 VDC 8A27 - DEKA Absorbed Glass Matt sealed deep cycle lead acid batteries shown in Figure 19 (a) [40]. Depicted in Figure 19 (b), an Iota DLS-54-13, 48 VDC battery charger is available to charge the battery when necessary. Throughout the instrumentation and LabVIEW development phase, this charger was used to keep the state of charge at an acceptable level, to maintain maximized battery cycles.



(a) AGM 12 VDC battery



(b) Battery charger

**Figure 19.** Battery and charger

To ensure safe operation, given the potential existence of large floating voltages, four electrically-isolated and regulated DC/DC converters were used to step down voltages and power various subsystems as summarized in Table 4.

**Table 4.** DC/DC converters

DC/DC Converter Type	DC/DC Converter Model	Target Subsystem
48 to 24 VDC (100W)	Wilmore Electronics 1640	CompactRIO
48 to 24 VDC (100W)	Wilmore Electronics 1640	Slew drive motor
48 to 12 VDC (100W)	Wilmore Electronics 1640	Sensors
12 to 10 VDC (20W)	Phoenix Contact (2320018)	Loadcell Wheatstone bridges

### 2.3.3 Dump Load Controller

The battery bank voltage and battery temperature will be measured utilizing a 45 A Tristar dump load controller illustrated in Figure 20 [41]. This controller (diversion load regulator) will manage battery charging by diverting the energy from the battery to a diversion load. The diversion load consists of two large 2-ohm, 300-W air resistors. When the battery voltage exceeds a programmed level, this dump load controller will divert power to the air resistors, which in turn convert the excess energy into heat [37].



**Figure 20.** Dump load controller

### 2.3.4 Yaw System

The test rig has a capability to actively perform yaw control using a worm slew bearing and a Midwest Motion 24 VDC motor [42] depicted in Figure 21. The DC motor has an inline 35:1 planetary gear head that when combined with the slew drive's 62:1 gear reduction, gives a total gear reduction of 2170 [37]. As pointed in 2.2.7, a 512 PPR encoder within this system gives a high resolution positioning capability. Due to time constraints, experiments in the current study were conducted in a fixed-yaw position; and hence, this active yaw system and the wind direction vane data were not used. The designed control system that will be covered in Chapter 4, successfully managed to ensure safe operation under high winds during controlled velocity runs.



(a) Slew drive



(b) DC motor [42]

**Figure 21.** Slew drive and DC motor

## 2.4 Data Acquisition System

As shown in Figure 22, this test rig utilizes National Instruments (NI) hardware products including the CompactRIO (CRIO) controller, chassis, and C-series modules as its data acquisition system along with the LabVIEW software.

The CompactRIO, which is a reconfigurable embedded system, has three components: a processor running a real-time operating system (RTOS), a configurable field-

programmable gate array (FPGA), and interchangeable industrial I/O (input/output) modules [43]. The architecture of this RTOS is illustrated in Figure 23 schematically [43]. CompactRIO applications typically include a human machine interface (HMI), providing the operator with a GUI to monitor the system's setting and operating parameters [43].

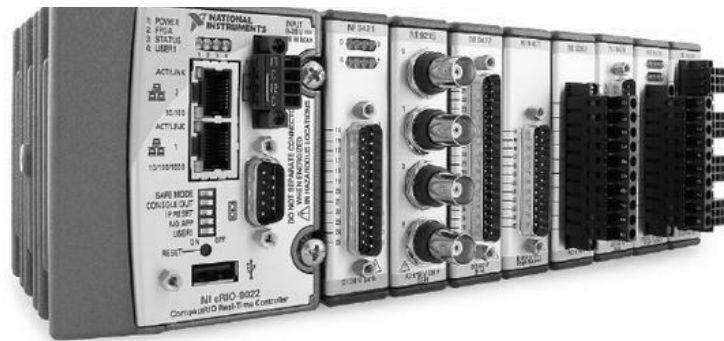


**Figure 22.** National Instruments data acquisition system

Components of National Instruments hardware used on the test rig as well as the associated sensors connected to the C-series I/O modules are summarized in Table 5. More information about these components will be covered in Chapter 3 where detailed specifications regarding the uncertainty analysis will be discussed.

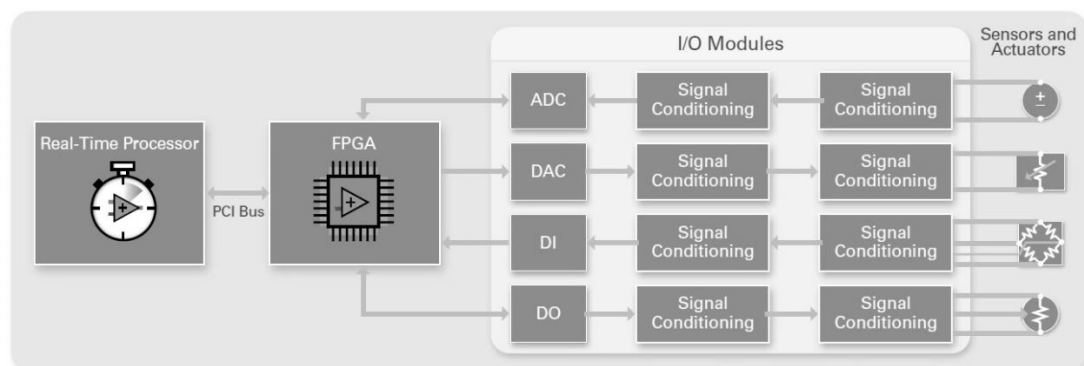


**Figure 23.** CompactRIO reconfigurable embedded system architecture

**Table 5.** Data acquisition system components

NI Hardware	Type and Features	Sensor(s)
NI 9022 Controller	CompactRIO Controller	-
NI 9114 Chassis	CompactRIO Chassis	-
NI 9201 (I/O Module)	8 Ch, $\pm 10V$ , 12-Bit, Analog Input	Temperature and relative humidity probe, wind vane
NI 9411 (I/O Module)	6 Ch, Differential Digital Input	Shaft encoder, cup anemometer interface
NI 9870 (I/O Module)	4 Port, RS232 Serial	Ultrasonic anemometer, pressure sensor
NI 9263 (I/O Module)	4 Ch, $\pm 10V$ , 16-Bit, Analog Output	EV controller throttle and regeneration
NI 9237 (I/O Module)	4 Ch, 24-Bit, Full Bridge, Analog Input	Loadcell Wheatstone bridges
NI 9505 (I/O Module)	DC Brushed Servo Motor	Yaw system

#### 2.4.1 National Instruments CompactRIO Controller

Being a part of the high performance CompactRIO programmable automation controller (PAC), the NI 9022 is a small and rugged real-time embedded controller that runs LabVIEW real-time for deterministic control, data logging, and analysis [44]. This controller is particularly designed for reliable and deterministic operation for stand-alone control, monitoring, and logging [44], making it a perfect fit for the test rig.

It features a 533 MHz Freescale MPC8347 real-time processor, 2 GB non-volatile storage, 256 MB DDR2 memory, dual Ethernet ports with embedded Web and file servers for remote user interfacing, hi-Speed USB host port for connection to USB flash and memory devices, RS232 serial port for connection to peripherals; dual 9 to 35 VDC supply inputs, and with a -20 to 55 °C operating temperature range [44].



**Figure 24.** NI CRIO controller

### 2.4.2 National Instruments CompactRIO Chassis

At the heart of the embedded system architecture, the FPGA chassis shown in Figure 25 is directly connected to the I/O modules for high-performance access to the I/O circuitry of each module and timing, triggering, and synchronization [43]. Compared to other controller architectures, as each module on this chassis is directly connected to the FPGA rather than through a bus, the latency in system response is practically minimal [43].



**Figure 25.** Reconfigurable FPGA chassis

### 2.4.3 National Instruments I/O Modules

Input/output (I/O) modules encompass isolation, conversion circuitry, signal conditioning, and built-in connectivity that can be utilized for direct connection to industrial sensors and actuators [43]. Through offering a range of wiring options and integrating the connector junction box into the modules, the CRIO system reduces space requirements as well as the field wiring costs significantly (hence called compact) [43]. More information regarding the modules used in this application will be covered when conducting the uncertainty analysis in Chapter 3.

### 2.5 System Integration

An overview of the system components is illustrated in Figure 26. The main electrical cabinet (ELEC) includes the electric vehicle controller, DC/DC converters, dump load controller, and the rest of the electrical components. The wind turbine nacelle includes the shaft encoder, multi-axial loadcell, planetary gear head, as well as the PMAC generator. Details regarding the control cabinet (CTRL) will be covered in Chapter 4.

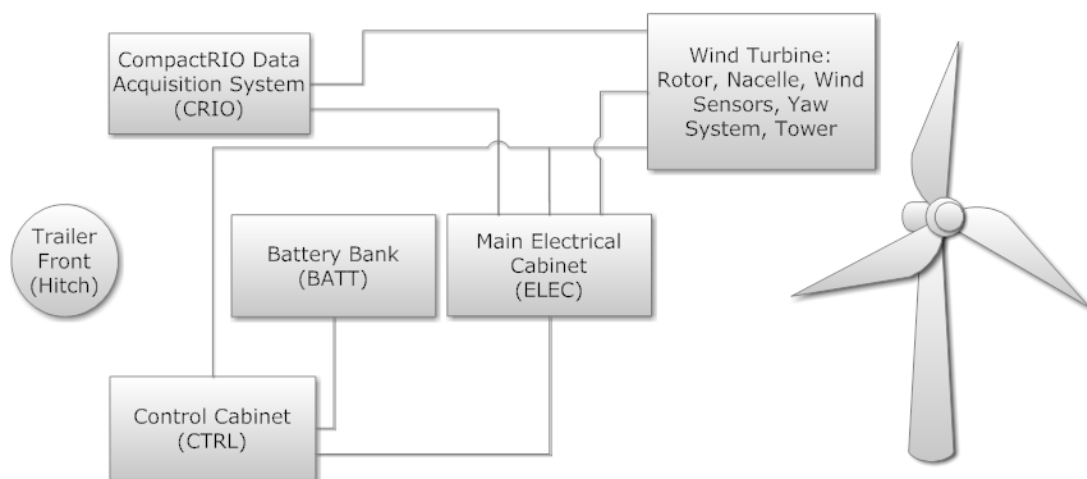


**Figure 26.** System integration

The main contribution of the current research work at this phase was to modify the instrumentation of the test rig as well as to develop a custom LabVIEW GUI illustrated in Figure 27. To achieve this goal, various sensors were tested utilizing individual test programs. Subsequently, the individual components were effectively integrated into a main program which can now be utilized through the developed program. Work instructions developed for both custom LabVIEW application as well as the control cabinet interface are presented in Appendix B. In addition, throughout the research work, hardware (e.g. nacelle cover was printed using the FDM technology) and software (e.g. the ultrasonic anemometer was programmatically changed to meet the desired experimental characteristics) modifications were made, when necessary, to ensure safe and reliable operation.

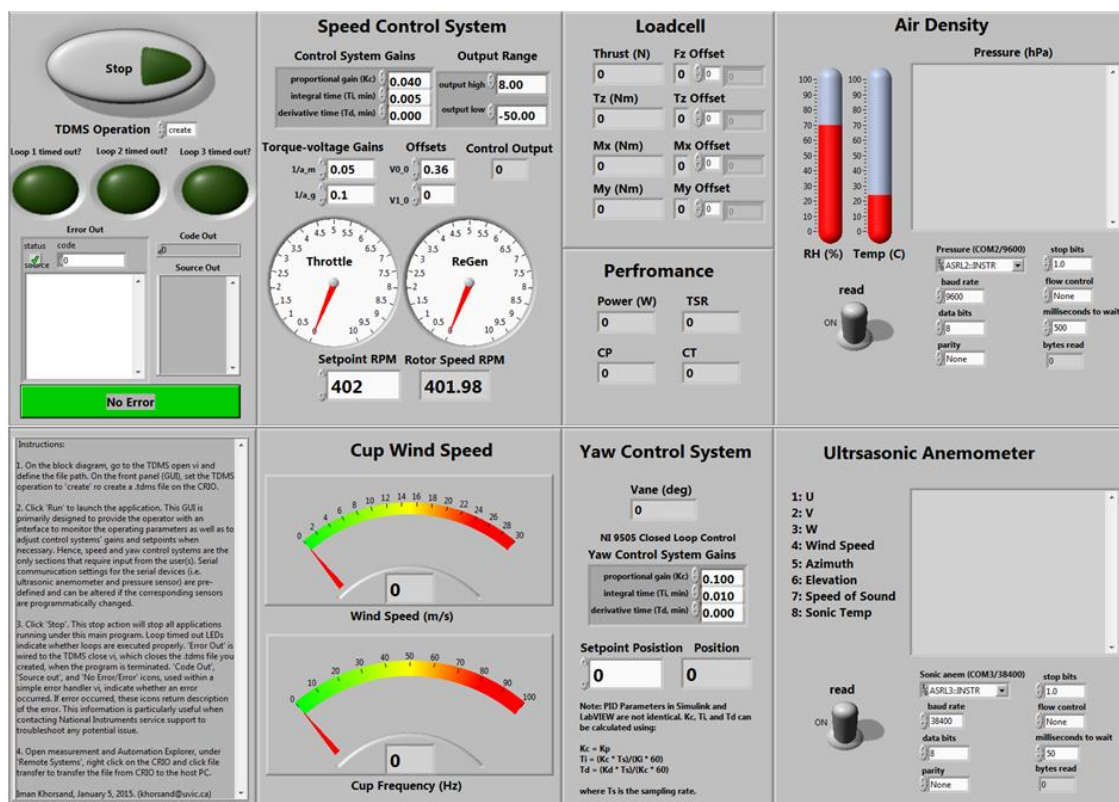


Figure 27. Graphical user interface of the test rig

## **Chapter 3: Operating Parameters and Uncertainty Analysis**

Given the importance of understanding the uncertainty associated with the final results of an experiment to reach meaningful conclusions, a thorough analysis is often required.

The choice of methodology to adopt to quantify and bundle various uncertainty constituents really depends on the specifics of the experimental work as well as any potential standard pertaining to the targeted area of study. In fact, reviewing the existing literature reveals that in most publications the uncertainty associated with the experimental results have not been reported as thoroughly as possible. In addition to explaining the operating parameters involved in track testing utilizing the test rig introduced, this chapter describes the process by which the total uncertainty associated with directly measurable parameters and pertinent uncertainty propagating to the calculable parameters can be estimated.

### **3.1 Uncertainty and Error Types**

The measurement error is the difference between the measured value and the true value of the measurand such as wind speed. Since the true value of the measured variable is unknown, the actual error is a rather elusive quantity. Hence, an estimation of the errors involved in the experiment is of interest and is called uncertainty [45]. In experiments, errors can be categorized into precision (random, aleatoric) errors and bias (systematic, epistemic) errors. Instrument manufacturers often state (in)accuracy of an instrument, which typically includes all sources of errors including bias and precision errors.

Precision errors are associated with sources such as the least count of the scale of an analogue signal, analog to digital signal conversions, repeatability errors due to

fluctuations in experimental conditions, and etc. The existence of all these precision errors leads to experimental data scatter which can be treated adequately using the statistical analysis and the theory of statistics [45].

Bias errors have various sources such as zero-offset, sensitivity, nonlinearity, hysteresis, etc. The main source is a calibration error of an instrument that include zero-offset or a scale error (also called sensitivity or span errors) in the input-output response curve for an instrument element. The former source leads to a constant absolute error in all the readings while the latter causes a constant percentage error in all the readings [45]. Another source of bias error is what is called hysteresis, the output varies based on whether the input is increasing or decreasing [45].

In general, four rules suggested in [45] can be followed for error estimates. First, when an error from a particular source is found to be significantly smaller than other existing errors, it can be neglected. Secondly, the major concern of the uncertainty analysis is quantitative estimates of bias errors and feasibly pertinent data correction. Third, precision errors can be estimated from repeated tests or via observation of the resultant graphical data scatter (when possible). Finally, in terms of experimental planning, wherever the bias error estimates are significant, further actions are to be taken to ensure that precision error estimates are much smaller.

### **3.2 Methods**

Inspired by ASME step-by-step procedure for uncertainty analysis described in [46], [47] the overall uncertainty analysis of the test rig was conducted in six steps for the current study:

1. Focusing on test objectives, measurement process was defined; all independent variables (measurable parameters) and their functional relationship to the final results (calculable parameters) were identified.
2. All elemental sources of uncertainty (e.g. sensors, data acquisition system, test data) were identified and categorized into two general groups; bias (systematic) and precision (random) uncertainties.
3. Elemental sources of uncertainty were quantified using manufacturers' specification sheets as well as statistical techniques (assuming normality and a 95% confidence level).
4. Bias and precision uncertainties for each measured variable were calculated.
5. Uncertainty in each measured variable was propagated to the final results.
6. Total uncertainties of the results in engineering units and percentage of full scale were calculated and tabulated. Three different scenarios were considered for the precision uncertainty estimation.

Prior to calculating the uncertainty in various measurands and results, a brief summary of statistical concepts used will be provided in the following section.

### **3.2.1 Statistical Summary**

Population refers to the entire collection of objects, measurement observations whose properties are under consideration (e.g. the test rig's power coefficient at a given tip speed ratio) [46]. A sample is a representative subset of a population. An experiment is performed on a sample and experimental data pertaining to this sample is collected [46].

A measurement can be repeated a number of times to acquire a sample mean and subsequently to investigate how the measured values scatter around the sample mean using the standard deviation [46]. Suppose  $x$  is the variable being measured and  $x_1, x_2, \dots, x_n$  are recorded for a sample of size  $n$ , the sample mean is  $\bar{x}$

$$\bar{x} = \frac{1}{n} \sum_{i=1}^n x_i \quad (3.1)$$

The standard deviation  $S_x$  can then be calculated as

$$S_x = \left[ \frac{1}{n-1} \sum_{i=1}^n (x_i - \bar{x})^2 \right]^{1/2} \quad (3.2)$$

The intent is to make an estimate of the population mean  $\mu_x$ , based on the sample mean  $\bar{x}$ , and the uncertainty  $U_x$  [46].

$$\mu_x = \bar{x} \pm U_x \quad (3.3)$$

Often a confidence level  $C$  is reported, indicating the probability that the population mean will fall within the pointed interval. When we say that our uncertainty at a confidence level of 95 % is  $U_x$ , we are stating that we are expecting that the true value of the population mean lies within the interval  $\bar{x} \pm U_x$  about 95 times out of a 100.

When several different samples of a population are available, each sample of size  $n$  would have a mean value  $\bar{x}_i$ . The central limit theorem then states that if  $n$  is sufficiently large (typically  $n > 30$ ), the mean values of the samples follow a normal distribution and the standard deviation of these means, which is called the standard error of the mean (SEM), is given by [46, 47]:

$$S_{\bar{x}} = \frac{S_x}{\sqrt{n}} \quad (3.4)$$

While standard deviation of the mean indicates how far the sample mean is likely to be from the population mean, standard deviation is a measure of how individuals within a sample differ from the sample mean. It is worth mentioning that as long as the sample size is large enough, the population does not have to necessarily be normally distributed for the assumption of normally distributed means to be valid. In this document, since the uncertainty of how far the sample mean is likely to be from the population mean is of interest, standard deviation of the mean will be used.

### 3.2.2 Precision (Random) Uncertainty

Standard deviations of a measurement can be combined using the root of the sum of the squares technique referred to as RSS [46]:

$$S_x = \left[ \sum_{i=1}^n S_i^2 \right]^{1/2} \quad (3.5)$$

Subsequently, the precision uncertainty for a single measurement of variable  $x$  would be  $P_x = 2S_x$  ( $C = 95\%$ ,  $n > 30$ ). Given the Student's  $t$  value of 1.96 ( $C = 95\%$ ,  $n > 30$ ), the precision uncertainty in the sample mean can be expressed as [46]:

$$P_{\bar{x}} = \frac{1.96 S_x}{\sqrt{n}} \cong 2 S_{\bar{x}} \quad (3.6)$$

### 3.2.3 Bias (Systematic) Uncertainty

According to our knowledge of the test rig, instrumentation, techniques, and pertinent physical phenomena, the bias uncertainty can be calculated. In case of having different elemental sources of bias errors, these elements could be estimated arithmetically to obtain the worst case scenario (upper bound) [45]. A better estimate of the combined bias uncertainty can be calculated using RSS. The latter approach will be used in this

document. It is worth mentioning that the bias uncertainty is independent of the sample size while the precision uncertainty can be reduced through increasing it [45]. The total bias elemental uncertainty,  $B_x$ , (of  $m$  elements in the system) can be calculated as:

$$B_x = \left[ \sum_{i=1}^m B_i^2 \right]^{1/2} \quad (3.7)$$

### 3.2.4 Total Uncertainty

Given the conceptual difference, the choice of whether to combine physical bias uncertainties with statistically attained precision uncertainties really depends on the application, specifics of the experimental setting, and rationale of the experimenter. In fact, there is no universally accepted practice for reporting total uncertainty, applicable to various fields. Since the intent of this chapter is to give an overview of the total uncertainty of the measurements recorded using the designed test rig, the most common method of total uncertainty quantification will be used here. For a confidence level of 95 %, the total uncertainty  $U_x$  in measuring variable  $x$  can be calculated combining both bias  $B_x$  and precision  $P_x$  uncertainties using [46]:

$$U_x = (B_x^2 + P_x^2)^{1/2} = (B_x^2 + [2S_x]^2)^{1/2} \quad (3.8)$$

### 3.3 Data Acquisition System Uncertainty Analysis

The first uncertainty source is the data acquisition system. To determine how accurate the CRIO device is, detailed specification provided by the manufacturer need to be analyzed. The uncertainty in the device used for the measurement,  $U_{CRIO}$ , is typically specified in terms of gain (reading), offset (range), and the noise ( $U_N$ ) uncertainties by National Instruments [48]:

$$U_{CRIO} = (Reading \times Gain) + (Range \times Offset) + U_N \quad (3.9)$$

Moreover, since the CRIO contains a number of c-series I/O modules in its chassis, uncertainty in each module needs to be quantified individually.

Detailed manufacturer specification of the NI 9237 loadcell module is provided in Table 6 and [49]. Considering the best performance, the first row corresponding to the readings taken within a year of calibration (assuming a temperature range of 25 C°, ± 5 C°) will be used here. In addition, the noise uncertainty can be calculated using the input noise reported for the full bridge configuration and 10 V of excitation as follows [49]:

$$U_N = 3 \times V_{rms} = 0.9 \frac{\mu V}{V} \quad (3.10)$$

The uncertainty of the module (for full ± 25 mV/V) can then be calculated as:

$$U_{DAQ} = \left(0.0005 \times 0.025 \frac{V}{V}\right) + \left(0.0005 \times 0.025 \frac{V}{V}\right) + 0.9 \frac{\mu V}{V} \quad (3.11)$$

$$U_{DAQ} = \pm 25.9 \frac{\mu V}{V}$$

**Table 6.** NI 9237 uncertainty [49]

Measurement Conditions	Percent of Reading (Gain Error)	Percent of Range (Offset Error)
Calibrated, typ (25 C°, ± 5 C°)	± 0.05 %	± 0.05 %
Calibrated, max (-40 to 70 C°)	± 0.20 %	± 0.25 %
Uncalibrated, typ (25 C°, ± 5 C°)	± 0.20 %	± 0.10 %
Uncalibrated, max (-40 to 70 C°)	± 0.55 %	± 0.35 %

Range equals 25 mV/V.  
Before offset null and shunt calibration.

Generally, as the output of an analog to digital converter (ADC) changes in discrete steps, there will be a precision uncertainty associated with this quantizing as well, which is equal to 0.5 LSB, where LSB is the least significant bit [46]. In terms of the input units, this uncertainty can be calculated using module's upper range  $V_{ru}$ , lower range  $V_{rl}$ , and its ADC's number of bits  $N$ :

$$U_Q = 0.5 \times \frac{V_{ru} - V_{rl}}{2^N} \quad (3.12)$$

The NI 9237 module has a Delta-sigma (with analog pre-filtering) ADC with a resolution of 24 bits. Although negligible, the quantizing uncertainty, considering the 10 V excitation and  $\pm 25$  mV/V input range, can also be calculated:

$$U_Q = 0.5 \times \frac{0.25 - (-0.25)}{2^{24}} = 0.00149 \text{ } \mu\text{V} \quad (3.13)$$

As for the NI CRIO 9201 module, detailed specification information of the module can be found in Table 7 and [50]. Using equation (3.12), the quantization uncertainty of  $\pm 0.00244$  V is the best that can be achieved by the 12-bit ADC. Gain error for the maximum voltage reading is 0.004 V and the offset error is 0.007 V (input noise excluded). This gives an uncertainty of 0.01158 V. Using the RSS method, the total uncertainty (including gain, offset, quantization, and excluding noise, drifts, etc.) of the module can be calculated to be 0.011837 V.

**Table 7.** NI 9201 uncertainty (noise excluded) [50]

Measurement Conditions	Percent of Reading (Gain Error)	Percent of Range (Offset Error)
Calibrated, typ (25 C°, $\pm 5$ C°)	$\pm 0.04$ %	$\pm 0.07$ %
Calibrated, max (-40 to 70 C°)	$\pm 0.25$ %	$\pm 0.25$ %
Uncalibrated, typ (25 C°, $\pm 5$ C°)	$\pm 0.26$ %	$\pm 0.46$ %
Uncalibrated, max (-40 to 70 C°)	$\pm 0.67$ %	$\pm 1.25$ %
Range equals 10.53 V		

For NI CRIO 9263 16-bit module, the uncertainty due to the quantizing is only

$$U_Q = 0.5 \times \frac{10 - (-10)}{2^{16}} = 0.000153 \text{ V} \quad (3.14)$$

As presented in Table 8, for the maximum reading of 10 V, the gain error is 0.035 V and the offset error is 0.075 V. Total uncertainty of the module (excluding the noise, drifts, etc.) due to gain, offset, and quantization can be estimated to be 0.11 V. More details regarding this module can be accessed in [51].

**Table 8.** NI 9263 uncertainty [51]

Measurement Conditions	Percent of Reading (Gain Error)	Percent of Range (Offset Error)
Calibrated, max (-40 to 70 C°)	0.35 %	0.75 %
Calibrated, typ (25 C°, ± 5 C°)	0.01 %	0.1 %
Uncalibrated, max (-40 to 70 C°)	2.2 %	1.7 %
Uncalibrated, typ (25 C°, ± 5 C°)	0.3 %	0.25 %

Total uncertainties associated with the NI modules are summarized in Table 9. The information required to quantify the uncertainty in measurements out of NI 9411 (digital), NI 9870 (serial), and NI 9505 (digital) was not available from the manufacturer.

**Table 9.** Uncertainty of NI CRIO modules

	NI 9237	NI 9201	NI 9263	NI 9411	NI 9870	NI 9505
Uncertainty (V)	2.59e-4	1.18e-2	1.10e-1	-	-	-

### 3.4 Sample Data for Initial Uncertainty Analysis

To understand the total uncertainty associated with the test results a sample test data presented in Table 10 will be used to quantify the uncertainty in the final results. This sample data was taken from one of the experimental runs that will be discussed in Chapter 6.

It should be noted that the reported SEM is the standard deviation of the mean for four-second-averaged values when the CRIO was running at 50 Hz, which in turn translates into a sample size of 200. Another point that needs to be mentioned here is that to quantify an upper bound on the uncertainty, this sample data was selected from a case of running at above-rated wind and rotor speeds. Upon replacing the outliers with the mean values, standard deviations of the mean for temperature and relative humidity, which were recorded within the same timed loop, were calculated across the full run.

For the serial devices, the sample size was considered primarily based on the actual output rates of the sensors. The sample size selected for the ultrasonic anemometer was chosen in the exact period that was used for the timed loop to have a reference for the cup wind speed measurement.

**Table 10.** Sample test run timed loop measured and calculated data

	Rotor speed (RPM)	Cup wind speed (m/s)	Thrust (N)	Torque (N.m)	Power (W)	C <sub>p</sub>	C <sub>T</sub>	TSR
Mean	450.143	16.258	80.612	11.316	533.400	0.084	0.206	2.539
SEM <sup>1</sup>	0.013	0.018	0.541	0.005	0.230	0.000	0.001	0.003
SEM <sup>2</sup>	0.129	0.179	5.412	0.049	2.296	0.003	0.010	0.030
SD	0.182	0.253	7.654	0.070	3.247	0.004	0.014	0.040
Min	449.981	15.983	72.056	11.248	530.129	0.080	0.191	2.504
Max	450.340	16.481	86.807	11.387	536.623	0.089	0.220	2.582

**Table 11.** Sample test run timed loop and serial data for air density calculation

	Temperature (C°)	Relative humidity	Pressure (hPa)
Mean	13.351	0.665	1028.741
SEM	0.010 <sup>3</sup>	0 <sup>4</sup>	0.003 <sup>5</sup>
SD	1.524	0.029	0.075
Min	10.430	0.504	1028.640
Max	13.515	0.797	1028.850

**Table 12.** Sample test run serial ultrasonic data

	U (m/s)	V (m/s)	W (m/s)	Sonic Wind Speed (m/s)	Azimuth (degree)	Elevation (degree)	Speed of Sound (m/s)	Sonic Temperature (C°)
Mean	-16.712	-0.654	0.630	16.760	267.733	2.156	338.45	11.112
SEM <sup>6</sup>	0.038	0.027	0.015	0.038	0.093	0.051	0.006	0.010
SD	0.756	0.537	2.437	0.756	1.851	1.015	0.119	0.199
Min	-18.270	-1.890	-0.110	13.96	263.400	-0.400	338.280	10.830
Max	-13.940	1.200	1.760	18.310	273.900	5.800	339.080	12.700

<sup>1</sup> Standard error of the mean (standard deviation of the mean) for n = 200.

<sup>2</sup> Standard error of the mean (standard deviation of the mean) for n = 3.

<sup>3</sup> Standard error of the mean (standard deviation of the mean) for n = 22257.

<sup>4</sup> Standard error of the mean (standard deviation of the mean) for n = 22257.

<sup>5</sup> Standard error of the mean (standard deviation of the mean) for n = 1159.

<sup>6</sup> Standard error of the mean (standard deviation of the mean) for n = 396.

### 3.5 Uncertainty in Measurable Parameters

Uncertainty associated with the directly measurable parameters (e.g. torque, thrust, wind speed, and rotor speed) will be discussed in this section.

#### 3.5.1 Torque, Thrust, Pitching, and Yawing Moments

Ideally, a load along any one of four axes of the loadcell will not produce an output on the other channels; however, in reality this undesired influence exists in any practical multi-axial loadcell and is called Cross Talk. If the cross talk is ignored for nominal readings, each bridge can be treated as a pure output, scaled to the data on the certificates of test and calibration. In this case, an induced cross talk bias uncertainty of up to 3 % RL (rated load) should be given to any axis associated to a full load being applied on any other axis [53]. Other elemental sources of uncertainty from the manufacturer's specification are summarized in Table 13.

**Table 13.** Generic multi-axial loadcell specifications [21]

Elemental Source	Uncertainty
Linearity	± 0.5 % RL
Hysteresis	± 0.5 % RL
Repeatability	± 0.02 % RL
Cross-talk	± 1.25 % RL

A calibration correction matrix can be derived based on the cross talk data provided by the manufacturer. This method of cross talk compensation involves manipulating the loadcell output data mathematically using an inverse matrix [52]. Applying a known load in line with one the measurement axis, and recording the output from the associated channel, the first transfer function (e.g. for the thrust force) would be the channel output,  $O_{Fz}$ , is equal to the sensitivity (mV/V per unit load),  $k_1$ , times the applied load,  $F_z$ :

$$O_{Fz} = k_1 \times F_z \quad (3.15)$$

The output of other channels will be recorded as cross talk simultaneously. In other words,

$$O_{Fz} = k_1 \times F_z$$

$$O_{Tz} = k_5 \times F_z \quad (3.16)$$

$$O_{Mx} = k_9 \times F_z \quad (3.17)$$

$$O_{My} = k_{13} \times F_z \quad (3.18)$$

Following the same procedure and utilizing the theory of superposition, the combined output equations that fully describe the output of the sensor would be:

$$O_{Fz} = k_1 \times F_z + k_2 \times T_z + k_3 \times M_x + k_4 \times M_y \quad (3.19)$$

$$O_{Tz} = k_5 \times F_z + k_6 \times T_z + k_7 \times M_x + k_8 \times M_y \quad (3.20)$$

$$O_{Mx} = k_9 \times F_z + k_{10} \times T_z + k_{11} \times M_x + k_{12} \times M_y \quad (3.21)$$

$$O_{My} = k_{13} \times F_z + k_{14} \times T_z + k_{15} \times M_x + k_{16} \times M_y \quad (3.22)$$

In order to solve for the unknown loads from the known outputs, the inverse correction matrix can be derived. Upon deriving the inverse correction matrix, the force and moments can be calculated using:

$$\begin{bmatrix} F_z \\ T_z \\ M_x \\ M_y \end{bmatrix} = [K]^{-1} \cdot \begin{bmatrix} O_{Fz} \\ O_{Tz} \\ O_{Mx} \\ O_{My} \end{bmatrix} \quad (3.23)$$

The important step is correction matrix derivation from the manufacturer cross talk data provided with the sensor. Based on the calibration data provided by the manufacturer, sensitivity (for 10 V supply), transducer outputs for maximum range, and the zero balance specifications are summarized in Table 14. In addition the cross talk data is listed in Table 15. The data points show the maximum cross talk output recorded on each bridge

while the rated load was applied to all other axes in turn. The data was available only for the maximum load points; however, in general, there is a linear relationship between the output and off axis load being applied [53].

**Table 14.** Custom loadcell specifications [Appendix A]

Measrand	Range	Zero balance (mV)	Positive output (mV/V)	Negative output (mV/V)
$F_z$ (N)	900	-0.350	0.6981	-0.6802
$T_z$ (N.m)	75	-0.134	1.0605	-1.0601
$M_x$ (N.m)	75	0.136	1.0684	-1.0612
$M_y$ (N.m)	75	0.136	1.0749	-1.0650

The cross talk performance can then be extracted by dividing the channel output due to an extraneous load, by the full scale output for that same channel [52]. The calculated cross talk performance for percentage of full scale output is presented in Table 16.

**Table 15.** Cross-talk raw data [Appendix A]

	$F_z$ (mV)	$T_z$ (mV)	$M_x$ (mV)	$M_y$ (mV)
$F_z +$		-0.2204	-0.3059	-0.0324
$F_z -$		0.1997	0.2091	0.2922
$T_z +$	-0.0099		-0.0373	0.1324
$T_z -$	0.0060		-0.0450	-0.1930
$M_x +$	-0.2074	0.0306		-0.0571
$M_x -$	0.2133	0.0292		0.0649
$M_y +$	-0.0606	0.0114	0.0133	
$M_y -$	-0.0246	-0.0485	0.0530	

**Table 16.** Cross talk performance (% full scale output)

	$F_z$	$T_z$	$M_x$	$M_y$
$F_z +$		-3.16	-4.38	-0.46
$F_z -$		-2.94	-3.07	-4.30
$T_z +$	-0.09		-0.35	1.25
$T_z -$	-0.06		0.42	1.82
$M_x +$	-1.94	0.29		-0.53
$M_x -$	-2.01	-0.28		-0.61
$M_y +$	-0.56	0.11	0.12	
$M_y -$	0.23	0.46	-0.50	

As can be seen in Table 16, the minimum cross talk is only 0.06 % of the full scale load when  $F_z$  is applied to the  $T_z$  channel. On the other hand the maximum cross talk is 4.38

% The average cross talk for the sensor is around 1.25 %. The data matrix,  $K$ , can be constructed by dividing cross talk data by the applied load.

$$K = \begin{bmatrix} 0.0008 & -0.0003 & -0.0004 & 0.0000 \\ -0.0008 & 0.0003 & 0.0003 & 0.0004 \\ 0.0000 & 0.0141 & 0.0000 & 0.0002 \\ 0.0000 & -0.0141 & -0.0001 & -0.0003 \\ 0.0000 & 0.0000 & 0.0142 & -0.0001 \\ 0.0000 & 0.0000 & -0.0141 & 0.0001 \\ 0.0000 & 0.0000 & 0.0000 & 0.0143 \\ 0.0000 & -0.0001 & 0.0001 & -0.0142 \end{bmatrix} \quad (3.24)$$

Subsequently the inverse matrix and required corrected output could be calculated using a computer program (signs of the axes are to be detected). As depicted in Figure 28, the offset error is compensated in the LabVIEW program.

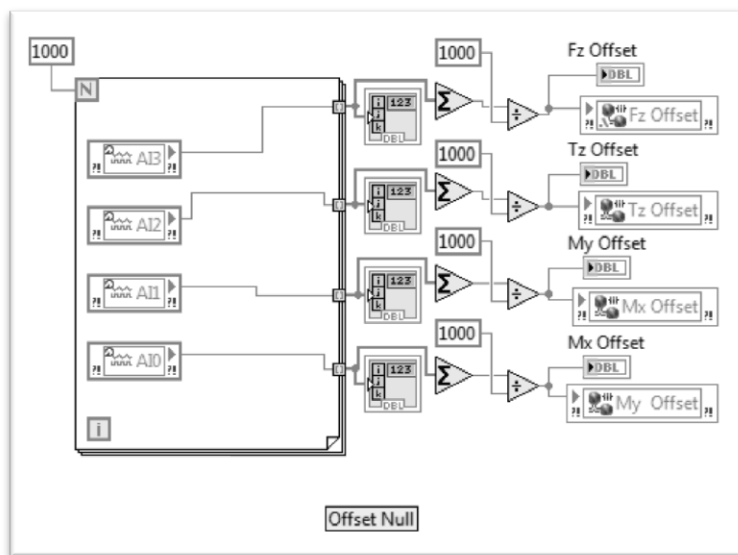


**Figure 28.** Loadcell offset null in LabVIEW

During the initial set of runs, reported sensitivities were simply used to obtain the thrust and the three moments. Based on the manufacturer specification reported in Table 14 (signs were selected according to an initial measurement), the following conversion matrix was used:

$$\begin{bmatrix} F_z \\ T_z \\ M_x \\ M_y \end{bmatrix} = \begin{bmatrix} -1323140 & 0 & 0 & 0 \\ 0 & -70748 & 0 & 0 \\ 0 & 0 & -70675 & 0 \\ 0 & 0 & 0 & 69774 \end{bmatrix} \cdot \begin{bmatrix} O_{Fz} \\ O_{Tz} \\ O_{My} \\ O_{Mx} \end{bmatrix} \quad (3.25)$$

To elaborate, since the output of the NI 9237 module is in  $\frac{V}{V_{ex}}$ , the raw torque output  $O_{Tz}$  needs to be multiplied by the constant from the second row of Table 14:

$$T_z = \frac{75 (N.m) \times 1000 \left(\frac{mV}{V}\right)}{-1.0601 \left(\frac{mV}{V_{ex}}\right)} \times O_{Tz} \left(\frac{V}{V_{ex}}\right) = -70748 N.m \quad (3.26)$$

The calculated average cross-talk of 1.25 % can be considered in addition to other elemental sources of uncertainty such as non-linearity, hysteresis, and repeatability. For the torque measurement, elemental sources of bias uncertainty are:

$$B_{torque\ linearity} = 0.5 \times \frac{75 (N.m)}{100} = 0.375 N.m \quad (3.27)$$

$$B_{torque\ hysteresis} = 0.5 \times \frac{75 (N.m)}{100} = 0.375 N.m \quad (3.28)$$

$$B_{torque\ cross-talk} = 1.25 \times \frac{75 (N.m)}{100} = 0.938 N.m \quad (3.29)$$

$$B_{CRIO} = \left(25.9e - 6 V \times 70748 \frac{N.m}{V}\right) = 1.832 N.m \quad (3.30)$$

The latter (bias) uncertainty associated with the data acquisition system  $B_{CRIO}$  was calculated based on the method that will be discussed in 3.6 using the Equation (3.31)

where  $\frac{\partial Q}{\partial V_i}$  is the scale used to obtain torque from the measured voltage calculated in

equation (3.26), and  $\Delta V_i$  is the CRIO module uncertainty reported in Table 9:

$$\Delta Q_i = \frac{\partial Q}{\partial V_i} \Delta V_i \quad (3.31)$$

Using RSS, total bias uncertainty in torque measurement is:

$$B_{torque} = (0.375^2 + 0.375^2 + 0.938^2 + 1.832^2)^{1/2} = 2.125 \text{ N.m} \quad (3.32)$$

While precision uncertainty can be calculated as:

$$P_{torque \text{ repeatability}} = 0.02 \times \frac{75 \text{ (N.m)}}{100} = 0.015 \text{ N.m} \quad (3.33)$$

Standard deviation of the averaged test data reported in Table 10 was:

$$SEM = 0.005 \text{ N.m}$$

Hence, using RSS, total standard deviation is:

$$P_{torque} = 2S_T = 2 \times (0.015^2 + 0.005^2)^{1/2} = 0.032 \text{ N.m} \quad (3.34)$$

Finally, the total uncertainty in torque measurement can be calculated as:

$$U_{torque} = (B_{torque}^2 + P_{torque}^2)^{1/2} = 2.126 \text{ N.m} \quad (3.35)$$

This value is the total uncertainty when the full rated load of 75 N.m is applied which translates into a 2.8 % full scale uncertainty. Using the cross-talk correction matrix, this value can be reduced. Uncertainty associated with the thrust force and the other two moments can be quantified using the same procedure. Uncertainty in the thrust force was calculated to be 36.626 N.m which translates into a 4 % full scale uncertainty. This rather high level of uncertainty is primarily due to the high range of the sensor (900 N).

### 3.5.2 Cup Wind Speed

Based on the NRG systems uncertainty document, the combined precision and bias uncertainty of an anemometer can be characterized by a classification number, a dimensionless index representing the maximum error, derived from experimental and modeling methods [54]. Anemometer dynamic effects, angular characteristics, and bearing friction are measured under laboratory-controlled conditions in order to assign a

classification number and are fed into a dynamic model of the anemometer used to bound the errors, subject to influence parameters (e.g., turbulence intensity, off-axis wind, and ambient temperature) [54]. Subsequently, the anemometer operational standard uncertainty can be derived from the classification number associated with the anemometer. In IEC 61400-12-1, Equation (3.36) is used to calculate the standard uncertainty, which is based on the wind speed bin  $U_i$  and classification number  $k$ , which is 2.4 for a NRG #40 in a flat terrain [54]:

$$u_i = (0.05 + 0.005 \times U_i) \frac{k}{\sqrt{3}} \quad (3.36)$$

Otech Engineering quantified the NRG #40 cup anemometer uncertainty through calibration uncertainty comparisons between various anemometers [55]. According to that study, the calibration uncertainty of the device is  $\pm 1.48\%$  of the reading. Moreover, as mentioned by the manufacturer, the operational standard uncertainty (IEC 61400-12-1) at 10 m/s is  $\pm 0.14$  m/s and  $\pm 0.45$  m/s, for classes A and B respectively [54]. Classes A and B are characterized based on the operational ranges as discussed in [54].

Total bias uncertainty in cup wind speed measurement includes the uncertainties caused by the CRIO and the cup anemometer itself. Bias uncertainty from the CRIO can be neglected as the measurement is measured using the NI CRIO 9411 digital module, based on the frequency of the square wave signal. Bias uncertainty of the cup anemometer can be calculated using [55]:

$$B_{cup\ speed} = 1.48 \times \frac{16.258\ (m/s)}{100} = 0.241\ m/s \quad (3.37)$$

Standard deviation of the averaged test data was:

$$P_{cup\ speed} = 2SEM = 0.036\ m/s \quad (3.38)$$

Total uncertainty in cup wind speed measurement can be calculated as:

$$U_{cup\ speed} = (B_{cup\ speed}^2 + P_{cup\ speed}^2)^{1/2} = 0.244\ m/s \quad (3.39)$$

### 3.5.3 Ultrasonic Measurands

Specifications of the ultrasonic anemometer provided by the manufacturer are summarized in Table 17 [22].

**Table 17.** Ultrasonic anemometer uncertainty

Wind speed	Range	0 to 40 m/s (0 to 90 mph)
	Resolution	0.01 m/s
	Threshold	0.01 m/s
	Uncertainty	± 1% ± 0.05 m/s (0 to 30 m/s) ± 3% (30 to 40 m/s)
Direction and Elevation	Azimuth range	0.0 to 359.9 degrees
	Elevation range	± 60.0 degrees
	Resolution	0.1 degree
	Uncertainty	± 2° (0 to 30 m/s) ± 5° (30 to 40 m/s)
Speed of Sound	Range	300 to 360 m/s
	Resolution	0.01 m/s
	Uncertainty	±0.1 ± 0.05 m/s (0 to 30 m/s wind)
Sonic Temperature	Range	-50 to +50 C°
	Resolution	0.01 C°
	Uncertainty	±2 C° (0 to 30 m/s wind)

Assuming that the reported uncertainty includes all bias elemental sources, the total bias uncertainty in wind speed measurements can be calculated as:

$$B_{sonic\ speed} = 1 \times \frac{16.760\ (m/s)}{100} + 0.05 = 0.218\ m/s \quad (3.40)$$

The precision uncertainty considering the standard deviation of the mean (Table 12) is:

$$P_{sonic\ speed} = 2S_T = 2SEM = 2 \times 0.038 = 0.076\ m/s \quad (3.41)$$

And the total uncertainty will be:

$$U_{sonic\ speed} = (B_{sonic\ speed}^2 + P_{sonic\ speed}^2)^{1/2} = 0.231\ m/s \quad (3.42)$$

Uncertainty associated with wind direction, wind elevation, speed of sound, and sonic temperature can be quantified using the same procedure.

### 3.5.4 Vane Wind Direction

According to the manufacturer specification, potentiometer non-linearity (bias uncertainty source) is within 1 %, maximum deadband (bias uncertainty source) is 8°, typical deadband is 4°, and the threshold is 1 m/s [31]. For a potentiometer wind direction vane, deadband is the range of directions for which the output signal is undefined [30]. Considering the maximum deadband for the 200P vane, the defined electrical range is from 4° to 356°. Neglecting the deadband compensation (assuming the 0° to 359°) leads to scaling error as readings approach the deadband from either side and is the worst at the edge of the deadband [30]. On the other hand, when the deadband compensation is considered, the deadband uncertainty is minimized [30]. In this case, the highest and the lowest reading would be 356° and 4° respectively and any readings within the deadband (356° to 4°) will be reported as 0° [30]. Considering the points mentioned, for a 10 V excitation (excluding deadband), the transfer function can be calculated as:

$$Wind\ direction\ (^{\circ}) = Voltage\ reading \times 36 \pm 3.6 \quad (3.43)$$

### 3.5.5 Temperature and Relative Humidity (RH)

Specifications provided by the manufacturer are summarized in Table 18 [33]. As can be seen from the table, one elemental bias uncertainty for the temperature is  $\pm 0.4\ C^{\circ}$  while considering the maximum RH, the associated bias uncertainty would be  $\pm 0.8\ \%$ , which

translates into an uncertainty of 0.008 when considering the relative humidity in a fraction between 0 and 1, as required for the air density calculation.

**Table 18.** Relative humidity and temperature uncertainty [33]

Relative Humidity	Range	0 to 100 % RH
	Resolution	0.02 %
	Output	0 to 1 VDC
	Typical Long Term Stability	less than 1 % RH/year
	Response Time	3 to 12 seconds
	Uncertainty at 23 C°	± 0.8 % RH (23 C°)
Temperature	Range	-40 to +60 C°
	Resolution	0.1 C°
	Output	0 to 1 VDC
	Typical Long Term Stability	less than 0.1 C° /year
	Temperature Uncertainty	-50 to +50 C°: ± 0.1 C° (0 C°)
		-50 to +60 C°: ± 0.4 C°

An R. M. Young 41003-5 multiple-plate radiation shield accommodates and protects the temperature and RH sensors from errors associated with solar radiation and precipitation up to 26 mm (1 in) diameter. According to the manufacturer [34], the radiation bias uncertainty associated with the shield depends on the wind speed. Uncertainty at 1080 W/m<sup>2</sup> intensity is summarized in Table 19.

**Table 19.** Multi-plate radiation shield uncertainty [34]

0.4 C°	3 m/s (6.7 mph)
0.7 C°	2 m/s (4.5 mph)
1.5 C°	1 m/s (2.2 mph)

As for the total bias uncertainty of temperature measurement,  $B_{Temp}$ , the RTD and shield uncertainties, and CRIO module uncertainty can be combined using RSS to be:

$$B_{Temp} = (0.4^2 + 0.4^2 + 11.84e - 6^2)^{1/2} = 0.567 C° \quad (3.44)$$

The total uncertainty in the temperature measurement  $U_{Temp}$  can then be calculated as:

$$P_{Temp} = 2 \times SEM \quad (3.45)$$

$$P_{Temp} = 2 \times 0.010 = 0.020 \text{ C}^\circ$$

$$U_{Temp} = (B_{Temp}^2 + P_{Temp}^2)^{1/2} = 0.567 \text{ C}^\circ \quad (3.46)$$

As for the relative humidity, considering the precision uncertainty based on the standard deviation of the mean and neglecting the CRIO uncertainty, the total uncertainty  $U_{RH}$  can then be calculated as:

$$B_{RH} = 0.008 \quad (3.47)$$

$$P_{RH} = 2 \times SEM \quad (3.48)$$

$$P_{RH} = 2 \times 0.020 = 0.040$$

$$U_{RH} = (B_{RH}^2 + P_{RH}^2)^{1/2} = 0.041 \quad (3.49)$$

### 3.5.6 Pressure

According to the manufacturer [32], bias uncertainty of this barometric pressure sensor is reported to be  $\pm 0.3$  hPa ( $\pm 0.2$  hPa at  $25 \text{ C}^\circ$ ). This device uses ASCII serial output format with an update rate of 1.8 Hz, upon a 10-sample averaging which will be neglected in this uncertainty study.

**Table 20.** Pressure sensor uncertainty [32]

Pressure Range	500 to 1100 hPa
Resolution	0.1 hPa
Temperature Range	-50 to 60 $\text{C}^\circ$
Output Rate	1.8 Hz (max) to 1 per minute (software selectable)
Total Uncertainty	$\pm 0.3$ hPa
Serial Output	9600 baud, 8 bit, 1 stop bit, no parity, continuous ASCII text

Considering the precision uncertainty based on the standard deviation of the mean, the total uncertainty  $U_{Pres}$  will be:

$$B_{Pres} = 0.3 \text{ hPa} \quad (3.50)$$

$$P_{Pres} = 2 \times SEM \quad (3.51)$$

$$P_{Pres} = 2 \times 0.003 = 0.006 \text{ hPa}$$

$$U_{Pres} = (B_{Pres}^2 + P_{Pres}^2)^{1/2} = 0.3 \text{ hPa} \quad (3.52)$$

### 3.5.7 Rotor Speed

Speed can be measured using the number of pulses counted inside a constant-width time window, assuming that the angular velocity is constant in it. In order to measure the rotor speed using the counter specialty mode in LabVIEW, the number of pulses per iteration loop running at the specified timed loop frequency was counted. The rotor speed in RPM at each time instant was then calculated as:

$$\text{Rotor speed [RPM]} = \frac{\left(\frac{\text{pulses}}{\text{scan}}\right) \times \left(\frac{\text{scan}}{\text{s}}\right) \times \left(\frac{60\text{s}}{\text{min}}\right)}{(\text{encoder pulses per revolution})} \quad (3.53)$$

The uncertainty associated with the shaft encoder is mainly due to quantization, which can be calculated based on the encoder pulses per revolution (PPR) and the observation time window, independent of the operating speed. Based on the high resolution of 4096 PPR of the encoder, its bias uncertainty  $B_e$  can be calculated as:

$$B_e = \frac{60}{PPR \times t_w} \quad (3.54)$$

$$B_e = \frac{60}{4096 \times 0.02} = 0.732 \text{ RPM} = 0.077 \text{ rad/s}$$

Where  $PPR$  is the encoder's resolution in pulses per revolution and  $t_w$  is the time window in seconds (0.02 seconds was used in calculation here given the sampling frequency of 50 Hz). In addition, the 512 PPR mounted on the yaw system motor results in a resolution positioning of 5.860 RPM (0.003 RPM considering the total gear reduction of 2170).

In order to quantify the precision uncertainty  $P_e$  in rotor rotational speed measurement, standard error of the mean,  $SEM^2$ , can be used as:

$$P_e = 2 \times SEM \quad (3.55)$$

$$P_e = 2 \times 0.129 = 0.258 \text{ RPM} = 0.027 \text{ rad/s}$$

The total uncertainty in rotor rotational speed  $U_e$  can then be calculated as:

$$U_e = (B_e^2 + P_e^2)^{1/2} = 0.776 \text{ RPM} = 0.081 \text{ rad/s} \quad (3.56)$$

### 3.6 Uncertainty Propagation in the Final Results (Calculable Parameters)

In this section, indirectly calculable parameters and their corresponding uncertainty will be discussed. Experimenters typically deal with data reduction which is calculating the desired experimental result by measuring several variables and via utilizing analytical formulas, spreadsheets or computer programs [45]. The main motivation is to investigate how an error estimate or uncertainty in a specific measurand affects the final results [45]. In a general case, suppose the result  $y$  be a function of  $n$  independent measured variables  $x_1, x_2, \dots, x_n$  as:

$$y = y(x_1, x_2, \dots, x_n) \quad (3.57)$$

Suppose  $\Delta x_i$  is the bias uncertainty of  $x_i$ . The associated uncertainty in  $y$  will be

$$\Delta y_i = y(x_1, x_2, x_i + \Delta x_i, \dots, x_n) - y(x_1, x_2, \dots, x_n) \quad (3.58)$$

Considering a small uncertainty and using the Taylor series expansion of the above equation (retain the first derivatives only), the resulting uncertainty in  $y$  can be calculated as:

$$\Delta y_i = \frac{\partial y}{\partial x_i} \Delta x_i \quad (3.59)$$

Moreover, considering the bias uncertainties to be independent and symmetrical with respect to either positive or negative values, the root of the sum of the squares (RSS) is again an appropriate estimate for the uncertainty and can be stated as:

$$\Delta y = \left( \sum_{i=1}^n \left| \frac{\partial y}{\partial x_i} \Delta x_i \right|^2 \right)^{\frac{1}{2}} \quad (3.60)$$

### 3.6.1 Power

Considering  $Q$  to be the rotor torque in N.m and  $\Omega$  as the rotor rotational speed in rad/s, the developed power by the rotor can be obtained [56] using

$$P = Q\Omega \quad (3.61)$$

As illustrated in Figure 29, in a constant rotational speed operation (zero angular acceleration), the rotor aerodynamic torque,  $T_{aero}$ , can be assumed equal to the loadcell measured mechanical torque,  $T_{mech}$ .

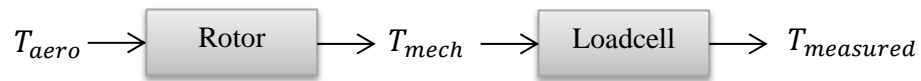


**Figure 29.** Aerodynamic torque schematic

Using the example case in Table 10 and Equation (3.60), the uncertainty associated with power measurement can be formulated as:

$$\Delta P = \left( \left( \frac{\partial P}{\partial Q} \Delta Q \right)^2 + \left( \frac{\partial P}{\partial \Omega} \Delta \Omega \right)^2 \right)^{1/2} \quad (3.62)$$

$$\Delta P = \left( (\Omega \Delta Q)^2 + (Q \Delta \Omega)^2 \right)^{\frac{1}{2}} \quad (3.63)$$

$$\Delta P_{bias} = \left( (47.139 \times 0.321)^2 + (11.316 \times 0.077)^2 \right)^{\frac{1}{2}} = 15.142 \text{ W}$$

where torque uncertainty,  $\Delta Q$ , was scaled down from rated to the mean value read.

Considering the SEM for estimating the precision uncertainty propagation in the power calculation,

$$\Delta P_{precision} = ((47.139 \times 0.0015)^2 + (11.316 \times 0.0027)^2)^{\frac{1}{2}} \quad (3.64)$$

$$\Delta P_{precision} = 0.076 \text{ W}$$

Utilizing the RSS technique, the total uncertainty in power measurement can then be formulated as:

$$U_P = (\Delta P_{bias}^2 + \Delta P_{precision}^2)^{1/2} = 15.149 \text{ W} \quad (3.65)$$

### 3.6.2 Air Density

In wind power calculations, air density is typically considered constant in time [56] as:

$$\rho = 1.25 \text{ kg/m}^3$$

However, recent studies have shown that it is worth taking the variation in time into account in order to obtain a higher accuracy in power production calculation [57]. While using the same foundation, Picard et al. in [58] revised the CIPM-81/91 formula for determination of the density of moist air to CIPM-2007 equation utilizing modern methods for determination of values such as Argon concentration obtained by various institutes and laboratories world-wide such as Korea Research Institute of Standards and Science (KRISS) and Laboratoire National de Métrologie et d'Essais (LNE, France). Frakas reported the variation in air density in a meteorological station in Győr, Hungary from 2004 to 2006 based on the CIPM-2007 equation [57]. According to the CIPM-2007 equation proposed by the International Committee for Weights and Measures [57], [58],

air density as a function of air temperature  $t$  [ $C^\circ$ ], air pressure  $p$  [Pa], and relative humidity  $h$  ( $0 \leq h \leq 1$ ) can be calculated using an equation of state as:

$$\rho(t, p, h) = \frac{pM_a}{Z(t, p, h)RT(t)} \left\{ 1 - x_v(t, p, h) \left[ 1 - \frac{M_v}{M_a} \right] \right\} \quad (3.66)$$

where  $R = 8.314472$  J/mol K is the molar gas constant,  $M_a = 28.96546 \times 10^{-3}$  kg/mol is the molar mass of dry air,  $M_v = 18.01525 \times 10^{-3}$  kg/mol is the molar mass of water,  $T(t) = (273.5 + t[C^\circ])$  K is the thermodynamic temperature, and  $x_v(t, p, h)$  is the mole fraction of water vapor which can be calculated using either the relative humidity or the dew point temperature [57]. The first step is to calculate the vapor pressure at saturation,  $P_{SV}$ , with constants listed in Table 21 as [58]:

$$p_{SV} = 1 \text{ Pa} \times \exp \left[ AT(t)^2 + BT(t) + C + \frac{D}{T(t)} \right] \quad (3.67)$$

Then, enhancement factor should be calculated using  $t$ , temperature in  $C^\circ$  as:

$$f = h[\alpha + \beta p + \gamma t^2] \quad (3.68)$$

The mole fraction of water vapor can then be calculated as

$$x_v(t, p, h) = hf(p, t) \frac{p_{SV}}{p} \quad (3.69)$$

where relative humidity has the following range:

$$0 \leq h \leq 1 \quad (3.70)$$

Substituting Equations (3.55) and (3.56) in Equation (3.57) gives:

$$x_v(t, p, h) = h[\alpha + \beta p + \gamma t^2] \frac{1 \text{ Pa} \times \exp \left[ AT(t)^2 + BT(t) + C + \frac{D}{T(t)} \right]}{p} \quad (3.71)$$

The compressibility factor  $Z(t, p, h)$  [57] is:

$$Z(t, p, h) = 1 - \frac{p}{T(t)} [a_0 + a_1 t + a_2 t^2 + [b_0 + b_1 t]x_v + [c_0 + c_1 t]x_v^2] \quad (3.72)$$

$$+ \frac{p^2}{T(t)^2} [d + ex_v^2]$$

Picard et al. in [58] recommended ranges for the pressure and temperature for CIPM-2007 are the same as CIPM-81/91:

$$600 \text{ hPa} \leq p \leq 1100 \text{ hPa} \quad (3.73)$$

$$15\text{C}^\circ \leq t \leq 27\text{C}^\circ$$

**Table 21.** CIPM-2007 constants [57]

General constants	Mole fraction of water vapor constants	Compressibility factor constants
$R = 8.314472 \text{ J/mol K}$ $M_a = 28.96546 \times 10^{-3} \text{ kg/mol}$ $M_v = 18.01525 \times 10^{-3} \text{ kg/mol}$	$A = 1.2378847 \times 10^{-5} \text{ K}^{-2}$ $B = 1.9121316 \times 10^{-2} \text{ K}^{-1}$ $C = 33.93711047$ $D = -6.3431645 \times 10^3 \text{ K}$ $\alpha = 1.00062$ $\beta = 3.14 \times 10^{-8} \text{ Pa}^{-1}$ $\gamma = 5.6 \times 10^{-7} \text{ K}^{-2}$	$a_0 = 1.58123 \times 10^{-10} \text{ KPa}^{-1}$ $a_1 = -2.9331 \times 10^{-8} \text{ Pa}^{-1}$ $a_2 = 1.1043 \times 10^{-10} \text{ K}^{-1} \text{ Pa}^{-1}$ $b_0 = 5.707 \times 10^{-6} \text{ KPa}^{-1}$ $b_1 = -2.051 \times 10^{-8} \text{ Pa}^{-1}$ $c_0 = 1.9898 \times 10^{-4} \text{ KPa}^{-1}$ $c_1 = -2.376 \times 10^{-6} \text{ Pa}^{-1}$ $d = 1.83 \times 10^{-11} \text{ K}^2 \text{ Pa}^{-2}$ $e = -0.765 \times 10^{-8} \text{ K}^2 \text{ Pa}^{-2}$

In order to simplify the air density calculation, the enhancement factor and compressibility factor can be assumed to be 1. Based on the definition of relative humidity, the mole fraction of water vapor can then simply be calculated as:

$$x_v(t, p, h) = h \frac{p_{sv}}{p} = \frac{p_v}{p_{sv}} \frac{p_{sv}}{p} = \frac{p_v}{p} \quad (3.74)$$

Considering the molar gas, molar mass of dry air, and molar mass of water constants, the air density can then be calculated as:

$$\rho(t, p, h) = \frac{p}{287.05T} \left(1 - 0.378 \left(\frac{p_{sv}}{p}\right) h\right) \quad (3.75)$$

Where  $p_{SV}$ , the saturation pressure of water vapor in Pascal can be estimated using the temperature in  $C^\circ$  as [58, 59]:

$$p_{SV} = 6.1078 \times 10^{\left(\frac{7.5t}{273.3+t}\right)} \quad (3.76)$$

Finally, the air density can be calculated as:

$$\rho(t, p, h) = \frac{p}{287.05(t + 273.15)} \left(1 - \left(\frac{2.3087 \times 10^{\left(\frac{7.5t}{273.3+t}\right)} h}{p}\right)\right) \quad (3.77)$$

For each actual test run, the mean values of temperature, relative humidity, and pressure can be obtained and input into Equation (3.77) to calculate the air density. Based on data presented in Table 11, calculated air density was  $1.249 \text{ Kg/m}^3$ . Using Equation (3.60), the uncertainty in air density measurement can be formulated as:

$$\Delta\rho = \left( \left(\frac{\partial\rho}{\partial t} \Delta t\right)^2 + \left(\frac{\partial\rho}{\partial h} \Delta h\right)^2 + \left(\frac{\partial\rho}{\partial P} \Delta P\right)^2 \right)^{1/2} \quad (3.78)$$

To obtain the analytic differentiation equations, MuPad from MATLAB's symbolic math toolbox was used. Gradients for the temperature in degrees Celsius, the relative humidity in fraction, and the power in Watts were derived to be:

$$\begin{aligned} \frac{\partial\rho}{\partial t} = & \frac{287.05 P \left( \frac{2.3087 \times 10^{\left(\frac{7.5t}{273.3+t}\right)} h}{p} - 1 \right)}{(287.05 t + 78407.7075)^2} \\ & + \frac{2.3087 \times 10^{\left(\frac{7.5t}{273.3+t}\right)} h \ln(10) \left( \frac{7.5 t}{(273.3 + t)^2} - \frac{7.5}{273.3 + t} \right)}{287.05 t + 78407.7075} \end{aligned} \quad (3.79)$$

$$\frac{\partial \rho}{\partial h} = -\frac{2.3087 \times 10^{\left(\frac{7.5t}{273.3+t}\right)}}{287.05 t + 78407.7075} \quad (3.80)$$

$$\frac{\partial \rho}{\partial p} = -\frac{2.3087 \times 10^{\left(\frac{7.5t}{273.3+t}\right)} h}{p (287.05 t + 78407.7075)} - \frac{2.3087 \times 10^{\left(\frac{7.5t}{273.3+t}\right)} h}{p} - 1 \quad (3.81)$$

Based on the values obtained from these equations and calculated uncertainty in the measurands, the precision uncertainty was negligible when using the corresponding SEM. The total bias uncertainty in air density measurement (neglecting the uncertainty associated with the CIPM equation and the simplification process used) was calculated using Equation (3.66) as:

$$U_{\rho} \cong \Delta \rho_{bias} = ((-0.044 \times 0.567)^2 + (1.216e - 5 \times 0.008)^2 + (-6.275e - 5 \times 0.3)^2)^{1/2} = 0.0025 \text{ kg/m}^3 \quad (3.82)$$

### 3.6.3 Power Coefficient

One of the experimental goals of wind turbine testing is to obtain the power and subsequently attain the power coefficient versus tip speed ratio performance curve. The power coefficient  $C_p$  can be calculated [56] as:

$$C_p = \frac{P}{\frac{1}{2} \rho U_{\infty}^3 \pi R^2} \quad (3.83)$$

where  $P$  is the mechanical (in this case) or electrical power developed by the wind turbine rotor (W),  $\rho$  is the density of air ( $\text{kg/m}^3$ ),  $U_{\infty}$  is the free stream wind speed (m/s), and  $R$  is the rotor blade radius (m). Based on the measured values of rotor torque and

speed, temperature, pressure, relative humidity, and the free-stream velocity, bias uncertainty in the power coefficient can be calculated using:

$$\Delta C_P = \left( \left( \frac{\partial C_P}{\partial P} \Delta P \right)^2 + \left( \frac{\partial C_P}{\partial \rho} \Delta \rho \right)^2 + \left( \frac{\partial C_P}{\partial U_\infty} \Delta U_\infty \right)^2 \right)^{1/2} \quad (3.84)$$

where

$$\frac{\partial C_P}{\partial P} = \frac{2}{\rho U_\infty^3 \pi R^2} \quad (3.85)$$

$$\frac{\partial C_P}{\partial \rho} = -\frac{2P\rho^{-2}}{U_\infty^3 \pi R^2} \quad (3.86)$$

$$\frac{\partial C_P}{\partial U_\infty} = -\frac{6PU_\infty^{-4}}{\rho \pi R^2} \quad (3.87)$$

Based on the reported data and the estimated total uncertainty in power, air density, and cup wind speed measurements, the total bias uncertainty propagating in the power coefficient measurement was calculated using Equation (3.84) as:

$$\begin{aligned} \Delta C_{P_{bias}} &= \left( (1.549e - 4 \times 15.769)^2 + (-0.066 \times 0.025)^2 \right. \\ &\quad \left. + (-0.015 \times 0.241)^2 \right)^{1/2} = 0.0044 \end{aligned} \quad (3.88)$$

Propagation of precision uncertainty (using SEM) can be calculated using the same method:

$$\begin{aligned} \Delta C_{P_{precision}} &= \left( (1.549e - 4 \times 0.076)^2 + (-0.066 \times 0.013)^2 \right. \\ &\quad \left. + (-0.015 \times 0.036)^2 \right)^{1/2} = 0.001 \end{aligned} \quad (3.89)$$

Utilizing the RSS technique, the total uncertainty in power coefficient calculation can be formulated as:

$$U_{C_P} = \left( \Delta C_{P_{bias}}^2 + \Delta C_{P_{precision}}^2 \right)^{1/2} = 0.0045 \quad (3.90)$$

### 3.6.4 Thrust Coefficient

Another performance curve of interest is the thrust coefficient versus tip speed ratio curve. Based on the thrust force,  $T$ , the thrust coefficient is defined as [56]:

$$C_T = \frac{T}{\frac{1}{2} \rho U_\infty^2 \pi R^2} \quad (3.91)$$

Taking into account the CIPM-2007 equation and based on the readings of the thrust force, temperature, pressure, relative humidity, and the free-stream velocity, the bias uncertainty of the thrust coefficient can be formulated as:

$$\Delta C_T = \left( \left( \frac{\partial C_T}{\partial T} \Delta T \right)^2 + \left( \frac{\partial C_T}{\partial \rho} \Delta \rho \right)^2 + \left( \frac{\partial C_T}{\partial U_\infty} \Delta U_\infty \right)^2 \right)^{1/2} \quad (3.92)$$

where

$$\frac{\partial C_T}{\partial T} = \frac{2}{\rho U_\infty^2 \pi R^2} \quad (3.93)$$

$$\frac{\partial C_T}{\partial \rho} = -\frac{2P\rho^{-2}}{U_\infty^2 \pi R^2} \quad (3.94)$$

$$\frac{\partial C_T}{\partial U_\infty} = -\frac{4PU_\infty^{-3}}{\rho \pi R^2} \quad (3.95)$$

Considering thrust uncertainty converted from full scale to the mean value read, using reported test data as well as the estimated total uncertainty in air density and cup wind speed measurements, the total bias uncertainty in thrust coefficient measurement was calculated using Equation (3.92) to be:

$$\begin{aligned} \Delta C_{T_{bias}} &= ((0.0025 \times 3.281)^2 + (-1.075 \times 0.0025)^2 \\ &+ (-0.165 \times 0.241)^2)^{1/2} = 0.041 \end{aligned} \quad (3.96)$$

SEM-based propagation of precision uncertainty can be calculated using:

$$\begin{aligned} \Delta C_{T_{precision}} &= ((0.0025 \times 1.082)^2 + (-1.075 \times 0.013)^2 \\ &+ (-0.165 \times 0.036)^2)^{1/2} = 0.016 \end{aligned} \quad (3.97)$$

Finally, using the RSS technique, the total uncertainty in thrust coefficient calculation can be formulated as:

$$U_{C_T} = \left( \Delta C_{T_{bias}}^2 + \Delta C_{T_{precision}}^2 \right)^{1/2} = 0.044 \quad (3.98)$$

### 3.6.5 Tip speed ratio (TSR)

The tip speed ratio  $\lambda$  is defined as the ratio of the blade tip speed and free-stream wind velocity [56]:

$$\lambda = \frac{R\Omega}{U_\infty} \quad (3.99)$$

The uncertainty in the tip speed ratio calculation can be formulated as:

$$\Delta\lambda = \left( \left( \frac{\partial\lambda}{\partial U_\infty} \Delta U_\infty \right)^2 + \left( \frac{\partial\lambda}{\partial \Omega} \Delta \Omega \right)^2 \right)^{1/2} \quad (3.100)$$

which takes the form:

$$\Delta\lambda = \left( \left( -\frac{R\Omega}{U_\infty^2} \Delta U_\infty \right)^2 + \left( \frac{R}{U_\infty} \Delta\Omega \right)^2 \right)^{\frac{1}{2}} \quad (3.101)$$

Based on the reported data and the estimated total uncertainty in cup wind speed as well as rotor speed measurements, the total bias uncertainty in the tip speed ratio was calculated using Equation (3.101) as:

$$\Delta\lambda_{bias} = ((-0.156 \times 0.244)^2 + (0.054 \times 0.077)^2)^{\frac{1}{2}} = 0.038 \quad (3.102)$$

Again considering the SEM for estimating the propagation of precision uncertainty:

$$\Delta\lambda_{precision} = ((-0.156 \times 0.036)^2 + (0.054 \times 0.027)^2)^{\frac{1}{2}} = 0.006 \quad (3.103)$$

Finally, the total uncertainty in the tip speed ratio calculation can be formulated using the RSS technique as:

$$U_\lambda = (\Delta\lambda_{bias}^2 + \Delta\lambda_{precision}^2)^{1/2} = 0.038 \quad (3.104)$$

### 3.7 Uncertainty Analysis Summary

Based on the sample test results presented in Table 10, the uncertainty analysis results associated with both measurable and calculable parameters were summarized in Table 22, Table 23, and Table 24, considering three cases, namely: SD-based, SEM1-based, and SEM2-based precision uncertainty estimation. It was of interest to investigate the extent to which the implementation of the standard error of the mean impacts the precision uncertainty quantification.

As discussed in 3.4, considering four-second-averaged data points, SD-based analysis corresponds to the case of considering the standard deviation itself. SEM1-based analysis pertains to consideration of the standard error of the mean for precision uncertainty

estimation based on the size of four-second-averaged data points. SEM2-based analysis was also conducted considering the standard error of the mean, this time considering the number of the four-second-averaged data points.

As the temperature, relative humidity, and pressure measurements were reported based on a full run, only one case of standard error of the mean was considered, compared against the standard deviation. Moreover, the ultrasonic wind speed data was cut from a full run such that it can be used as a reference for the cup anemometer wind speed readings.

**Table 22.** SD-based uncertainty analysis summary

Parameter	Unit	Range	Bias Uncertainty	SD-based Precision Uncertainty	SD-based Total Uncertainty	SD-based % Full-scale Uncertainty
<b>Measurable</b>						
Torque	N.m	75	2.125	0.140	2.129	2.84
Thrust	N	900	36.626	15.308	39.696	4.41
Wind speed (cup)	m/s	96	0.241	0.506	0.560	0.58
Wind speed (sonic)	m/s	40	0.218	1.512	1.528	3.82
Temperature	C°	100	0.567	3.048	3.100	3.10
Relative Humidity	-	1	0.008	0.058	0.059	5.90
Pressure	hPa	600	0.300	0.150	0.335	0.06
Rotor speed	Rad/s	50	0.077	0.364	0.372	0.74
<b>Calculable</b>						
Power	W	-	15.142	1.078	15.180	-
Air density	Kg/m <sup>3</sup>	-	0.003	0.013	0.013	-
Power coefficient	-	-	0.004	0.008	0.009	-
Thrust coefficient	-	-	0.041	0.093	0.102	-
Tip speed ratio	-	-	0.038	0.079	0.088	-

The bias uncertainty reported for the directly measurable parameters are expected to be consistent in the future experiments. On the other hand, the bias uncertainty propagated in the calculable parameters as well as the precision uncertainties of both measurable and calculable parameters will vary in each test as the uncertainty propagation in the calculable parameters is a function of the gradients and the mean measured value of independent parameters.

**Table 23.** SEM1-based uncertainty analysis summary

Parameter	Unit	Range	Bias Uncertainty	SEM1- based Precision Uncertainty	SEM1- based Total Uncertainty	SEM1-based % Full-scale Uncertainty
<b>Measurable</b>						
Torque	N.m	75	2.126	0.010	2.125	2.83
Thrust	N	900	36.626	1.082	36.642	4.07
Wind speed (cup)	m/s	96	0.241	0.036	0.244	0.25
Wind speed (sonic)	m/s	40	0.218	0.076	0.231	0.58
Temperature	C°	100	0.567	0.020	0.567	0.57
Relative Humidity	-	1	0.008	0.000	0.008	0.80
Pressure	hPa	600	0.3	0.006	0.300	0.05
Rotor speed	Rad/s	50	0.077	0.026	0.081	0.16
<b>Calculable</b>						
Power	W	-	15.142	0.076	15.142	-
Air density	Kg/m <sup>3</sup>	-	0.003	0.000	0.003	-
Power coefficient	-	-	0.005	0.001	0.005	-
Thrust coefficient	-	-	0.041	0.016	0.044	-
Tip speed ratio	-	-	0.038	0.006	0.038	-

**Table 24.** SEM2-based uncertainty analysis summary

Parameter	Unit	Range	Bias Uncertainty	SEM2- based Precision Uncertainty	SEM2- based Total Uncertainty	SEM2-based % Full-scale Uncertainty
<b>Measurable</b>						
Torque	N.m	75	2.125	0.098	2.127	2.84
Thrust	N	900	36.626	10.824	38.192	4.24
Wind speed (cup)	m/s	96	0.241	0.358	0.432	0.45
Wind speed (sonic)	m/s	40	0.218	0.076	0.231	0.58
Temperature	C°	100	0.567	0.020	0.567	0.57
Relative Humidity	-	1	0.008	0.000	0.008	0.80
Pressure	hPa	600	0.300	0.006	0.300	0.05
Rotor speed	Rad/s	50	0.077	0.258	0.269	0.54
<b>Calculable</b>						
Power	W	-	15.142	0.762	15.161	-
Air density	Kg/m <sup>3</sup>	-	0.003	0.000	0.003	-
Power coefficient	-	-	0.004	0.006	0.007	-
Thrust coefficient	-	-	0.041	0.055	0.069	-
Tip speed ratio	-	-	0.038	0.046	0.060	-

As discussed in 3.2.1, standard deviation of the mean demonstrates how far the sample mean is likely to be from the actual population mean, as opposed to the standard deviation which merely informs us how individuals within a sample differ from the

sample mean. Hence, the standard error of the mean should be used to estimate the precision uncertainty. Obviously, an increase in the sample size will lead into a reduction in the precision uncertainty. However, using the exact same sample data, an experimenter might consider different  $n$  values in Equation (3.4) to post process the raw data, resulting in a difference in the standard deviation of the mean values.

For example, consider the case of wind speed measurement using the current test rig where the speed is sampled at 50 Hz. To post-process and calculate the final dimensionless performance parameters, we can first perform a 4-second averaging. Then, the four-second-averaged data points (e.g.  $n = 3$ ) can be analyzed further and be averaged to report the final mean value. Now, if one considers the sample size of  $n = 200$  (number of the data points used for the four-second averaging, SEM1), the precision uncertainty in wind speed will be only 0.036 m/s as shown in Table 23. On the other hand, considering a case of having three 4-second-averaged data points (SEM2), the precision uncertainty will be 0.358 m/s as presented in Table 24.

It is apparent that considering the total number of raw data points ( $n = 600$ ) used to report the mean wind speed associated with this test run will result in reduced uncertainty compared to SEM1. Furthermore, choosing a coarser/finer initial averaging window will alter both SEM1 and SEM2 results. In this study, the SEM2-based data was used for a conservative uncertainty analysis. A script was developed in MATLAB, incorporating all the equations presented in this chapter, adding an automated data post-processing capability to the application.

## Chapter 4: Wind Turbine Controls

Control systems are fundamental elements of a modern wind turbine as they assist with increasing its energy capture while decreasing the dynamic loads in the presence of turbulent wind inflows [56]. In general, the wind turbine control system consists of a number of sensors, a number of actuators, and a system consisting of hardware and software which processes the input signals from the sensors and generates output signals for the actuators [56].

On the system developed for the test rig under study, these sensors include a shaft encoder, yaw encoder, cup and ultrasonic anemometers, wind vane, loadcell, and control switches. The electric vehicle controller coupled with the CompactRIO, the PMAC generator and the battery bank make up the electrical generator which can be considered to be a torque actuator (the other potential capability yet to be used is the yaw motor).

The main objective of this study was to modify the instrumentation and subsequently utilize all these components along with the NI LabVIEW (2012, SP1) software to develop and implement a custom closed loop control system for the test rig, meeting the desired objectives of full variable-speed control of such a wind energy system.

In this chapter, upon presenting a brief background on wind turbine control fundamentals, the step-by-step procedure used to develop a custom control system for the test rig will be explained. The LabVIEW GUI and the control cabinet interface (CTRL in Figure 26 ) work instructions, developed for future operators, will be presented in Appendix B.

## **4.1 Basics of Wind Turbine Control**

The wind turbine controls have multiple layers. The Supervisory Control and Data Acquisition (SCADA) is responsible for feedback and control of an entire wind farm, while the supervisory controller is responsible for transitions between operational states of a turbine [59]. For instance, these states can be stand-by, start-up, power production, and shut-down [59]. On the next level, within a given state, closed-loop Controllers automatically adjust the operational state of turbine to follow pre-defined operating curves or setpoints [59]. Three common controllers used in practice are blade pitch (turning the angle of attack of the blades in or out of wind) controller, generator torque controller, and yaw error controller (responsible for the orientation of the wind turbine rotor in or out of wind) [60]. Independent from the other controller elements that make up the 'normal' controls of a wind turbine; a safety system is required to bring the turbine to a safe condition in the event of an emergency or fault conditions [56].

The focus of this chapter is to explain the design and implementation procedure of a generator torque controller successfully tested to regulate the rotational speed of the test rig's variable-speed system.

### **4.1.1 Rotor Speed Choices: Fixed- and Variable-Speed**

As shown in Figure 30, the most effective operation of a wind turbine rotor is at a particular tip speed ratio that gives the maximum power coefficient (defined in 3.6.3 and 3.6.5) [56]. Consequently, fixed-speed turbines, which function at a fixed rotational speed, operate optimally only at the rated wind speed [56]. In a variable-speed turbine on the other hand, the energy capture can be increased through varying the rotational speed

so that the turbine operate at the optimum tip speed ratio over a range of wind speeds [56]. In addition to enhancing power capture, there are other major benefits in utilizing a variable speed turbine such as a reduction in noise level (through operating at lower tip speeds in low winds) and a reduction in mechanical loads [56].

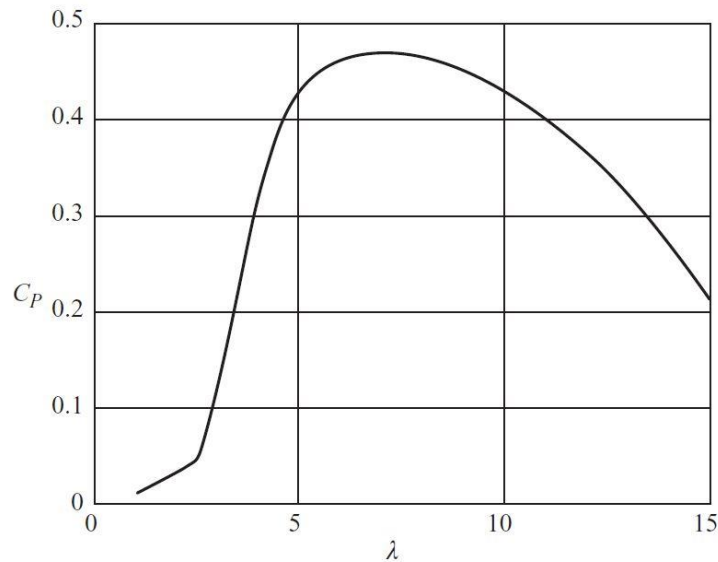


**Figure 30.** Performance curve for a modern three-blade turbine [56]

#### 4.1.2 Power Curve and Control Regions

As illustrated in the power curve (power versus wind speed curve) depicted in Figure 31, wind turbine control is defined over three basic regions characterized by three wind speeds: cut-in wind speed, rated wind speed, and cut-out wind speed. The cut-in wind speed (e.g. 5 m/s) is the speed at which the turbine starts to operate and produce power. At rated wind speed (e.g. 12-14 m/s), the turbine is expected to generate the rated power. For wind speeds above this rated speed, the power output needs to be limited using the control methods to avoid overheating the generator and potential rotor run away. The cut-out wind speed (e.g. 23-25 m/s) is the maximum speed allowed (to prevent overloads and damage to the components) for the wind turbine operation prior to shut down [62]. In

region II, between cut-in and rated wind speeds, the turbine operates at the highest efficiency possible, typically by varying the rotor rotational speed to maintain optimum tip speed ratio (to track maximum power) at a fixed (optimum) pitch. In region III, between rated and cut-out, the power transmitted to the drivetrain is held constant at rated, usually by pitching the blades out of wind (to feather) and some variable speed control to limit load. Finally, the turbine stops in extreme winds above cut-out wind speeds (parking mode). In general, a modern utility-scale turbine extracts around 50 % of the power in the wind (cubically correlated to the wind speed) below rated, compared to the maximum theoretical extractable power of 59 % referred to as Betz Limit [62].

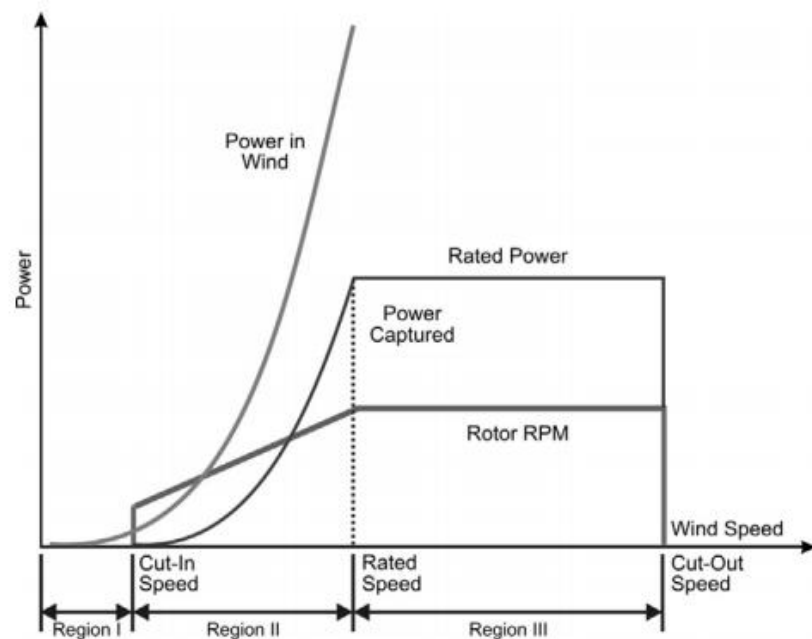


**Figure 31.** Power curve of a variable-speed wind turbine [62]

## 4.2 Power Control Methods

As rotors are designed to match a maximum installed generator capacity, the aerodynamic input power must be controlled to avoid overloading the generator and

rotors inherent run away [56]. Power control methods including passive stall, active pitch, passive pitch, passive stall, and yaw control will be reviewed in this section.

#### **4.2.1 Passive Stall Control**

Being the simplest power control method, passive stall control makes use of the post-stall reduction in lift coefficient and corresponding increase in drag coefficient to restrict the power output as the wind speed becomes excessive, while maintaining a constant rotor speed [56]. In this method, the blade pitch is fixed to reach maximum rated power at the rated wind speed. There are a number of drawbacks for this method such as the uncertainties in post-stall aerodynamic behaviour, resulting in inaccuracy in power level predictions as well as blade loadings at rated wind speed and above [56].

#### **4.2.2 Active Pitch Control**

In active pitch control, power is limited above rated wind speed through a process referred to as pitching to feather (PTF), in which all or part of each blade is rotated about its axis in the direction which reduces the angle of attack, hence decreasing the lift coefficient [56]. The main advantages of this method are increased predictability and energy capture (e.g. approximately 2.7 % more energy capture compared to stall regulation for a 7.5 m/s annual wind speed), the aerodynamic braking facility, and reduced extreme loads on the turbine when shut-down [56]. The power curves of (1) stall-regulated, fixed-speed, (2) pitch-regulated, fixed-speed, and (3) pitch-regulated, variable-speed 1.5 MW rated machines are compared in Figure 32. The latter machine would produce 5 % more energy compared to the case of having a fixed-speed, pitch-regulated machine [56].

Pitch actuation systems which can be either electrical or hydraulic can be classified into those in which each blade has its own actuator, known as individual/independent pitch control, and those in which a single actuator pitches all the blades, referred to as collective pitch control [56].

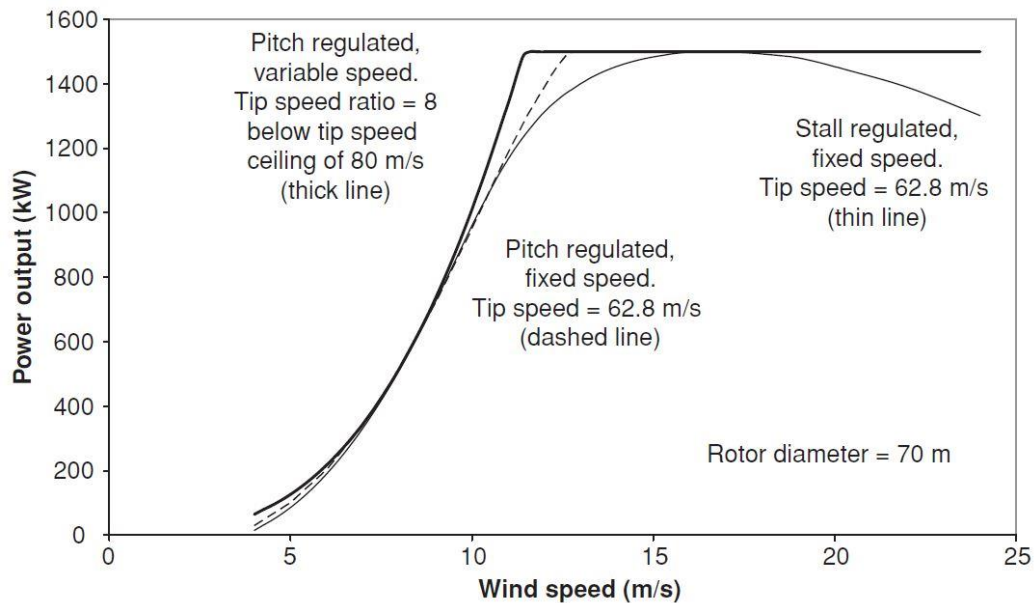


**Figure 32.** Power curve comparison of 1.5 MW rated machines [56]

#### 4.2.3 Passive Pitch Control

In passive pitch control, the blade and/or its hub mounting are designed to twist under the action of loads on the blades to achieve the desired pitch variations in high wind speeds to limit the power [56]. In practice, the required variation in blade twist with wind speed often does not match the corresponding variation in blade load, making this method a hard choice to implement [56]. This method is suitable for the application in which the optimization of energy yield is not the main objective, such as in stand-alone applications. In these applications, typically a spring-mass pitch mechanism is utilized in which as the centrifugal load on the tip exceeds the pre-load in high winds, the blades are driven outwards against the spring and are pitched.

#### **4.2.4 Active Stall Control**

In active stall control, power limitation above rated wind speed is achieved through pitching the blades into stall referred to as pitch to stall (PTS) or negative pitch control (compare to PTF as a positive pitch control). To maintain the rated power output at high winds, the blades are usually pitched back towards feather [56]. The main advantage of this method is a reduction in fatigue loads and required pitch angles demand. On the other hand, the uncertainty in predicting aerodynamic behaviour in stalled flow conditions is the main challenge in implementing this control method [56].

#### **4.2.5 Yaw Control**

In most HAWTs, a yaw actuator is responsible for keeping the turbine headed into the wind. A reversed strategy can be used to control the turbine out of the high winds theoretically [56]. However, a rapid response of a yaw control system is not possible due to the large moment of inertia of the nacelle and rotor about the yaw axis and the cosine relationship between the component of wind speed orthogonal to the rotor disc and yaw angle [56]. This relationship means that a yaw change of  $10^\circ$ , only reduces the power by a few percent compared to the blade pitch which can easily halve the power output with the same magnitude [56]. Active yaw control is only applicable in variable speed machines.

### **4.3 Braking Systems**

In general, various standards require at least two independent braking systems for safe wind turbine control in all states, which normally includes both aerodynamic and mechanical braking mechanisms [56]. In a general case of having independent aerodynamic braking systems on each blade with a rotor deceleration capability, the

mechanical brake will only be used to bring the rotor to rest (parking) [56]. In addition, a generator braking mechanism can also be counted as an electrical braking system mostly used in small wind turbines by shorting the generator windings in PMACs.

#### **4.4 Test Rig Control System**

As mentioned previously, the test rig can be used in two scenarios of track and stationary tests based on the following rotor speed control objectives:

1. During the steady (track) test runs, the rotor rotational speed is held constant, to maintain a nominally constant tip speed ratio while the trailer is being driven at a constant velocity by the towing vehicle. In reality, vehicle velocity is not perfectly steady, and hence with rotor speed held constant and fore-aft vibration of the tower affecting relative inflow velocity, tip speed ratio varies somewhat over the test.

A closed-loop control system can be implemented using the actual rotor speed measured by the shaft encoder as the feedback. In this scenario, a single power coefficient associated with the controlled tip speed ratio can be obtained. As such, a range of rotor rotational speeds and towing vehicle (wind inflow) velocities need to be prescribed to facilitate the construction of the performance curve introduced in Figure 30.

2. During testing in unsteady winds with the trailer parked (stationary), the rotor rotational speed is varied as the natural incoming wind inflow velocity changes in order to track the optimum tip speed ratio (corresponding to the maximum power coefficient) obtained from the steady state test runs. More aggressive rotor control

could also be used to proactively spin-up the rotor to actively follow or even lead wind gusts.

The controller designed to maintain the constant rotor speed in the previous step can be used in an outer/inner loop algorithm. The outer loop would track wind speed and with tip speed ratio setpoint set the rotation speed target. The inner loop would then control the rotor speed to track the outer loop's rotor speed target.

To implement the rotor speed control, a custom LabVIEW-based closed loop controller (paired with the EV controller, PMAC generator, battery bank, and the CRIO) is responsible for controlling the rotor speed through generator torque regulation. This generator torque controller and the procedure used for its development will be the focus of the rest of this chapter. A flow chart of this procedure is depicted in Figure 33.

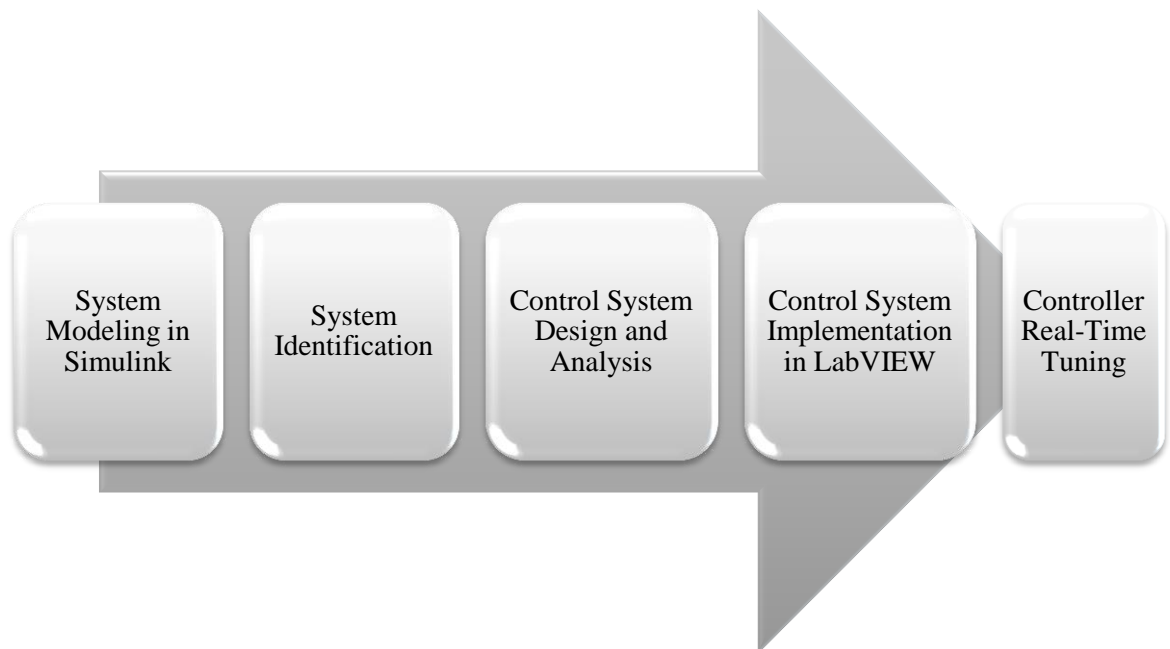


**Figure 33.** Custom control system development flow chart

Moreover, overspeed protection is assured through a separate mechanical system utilizing a spring-mass passive pitch mechanism that mechanically pitches the rotor blades above a rated rotor speed. As can be seen in Figure 34, three stainless steel blade pitching weights are mounted on the blades to pitch all three blades along their axis simultaneously at high wind speeds, while maintaining the rotor into the wind to generate power [61].

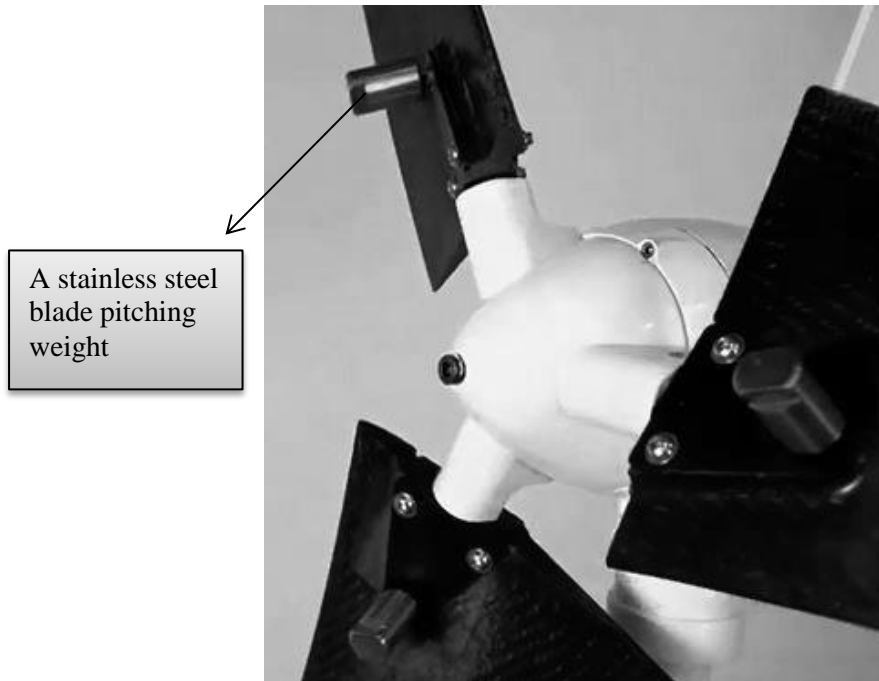


**Figure 34.** Mass-spring passive pitch control

To ensure safe operation and to conform to the standards, a parking (stop) switch located on the control cabinet of the test rig can also be utilized (as a generator braking mechanism) which shorts the three phases of the generator at the time of emergency. However, using this brake may damage the system. Additional notes on using this brake is presented in Appendix B where a work instruction for the control cabinet is discussed.

## 4.5 System Modeling in Simulink

As mentioned on the workflow illustrated in Figure 33, the first step in test rig's control system development was to model the system in Simulink within the MATLAB platform. In general, control engineers model their systems of interest to analyze the system and subsequently design a controller to improve the system performance. For this study, the main motivation for system modeling and identification was to obtain an initial guess for controller gains usable in the actual LabVIEW application.

### 4.5.1 Turbine Simulink Model

A simplified model of the turbine system was developed as illustrated in Figure 35. Both steady and unsteady wind speeds can be prescribed using a manual switch. The unsteady wind speed data can be generated using TurbSim, a stochastic, full-field, turbulent-wind simulator that uses a statistical model to numerically simulate time series of three-component wind speed vectors at points in a two-dimensional vertical rectangular grid fixed in space [63]. TurbSim output can be used as input into AeroDyn-based codes such as FAST [64], [65]. The pitch angle was assumed to be fixed at zero, neglecting the passive pitch mechanism on the real system. The rotor speed can also be set to fixed or variable using another manual switch.

Wind speed, rotor speed, and pitch angle are fed into the rotor aerodynamics subsystem depicted in Figure 36. On the rotor aerodynamics subsystem, wind and rotor speeds are used to calculate the corresponding tip speed ratio (using Equation 3.99). The tip speed ratio and pitch angle are then input into two look up tables to determine the power and thrust coefficients. These maps are obtained using Excel-BEM, a BEM-based code which

was used in the actual AmpAir600 rotor blade design developed by University of Victoria's Dr. C. Crawford. Based on the obtained coefficients, rotor power (Equation 3.83), thrust (Equation 3.91), and rotor torque (Equation 3.61) can be calculated.

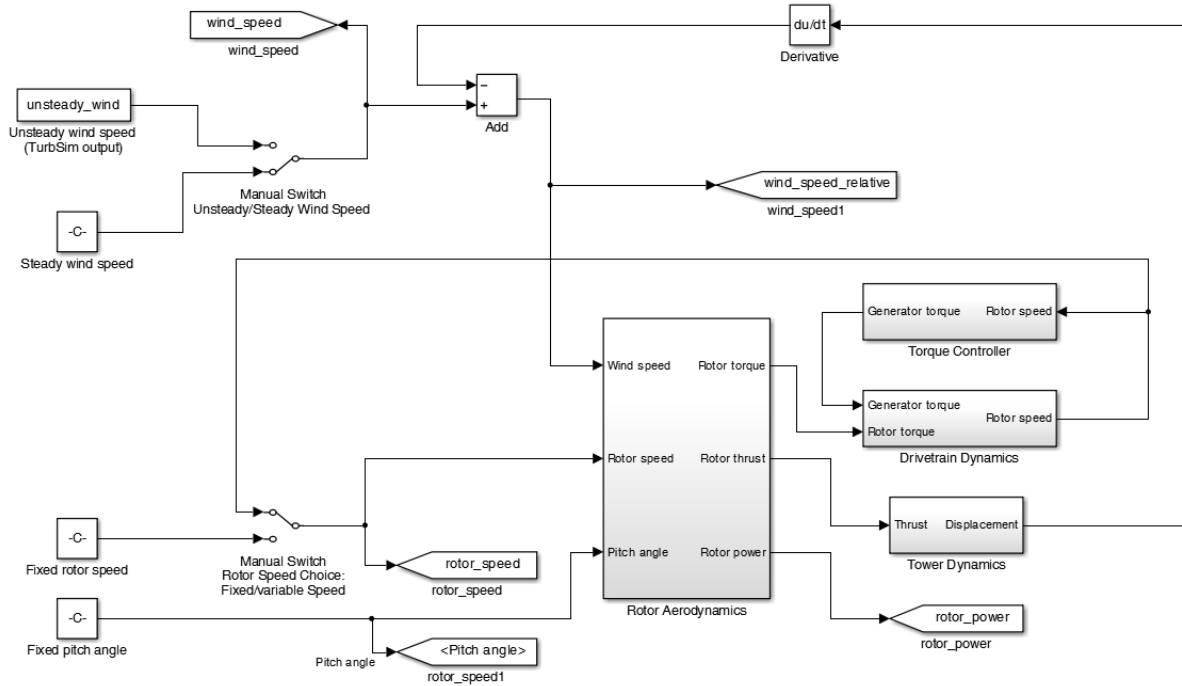


**Figure 35.** Turbine Simulink model

The rotor torque output of the aerodynamics subsystem is used as one of the two inputs to the drivetrain dynamics subsystem. The other input to this subsystem is the demanded generator torque by the controller. To analyze the test rig drivetrain dynamics, a simple one-mass (lumped) model was used as shown in Figure 37. In this one-mass model [66], [67], all components are lumped together, essentially working as a single rotating mass. The drivetrain dynamic behaviour can be formulated and rearranged based on the Newton's second law for rotation as:

$$\sum T = I_{eq} \alpha = I_{eq} \frac{d\Omega}{dt} \quad (4.1)$$

$$\frac{d\Omega}{dt} = \frac{T_a - T_g - T_f}{I_{eq}} \quad (4.2)$$

Where  $\sum T$  is the net external torque [N.m],  $\Omega$  is the angular velocity [rad/s],  $\alpha = \frac{d\Omega}{dt}$  is the angular acceleration [rad/s<sup>2</sup>],  $T_a$  is the aerodynamic torque [N.m],  $T_g$  is the generator torque [N.m],  $T_f$  is the frictional/damping torque [N.m], and  $I_{eq}$  is the equivalent rotating mass moment of inertia [kg.m<sup>2</sup>] at the low speed shaft (LSS) side, calculated considering the gear box (GB) ratio,  $k$ , as:

$$I_{eq} = I_{rotor} + \frac{(I_{generator} + I_{GB})}{k^2} \quad (4.3)$$

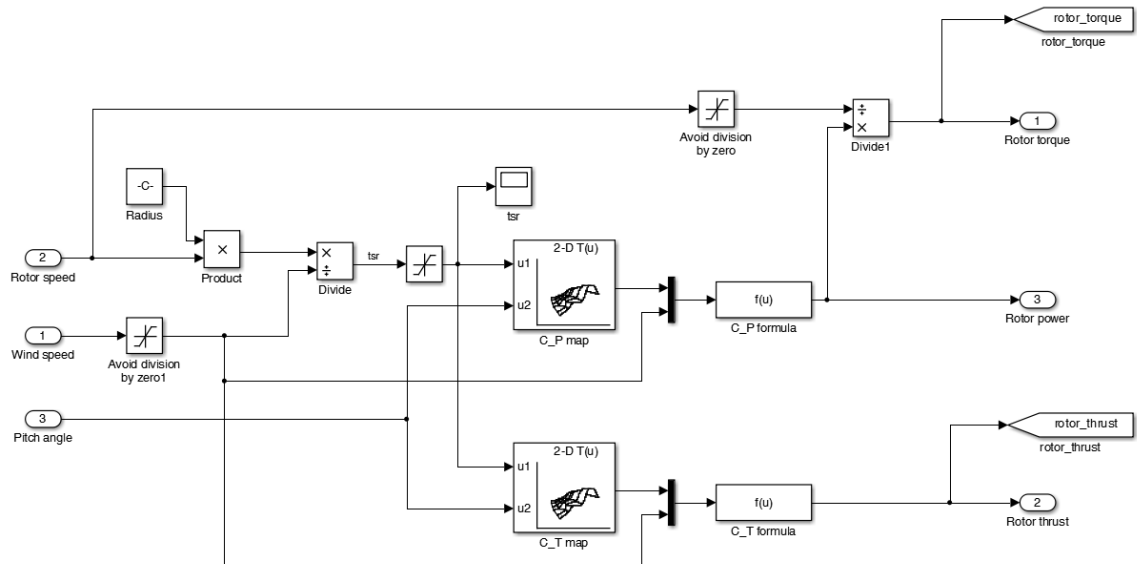


**Figure 36.** Rotor aerodynamics subsystem

To calculate the equivalent moment of inertia, moment of inertias of the actual rotor, the generator rotor, and the gear box were needed. The method by which the moment of inertia of the rotor was quantified will be discussed in the next section. The latter two inertias were obtained roughly from the manufacturer specifications. The other unknown parameter was the frictional damping constant.

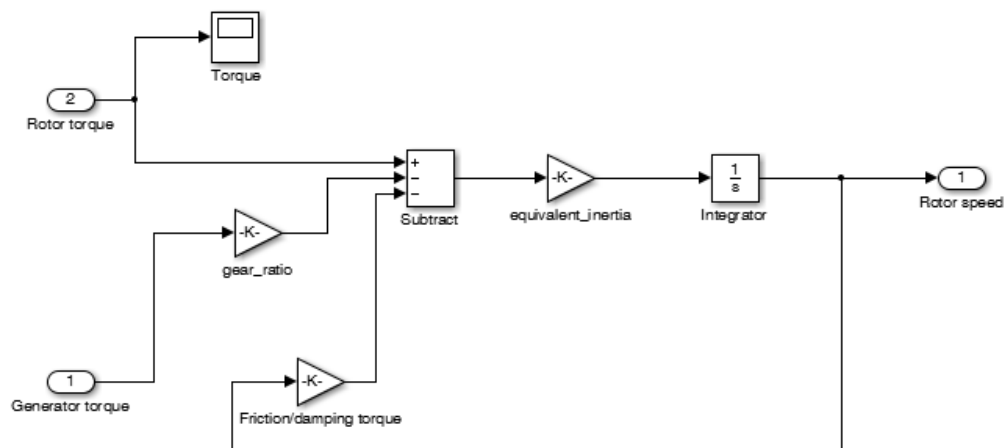


**Figure 37.** LSS One-mass (lumped) drivetrain dynamics subsystem

The design objectives of the final LabVIEW application was to utilize a proportional-integral (PI) controller to effectively control a set rotational speed using the EV controller's throttle and regeneration signals. As shown in Figure 38, to model the torque controller subsystem, a PID block was used (this controller will be discussed in 4.7).

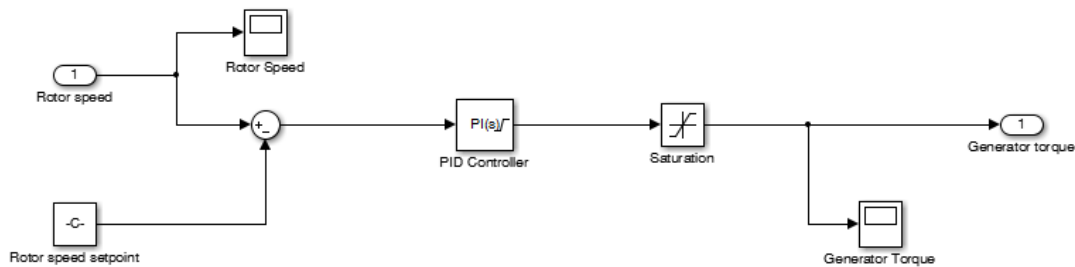


**Figure 38.** Torque controller subsystem

As illustrated in Figure 39, the thrust is used as the input for the tower dynamics subsystem, where the displacement is then calculated using the tower transfer function. Differentiating this displacement allows for relative wind speed corrections.

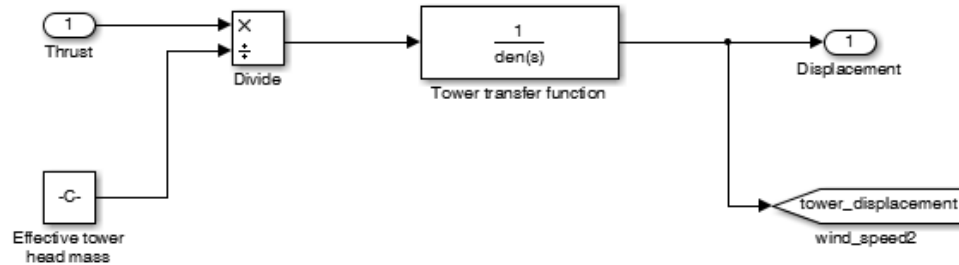


**Figure 39.** Tower dynamics subsystem

#### 4.5.2 Rotor Inertia Measurement using Bifilar Pendulum Test

Mass moment of inertia of the actual rotor was one of the unknown parameters needed for an accurate modeling of the dynamics of the drivetrain. Typically, this parameter can be obtained from the data provided by the computer aided design (CAD) model of rather simple geometries. For more complex geometries, this parameter can be measured experimentally using a simple and cost-effective bifilar (two support wire) vertical axis torsional pendulum test [68].

A bifilar torsional pendulum test rig was developed as shown in Figure 40. The rotor was suspended from two parallel vertical wires that were free to rotate about their attachment points on a custom plate machined to hold the rotor hub using the actual M10 bolt. Based on the frequency of oscillation measurements for the plate with and without the rotor mounted, an estimation of the rotor inertia was measured using [68]:

$$I_{rotor} = \frac{mgd^2}{4h\omega_n^2} \quad (4.4)$$

Where  $m$  is the mass of the test object [kg],  $g$  is gravitational acceleration [ $m/s^2$ ],  $d$  and  $h$  represent the distance between wires and their heights as shown in Figure 40 [m], and  $\omega_n$

is the angular frequency [rad/s] calculated out of the measured frequency of oscillations,  $f$  [Hz]. Frequency of oscillation was simply calculated using the time period,  $T$  [s], associated with the known number of oscillations,  $N$ , as:

$$f = \frac{N}{T} \quad (4.5)$$

Subsequently, the angular frequency was calculated using

$$\omega_n = 2\pi f \quad (4.6)$$

The geometrical and mass-related parameters as well as the bifilar test results, for both cases of the single plate and rotor mounted on the plate are summarized in Table 25.

**Table 25.** Rotor inertia bifilar pendulum test results

	Number of rotations	Time (s)	f (Hz)	$\omega_n$ (rad/s)
<b>Rotor + Plate Tests:</b>				
Test 1	11	52.11	0.21109	1.32633
Test 2	11	52.12	0.21105	1.32608
Test 3	11	52.19	0.21077	1.32430
Mean $\omega_n$ (rad/s)				1.32557
<b>Plate Tests:</b>				
Test 1	12	15.39	0.77973	4.89917
Test 2	12	15.38	0.78023	4.90236
Mean $\omega_n$ (rad/s)				4.90076
<b>Known parameters:</b>				
h (m)	0.59			
d (m)	0.162			
Rotor mass (kg)	6.9			
Plate mass (kg)	0.05			
Rotor + Plate mass (kg)	6.95			
g (m/s <sup>2</sup> )	9.81			
<b>Final results:</b>				
Rotor + plate inertia	0.43149			
Plate inertia (kg.m <sup>2</sup> )	0.00012			
Rotor inertia (kg.m <sup>2</sup> )	<b>0.43137</b>			

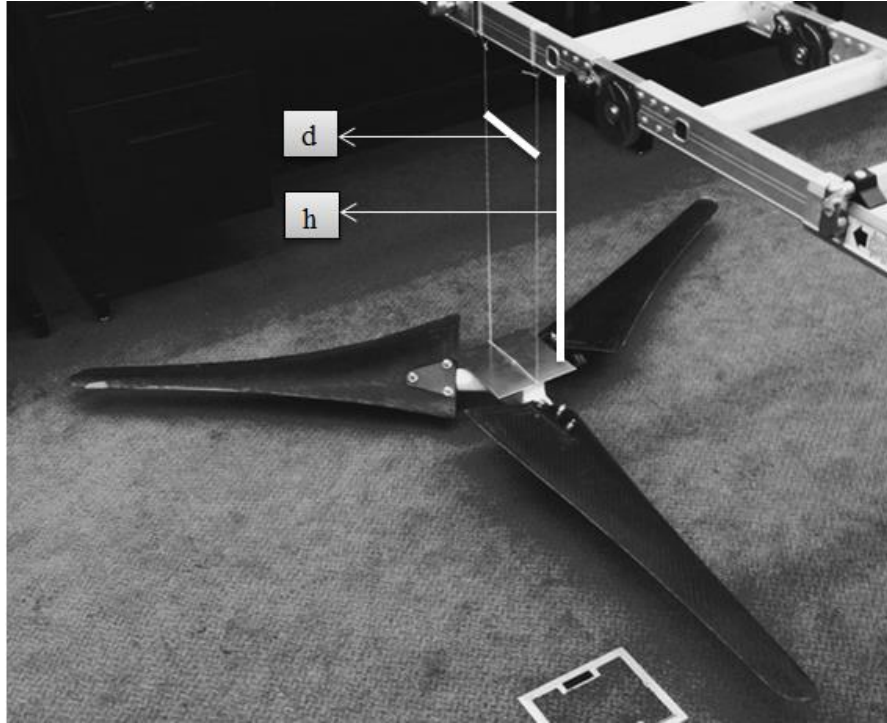


**Figure 40.** Bifilar pendulum test of the rotor

#### 4.6 System Identification

Although the bifilar pendulum test solved one of the unknown parameters for the system modeling and analysis, other parameters such as the actual equivalent drivetrain and generator inertia on the turbine side (LSS), friction or damping coefficient, and two key conversion constants were still unknown. The latter two parameters were the constants associated with the internal logics of the Gen4 EV controller. The operator (or the closed loop system) can input throttle (motor operation) and regeneration (generator operation) voltage signals which are then translated to torque demands inside the controller to be sent/extracted to/from the motor/generator based on these two parameters. Unfortunately, as the combination kit of this Gen4 EV controller and PMAC generator is typically used for electric boats or gulf karts, the supplier of the kit was unable to provide detailed information regarding how the controller was actually programmed internally. It was of

interest to know how the voltage signals are translated to torque demands on both throttle (motor) and regeneration (generator) paths. In the absence of the required tools to interface with the controller (i.e. DriveWizard configuration tool, CANOpen protocol, etc.), it was a black box in practice.

To obtain an estimate of these conversion constants as well as the overall inertia and damping constant, System Identification Toolbox within MATLAB and Simulink, explained in [69], was utilized. Basically, this method allows building mathematical models of a dynamic system based on the measured input-output data. This trial-and-error process seeks to adequately capture the dynamics of a system in three key steps described in [70] as:

- 1. Gathering experimental data:** Both time and frequency data of the system can be collected. To achieve reliable estimates, at least two data sets are needed. One for estimation and the other for validation.
- 2. Estimating the model from data:** A generic model of the system can be selected and fit to the estimation data set.
- 3. Validating the model:** The independent data set can then be used to validate the model obtained from the estimation data set.

Within the System Identification Toolbox, both a GUI (shown in and accessible using the `ident` command) and many MATLAB functions can be utilized for the identification. In this study, both the GUI and MATLAB's `idgrey` function, a linear ordinary differential equation (ODE) grey box model with identifiable parameters were used. A grey box

(parameter estimation) modeling approach was utilized, which is typically used on systems where the structure and component properties are well-known without exact knowledge of the physical properties. This method can be considered as a hybrid between black box modeling (where nothing is known about the system structure but the experimental data) and first principles modeling (where the governing equations and all the parameters are known in addition to the input-output data) [70]. Upon modeling the system using the idgrey function, the greyest function was utilized to obtain estimated values for the unknown parameters.

#### **4.6.1 Speed Ramp-up and Coast-down Data Collection for Identification**

Data collection, the first step in system identification, plays a key role in the accuracy and reliability of the estimable model parameters. A total of 16 tests, all automated in LabVIEW, were conducted to collect rotational speed, throttle voltage, and regeneration voltage data. For the throttle path identification (motor mode), the LabVIEW application was developed in six steps such that two full data sets corresponding to a throttle ramp-up run, a constant throttle, and a throttle coast-down run were captured. The block diagram representing the first two steps is illustrated in Figure 41.

For the regeneration path (generator mode), data associated with coast-down tests of a total of 14 voltage levels (0 - 2 V) were collected. As can be seen in Figure 42, the performance of the regenerative braking was verified, observing a faster coast-down with higher regeneration levels. Despite commanding a consistent throttle signal of 0.47 V in the ramp-up portion of the runs, before applying the regenerative braking levels, the starting rotational speed of the rotor did not remain the same. This could be due to the

variation in temperature impacting the frictional resistance and other unknown internal logics of the Gen4 controller.

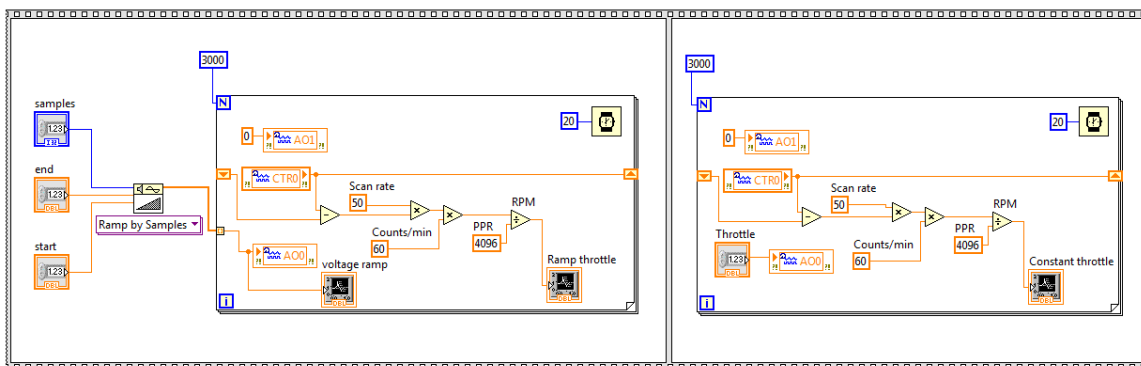


**Figure 41.** Throttle path ramp-up VI for system identification

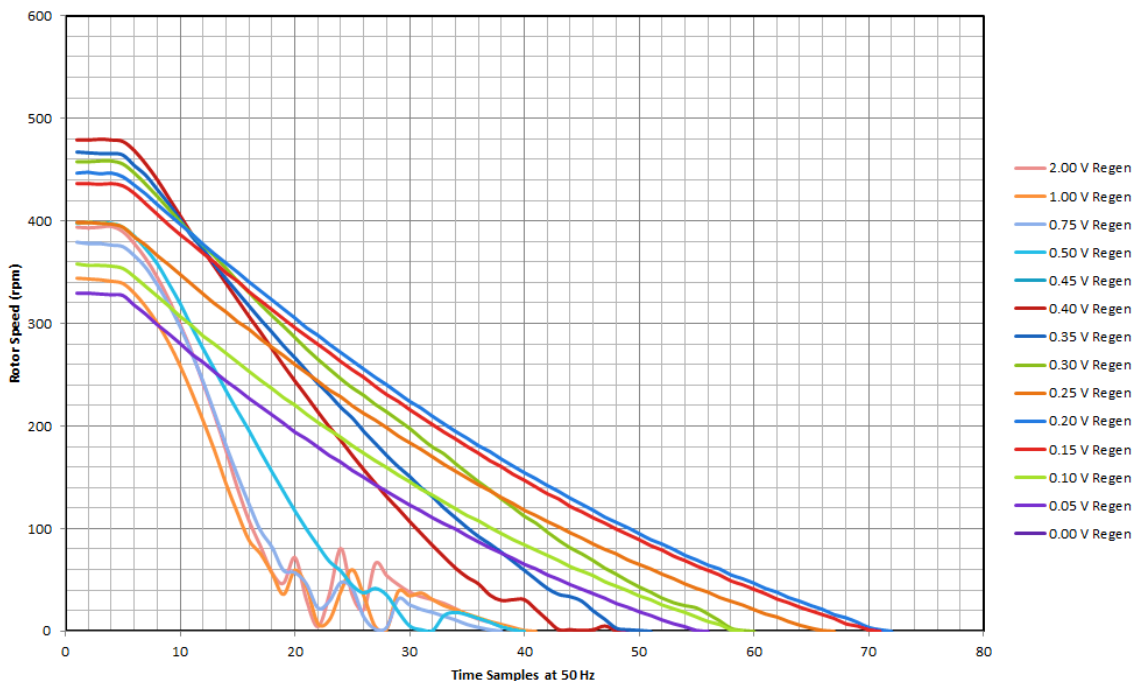


**Figure 42.** Regeneration path coast-down raw test results

For identification, the unknown physical properties to be investigated were  $S_m$  torque-voltage relationship slope for motor operation (throttle),  $S_g$  torque-voltage relationship slope for generator operation (regeneration),  $J$  total equivalent rotational inertia, and  $c$

damping/friction coefficient of the drivetrain. The equation of motion of the drivetrain in state-space representation was formulated as:

$$\begin{aligned}\dot{x} &= Ax + Bu \\ y &= Cx + Du\end{aligned}\quad (4.7)$$

Where:

$$A = \begin{bmatrix} -c & 0 \\ J & 0 \\ 1 & 0 \end{bmatrix} \quad B = \begin{bmatrix} S_m & S_g \\ J & J \\ 0 & 0 \end{bmatrix} \quad C = [0 \ 1] \quad D = [0 \ 0]$$

Overall, this grey box approach did not produce consistent and reliable results that could be used for the torque-voltage slopes (which were not included in Simulink models).

However, the estimated values for the damping coefficient and the rotational inertia were used as initial values in a new Simulink model of the system (discussed in 4.7.1). A sample comparison between the linear grey box model and the measured data of a throttle ramp-up run, which provided a 95 % fit, is illustrated in Figure 43.

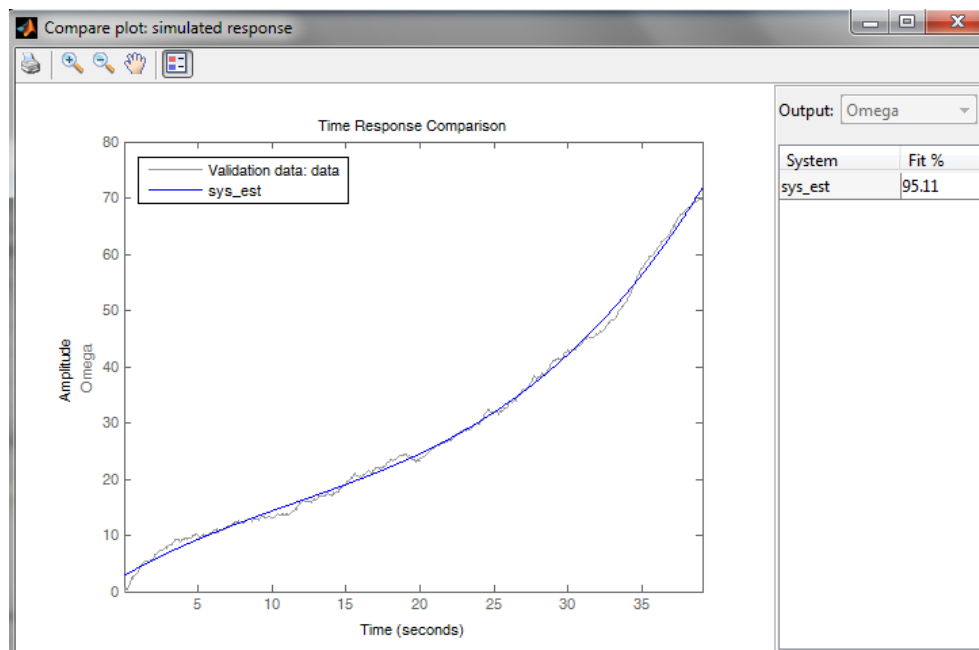


**Figure 43.** Comparison of the grey box model and the measured data

#### 4.6.2 Torque-voltage Slope Identification using a Clamp Ammeter

Given the available resources and the unknown torque-voltage slopes of the Gen4 controller operation, a Fluke 324 true RMS clamp ammeter was used to actually measure the current of the phases leaving the Gen4 controller towards the generator/motor as shown in Figure 44 . The current measurement data was then used together with the torque-current slopes provided by the generator/motor supplier (0.127 N.m/A) and the gear head ratio, to approximately quantify these slopes as presented in Table 26.

**Table 26.** AC phases current measurement data

AC Phase	Throttle (V)	Current (A)	Rotor Speed (rpm)	Torque (N.m)	Slope (N.m/V)
M1	0.40	5.99	120.00	3.80	9.58
	0.45	8.01	360.00	5.09	11.33
	0.48	9.93	630.00	6.31	13.14
M2	0.40	6.05	100.00	3.84	9.58
	0.45	8.55	350.00	5.43	11.99
	0.48	10.19	630.00	6.47	13.57
M3	0.40	6.10	100.00	3.87	9.73
	0.45	8.21	250.00	5.21	11.59
	0.48	9.29	380.00	5.90	12.32



**Figure 44.** Torque-voltage slope identification using a clamp ammeter

## **4.7 Control System Design and Analysis**

The motivation behind all the modeling and identification techniques explained previously was to obtain adequate initial guess for the gains of the actual speed control system. In this section, control system objectives will be outlined. Subsequently, upon presenting a background on PID controller application and functionality, a new Simulink model developed for the combined drivetrain and generator torque controller (without rotor) will be utilized to obtain initial gains for the turbine model discussed in 4.5.1. Finally, the final simulation results of the controller performance will be presented.

### **4.7.1 Control Objectives**

The primary objective of the closed loop controller of the test rig was to provide a custom platform for real-time variable speed control utilizing a LabVIEW-based control system paired with the Gen4 EV controller, PMAC generator/motor, and the battery bank. To acquire the very first performance curve of the test rig's turbine, the control objective was defined to design a stable and robust control system to facilitate a set rotational speed traction operation in the steady state towed scenario. General control design objectives of fast rise time, minimum overshoot, and no steady state error will be tried to achieve depending on the Gen4 capabilities.

Assuming all the parameters such as torque-voltage slopes were known, this objective could be accomplished utilizing a Proportional-integral-derivative (PID) controller used in a closed loop with the encoder speed measurement feedback. When the aerodynamic power is less than friction losses, the energy from the batteries can be fed to the turbine using the Gen4 and the PID controller, essentially working as a motor in the throttle path.

In contrast, when the net torque is positive, the regenerative braking is activated. This corresponds to the actual power producing mode where the battery bank is charged.

#### **4.7.2 Generator Torque Control using a PI Controller**

The PID controllers are commonly used in a broad range of academic and industrial applications to control equipment and processes. PID controller algorithms can be classified into ideal (as used in LabVIEW), parallel (as used in Simulink), and series. The former two algorithms, which are most commonly used based on their tuning capabilities, will be covered in this study. In a general case of having all three components of Proportional (P), Integral (I), and Derivative (D), which make up a PID controller, the parallel control action is calculated as the sum of three terms, one proportional to the control error itself, one proportional to the to the integral of the control error, and one proportional to the derivative of the control error [56]. The difference between the desired value (the set rotor speed in this study) and the actual value of the quantity to be controlled (rotor speed measured by the shaft encoder) is referred to as the control error.

The algorithm is made more responsive to rapid changes in the quantity being controlled using the proportional term while the integral term ensures that steady state error tends to zero [56]. The derivative term can contribute to the control action proportional to the rate of change of the control error [56]. In Simulink, a PID block (depicted in Figure 45) can be used to model and tune a PID controller. As can be seen, a low-pass filter is commonly used to avoid amplifying high frequency noise. For the application under study, a PI controller was selected to be used (zero derivative gain). A common workflow [70] used for modeling and tuning the PI controller in Simulink was to create the plant model (as discussed in 4.5.1 and 4.7.3), model feedback loop using the PID controller

block, iteratively tune the gains, and add realistic features such as output saturation as well as anti-windup characteristics which are built in capabilities of the PID block.

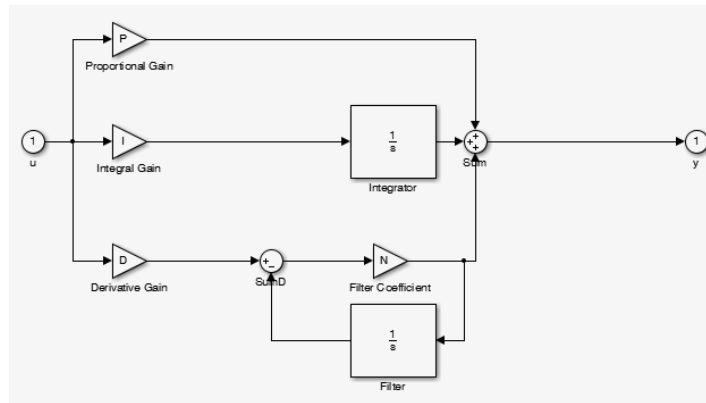


**Figure 45.** Simulink PID block

#### 4.7.3 Combined Drivetrain and Torque Controller Simulink Model

The rotational inertia and damping coefficient obtained from the system identification technique were input into a new Simulink model of the combined drivetrain and torque controller as shown in Figure 46. The intention here was to obtain proper PI gains to be used in the full turbine model for validation of the controller performance under a range of conditions including the case of unsteady wind inflow.

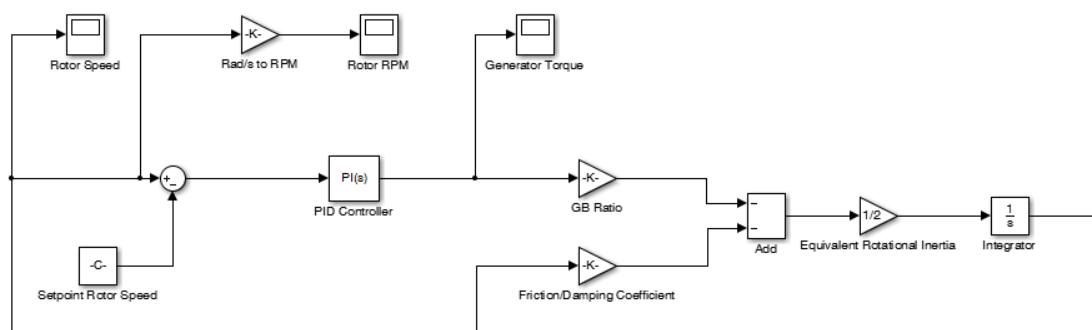
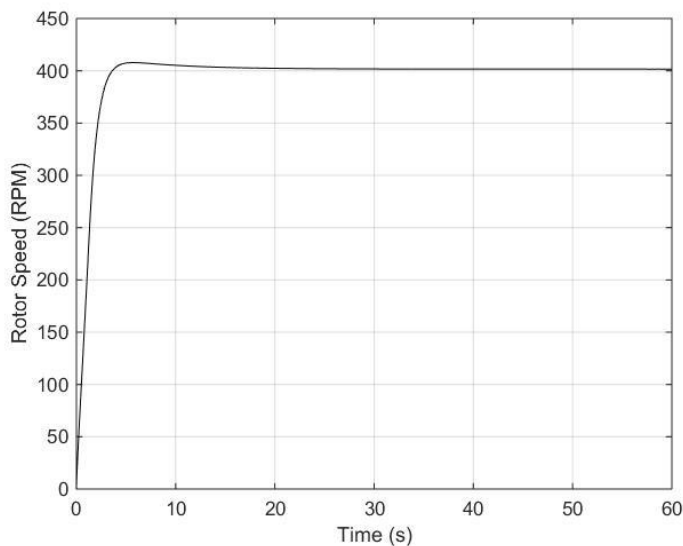


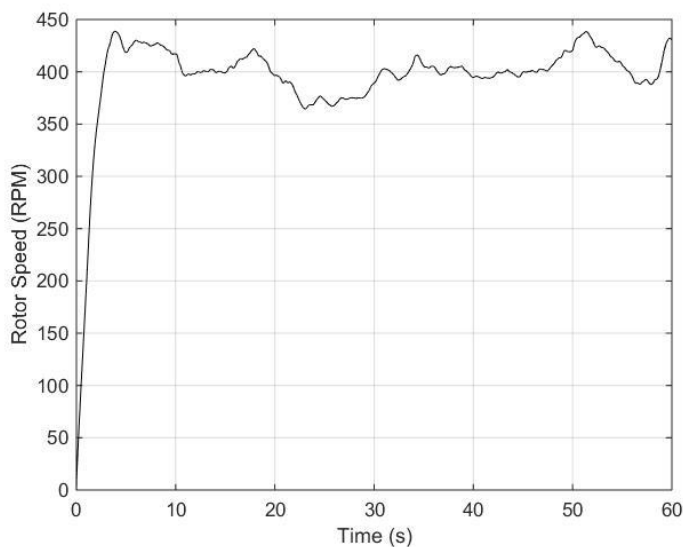
**Figure 46.** Drivetrain and torque controller Simulink model

Upon observing a rather satisfactory result from this model, the PI gains obtained from this analysis and the damping coefficient and rotational inertia attained from the system

identification were input into the main turbine model to finalize the analysis. As can be seen in Figure 47, when demanding for the rated rotor speed of 402 rpm as the set point of the closed loop, the tuned PI controller performed satisfactorily, both in the steady wind inflow (8 m/s) as well as the TurbSim-generated unsteady wind inflow, with a hub height reference speed of 8 m/s. These wind inflow profiles are illustrated in Figure 48.

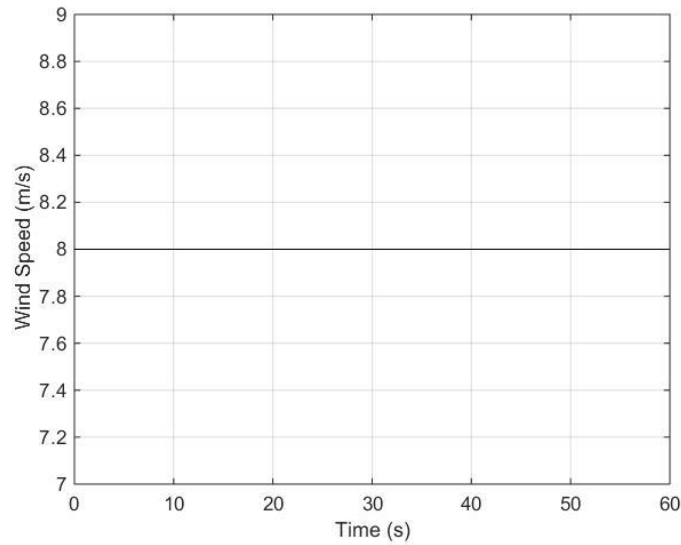


(a): Performance in steady wind inflow

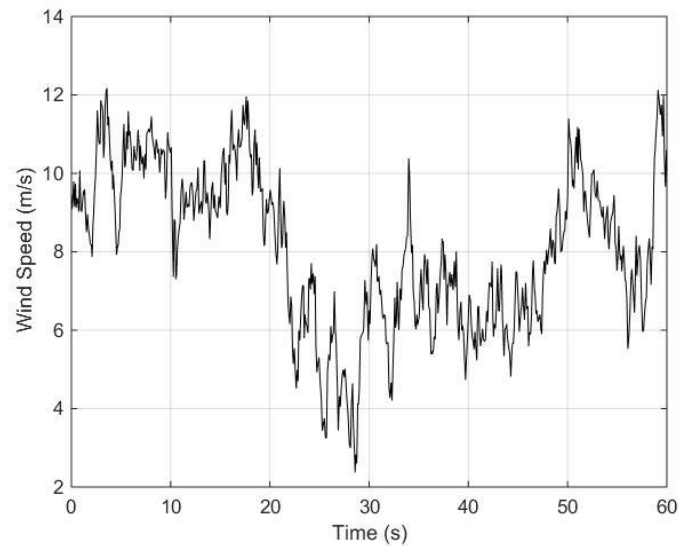


(b): Performance in unsteady wind inflow

**Figure 47.** PI controller performance in steady and unsteady wind inflows



(a): Steady wind inflow



(b): Unsteady wind inflow

**Figure 48.** Steady and unsteady wind inflows

#### 4.8 Control System Implementation in LabVIEW

Prior to implementing the actual controller in real-time, some important factors need to be considered. First of all, the PI controller performance is limited by maximum capability of the Gen4 controller in torque actuations in both throttle (motor) and

regeneration (generator) paths. For instance, when wind inflow is well below rated, the speed at which the PI controller can reach the set rotor speed in a motoring mode is primarily limited by the maximum transferrable torque supplied by the Gen4 controller. According to the supplier, the throttle voltage signal ranges from 0 V to 12 V. However, initial ramp-up/coast-down runs on the test rig revealed that the practical range is between 0.3 V to 0.7 V, where the maximum HSS of around 700 rpm can be reached when rotor is removed from the turbine. Above this voltage supply, speed remained constant. For the regenerative braking this range turned out to be between 0 V to 4 V. Secondly, other physical factors could also impact the controller's performance in practice such as the variation in drivetrain's frictional damping as a result of temperature change due to both internal heating and ambient atmospheric variations.

The third point to consider is the fact that the Simulink controller design and analysis conducted were in continuous time domain (s-domain) as opposed to the actual digital embedded controller operating in discrete steps (z-domain). Due to time constraints and given the inherent complexity of the actual system, this discretizing of the controller step was substituted with the on-line tuning of the LabVIEW-based PI controller where the discretized nature of the system and its other realistic characteristics can be dealt with practically.

The fourth point to take into account is the uncertainty in understanding the actual torque-voltage slopes implemented by the internal logics of the Gen4 controller in both motoring and power generating paths. Although the current measurements gave rough estimates regarding these slopes, a practical solution was needed to ensure safe and reliable operation. As a simple, yet creative solution, it was decided to add these two slopes as

additional gains to the already existing P and I gains. Consequently, a total of four gains were required to be tuned in real time.

Following the same principle discussed in 4.7.2, the PID algorithm in LabVIEW [71] compares the setpoint (SP) to the process variable (PV) to obtain the control error.

$$e = SP - PV \quad (4.8)$$

Subsequently, the ideal control action is calculated as

$$u(t) = K_c \left( e + \frac{1}{T_i} \int_0^t e dt + T_d \frac{de}{dt} \right) \quad (4.9)$$

Where  $K_c$  is the controller gain,  $T_i$  is the integral time in minutes (reset time), and  $T_d$  is the derivative time in minutes (rate time) [71]. The built-in LabVIEW PID VI (code/block), which uses an integral sum correction algorithm to facilitate anti-windup, can limit the output range using:

$$\begin{aligned} \text{If } u(k) \geq u_{max} \text{ then } u(k) &= u_{max} \\ \text{If } u(k) \leq u_{min} \text{ then } u(k) &= u_{min} \end{aligned} \quad (4.10)$$

The PID parameters are defined differently in Simulink and LabVIEW. Summarized in Table 27, the parameters conversions from one platform to the other are derived, simply by comparing the control action formulations considering  $T_s$  as the sampling frequency.

**Table 27.** Comparison of PID gains in LabVIEW and Simulink

Gain	LabVIEW (Ideal Format)	Simulink (Parallel Format)
Proportional (P)	$K_c = K_p$	$K_p$
Integral (I)	$T_i = \frac{K_c T_s}{60K_i}$	$K_i$
Derivative (D)	$T_d = \frac{K_d T_s}{60K_c}$	$K_d$

The final PI closed loop control system developed and implemented using a PID controller VI in LabVIEW is illustrated in Figure 49. The PI controller operates within a deterministic Timed-loop structure synchronized to the scan engine of the CRIO controller. A case structure was utilized to couple the PI controller control action with the voltage signals sent to the Gen4 controller by the CRIO module. The torque demand and supply between the turbine and the battery bank is then managed by the Gen4 controller.

As a result, if the difference between the set point (i.e. the desired rotor speed) and the feedback process variable (i.e. the rotor speed measured by the encoder, CTR0) is positive, the throttle action (AO0) will be used, else the regen braking (AO1) will be activated. It should be noted that on the regeneration mode logics, since the corresponding error is negative, the regenerative action should be multiplied by a negative sign.

Here it was assumed that the Gen4 controller actuates a single mode (i.e. motor or generator) at a time. Hence, when the error is positive (below rated operation) the throttle signal is solely activated, essential prescribing a zero command to the regeneration signal and vice versa on the reversed path.

The PID VI has multiple inputs that can be customized depending on the application requirements. In this application, the setpoint rotor speed, PID gains, and output range were made accessible to the operator. The output range can be specified in terms of percentage of full scale from -100 to 100 (default) or it can be set to relates to actual engineering units. Two additional inputs can also be added to the application, namely dt and reinitialize. Detailed information about all these features is available in [71].

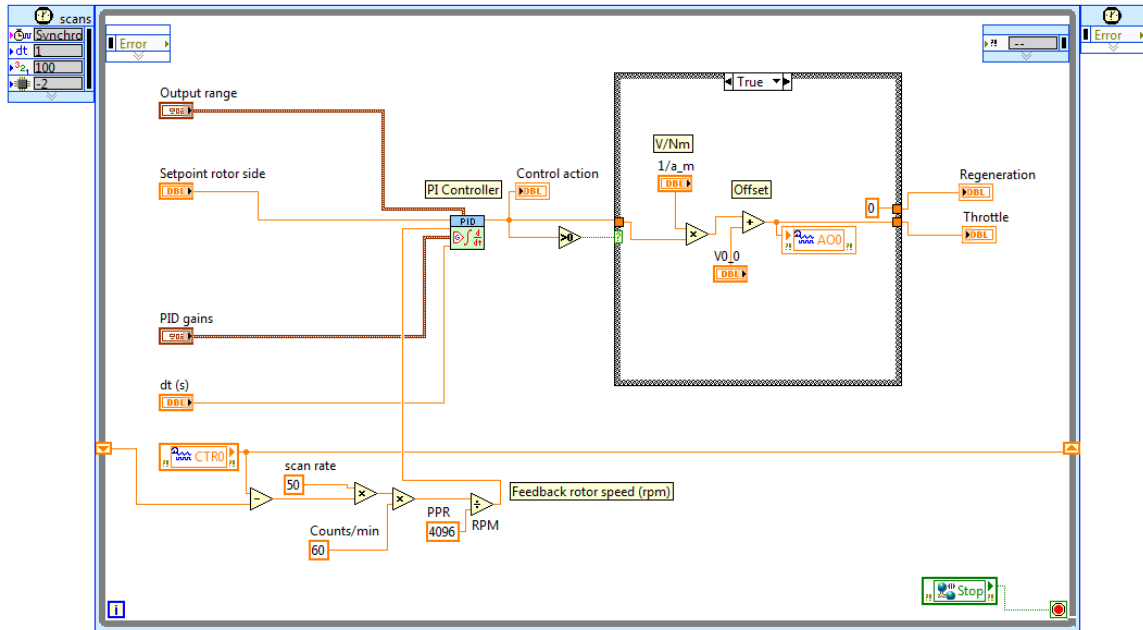


**Figure 49.** Closed-loop control system block diagram in LabVIEW

#### 4.9 LabVIEW-based Controller Tuning in Real-Time

Tuning is the process by which optimal PID gains for a control system are determined to enhance the system to provide control actions adequately based on specific design requirements of an application [72]. Within both Simulink and LabVIEW automatic tuning tools are available to the users. However, these tools do not always provide the optimal gains for a practical control system. There are a broad range of tuning methods used based on the specifics of an individual application. For this study, the controller models were initially tuned manually, using a trial and error method, which is similar to Ziegler Nichols method [72].

A key to effectively tune PID gains based on the trial and error method is to comprehensively understand the actual impacts of each individual gain on the system response. In general, the system response is analyzed based on properties such as rise time, overshoot, settling time, and steady state error. Considering the case of demanding

a setpoint rotor speed, rise time is the time needed for the rotor to go from 10 % to 90 % of the demanded speed. Overshoot is the amount that the actual rotor speed exceeds the demanded setpoint, often reported as percent of the setpoint. Settling time is the time that needs to be elapsed before the rotor speed settles within a certain percent of the demanded speed (typically 5 %). Steady state (SS) error is the final difference between the setpoint and the measured speed. The impacts of each of the PID gains on a response of a closed-loop system are summarized in Table 28 [73].

**Table 28.** PID effects on a closed-loop system response [73]

Gain	Rise Time	Overshoot	Settling Time	SS Error
$K_p$	Decrease	Increase	Small Change	Decrease
$K_i$	Decrease	Increase	Increase	Eliminate
$K_d$	Small Change	Decrease	Decrease	No Change

During the trial and error tuning of the PI controller selected for the application under study, the integral gain was initially set to zero. Subsequently the proportional gain was increased until an oscillation in response was observed. The integral term was then tweaked to damp the oscillation and eventually minimize the steady state error.

Derivative term was not added to the system to minimize the system sensitivity to noise while maintaining practical simplicity. In practice, engineers are required to often trade off one characteristic of a control system for another to adequately meet the design requirements [70].

As mentioned earlier, the closed-loop control system designed for the test rig was different from a typical PI-based system in that it had two additional torque-voltage slope gains which were needed to be tuned. Slope estimates from the current measurements

were used as initial guess for the latter two gains while the identification and Simulink modeling tuned gains were used as initial guess for the P and I gains of the actual system.

Finally, initial guesses for the proportional gain  $K_c$ , integral time  $T_i$ , torque-voltage slope in motor operation  $a_m$ , and torque-voltage slope in generator operation  $a_g$  were input into the actual LabVIEW GUI in real time. For the latter two gains, a reciprocal of the slopes were used since voltage signals were to be demanded from the Gen4 controller by the PI-based control system. A trial and error method was utilized to tune the controller with optimal gains for the control system capable of tracking the demanded speed as outlined in the design objectives.

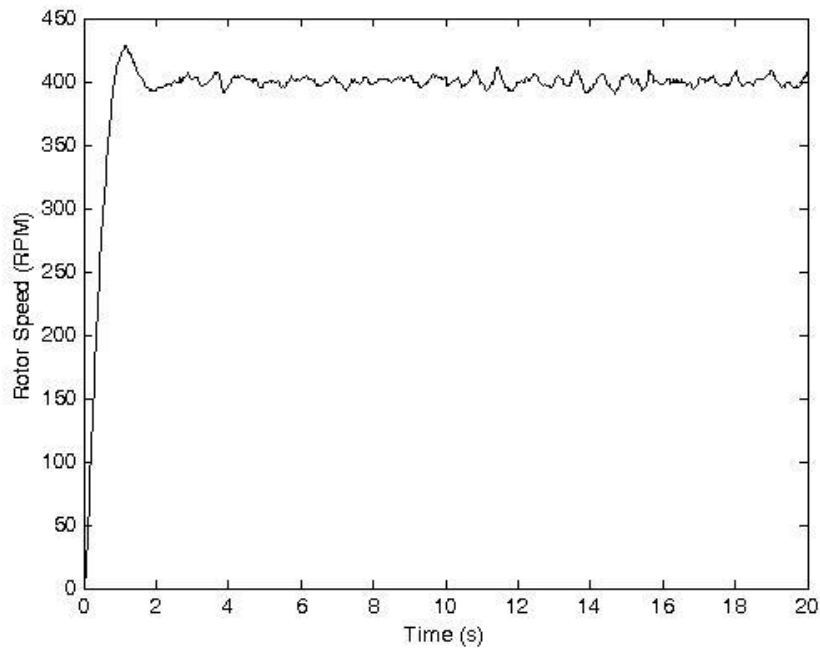


**Figure 50.** Control system performance at rated rotor speed

Control system performance at rated rotor speed of 400 RPM is illustrated in Figure 50.

As can be seen, given the inherent physical constraints, the controller performance was

satisfactory with approximately a one-second rise time, an 8 % overshoot, and a two-second settling time.

The control system was also successfully communicated with the Gen4 controller, through the CRIO, to provide the turbine with adequate generator torque actuations to track the demanded rotor speed. This performance from an actual test run (which will be explained in Chapter 6) is depicted in Figure 51. As illustrated, when the net torque was negative, full throttle was applied by the closed-loop control system. Subsequently a zero throttle was maintained throughout the power generating period using the regenerative braking system.

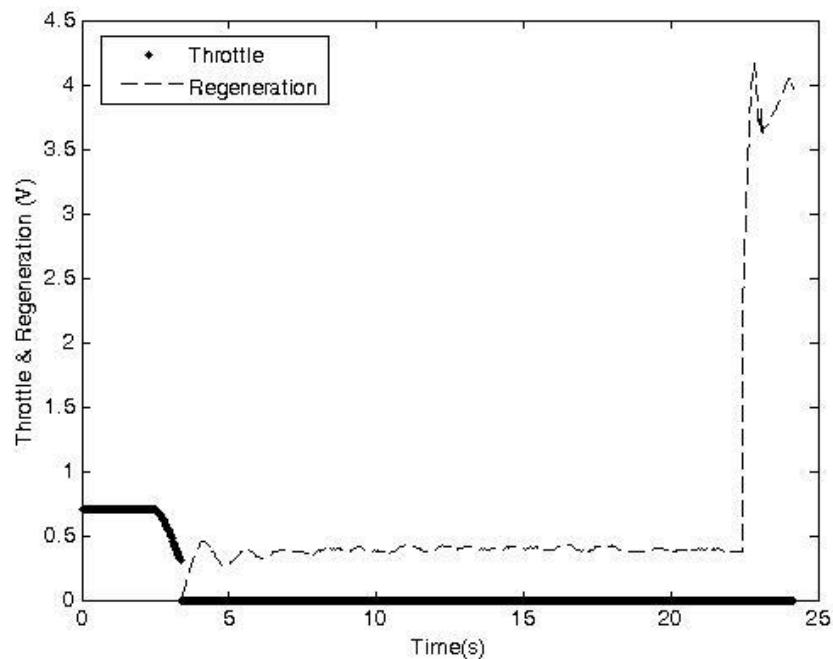


**Figure 51.** Regenerative braking and throttle torque actuation during towed test run

## **Chapter 5: 3D CFD Simulation of the Testing Platform in ANSYS**

The wake region, the region of disturbed turbulent flow downstream of the car moving through the air, is massively separated. In order to have a better understanding of the flow field behind the vehicle selected to be used to tow the test rig, the flow over a 3D model of the vehicle was simulated.

### **5.1 CFD Simulation Objectives**

Key objectives of this CFD study were to determine whether or not the flow properties at the turbine rotor location are affected by the wake generated at the rear of the tow vehicle, as well as to investigate how the variation of velocity profile could impact data collection on the circular region of the rotor and adjacent transducers.

### **5.2 Background**

Ground vehicles can be categorized as bluff-bodies that are fully submerged in the fluid. Based on the high Reynolds number, the flow regimes are fully turbulent and complicated interactions between flow separations and the dynamic behavior of the released vortex wake determine the aerodynamic forces on these vehicles [74].

The effects of Free Stream Turbulence (FST) on the flow around bluff bodies were reviewed in [75]. Mechanisms by which FST can affect the mean flow around a body were identified to be: accelerated transition to turbulence in shear layers, enhanced mixing and entrainment, and distortion of FST itself by the mean flow [75]. It is apparent that for ground vehicles, turbulence could influence separation, reattachment, and the pressure in the region that is affected by separation [76].

In general, turbulent flow simulation methods can be categorized as Direct Numerical Simulation (DNS), Scale Resolving Simulations (SRS), and Reynolds Averaged Navier-Stokes simulations (RANS). The SRS includes Large Eddy Simulation (LES) in which the motion of the largest eddies is directly resolved in the calculation, in at least a portion of the domain, but eddies smaller than the mesh are modeled [77].

Several experiments and numerical simulations have been conducted based on a very simplified parametric bluff-body called Ahmed vehicle model which has been used frequently as a benchmark in vehicle aerodynamics [74], [78]. The geometry of this model illustrated in Figure 52, was designed to be such that experiments can be conducted with reference to the flow around the slanted rear end [74].

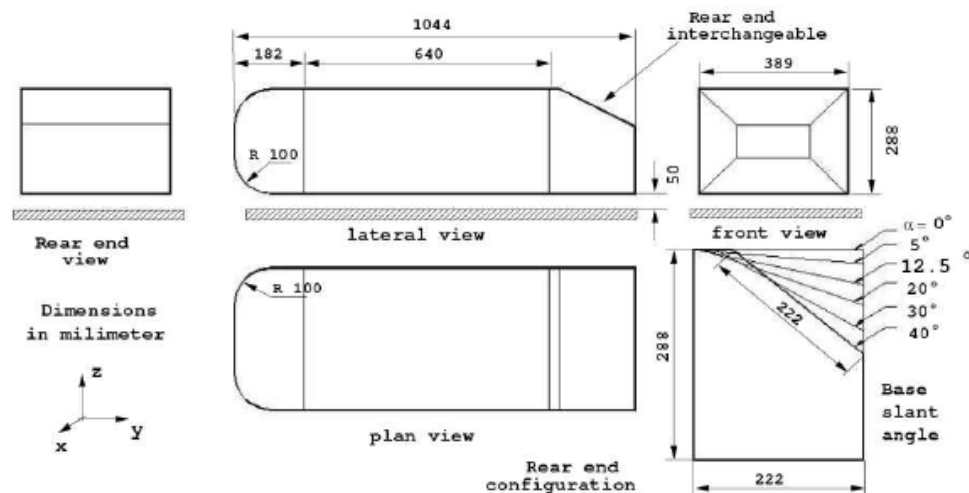


**Figure 52.** Ahmed vehicle model [74]

Using this model, most of the characteristics of the flow around this bluff body in ground proximity such as formation of trailing vortices, re-circulatory flows, and massive separation were predicted throughout various scenarios [74].

Most vehicles generate lift, but pertinent trailing vortices influenced by the large separated region at the rear of the vehicle are unsteady and rapidly dissipate. It was argued that for computing vehicles flows, LES methods are more suitable compared to RANS equations coupled with a turbulence model [74], [76].

To sum up, the interaction between a turbulent approaching flow and a road vehicle is complicated and studying the effects of various aspects and elements is not in the scope of this chapter. However, it is apparent that turbulence leads to uncertainties when actual road vehicle flow properties measurements are compared to experimental results and numerical simulations [76].

### **5.3 Theoretical Model**

Airflow over the tow vehicle is governed by the Navier-Stokes equations. Based on the velocity, length of the model, and viscosity, the Reynolds number for this problem was calculated to be  $5.14 \times 10^6$ . The flow of air was expected to be turbulent and approximately isothermal at 288K and was assumed to be steady. Due to the complexity of the LES approach and given the time constraints of the project, RANS turbulence modeling approach was utilized for this study, presenting an indicative result in the flow region above the separation region where the rotor will be. RANS equations were to be solved for this problem. Among the broad range of turbulence models, the Shear Stress Transport (SST) turbulence model was selected. The main motivation for choosing the SST model in aerodynamics is that it is one of the most accurate two-equation models for separation prediction. Standard two-equation models miss the separation and predict attached flow even for strong pressure gradient flows [77]. Introduced in [79], SST

exploits both two-equation models of k-epsilon and k-omega by blending the free stream advantages of the k-epsilon model with the wall bounded advantages of the k-omega model. Full presentation of the RANS and Navier-Stokes equations was skipped as it was out of the scope of this chapter. More details about the modified SST model formulation developed by ANSYS\_CFX software development department can be found in [80].

#### 5.4 Computational Domain and Geometry

A simple 3D model of a Chevrolet Astro van was designed in CATIA as shown in Figure 53. The model was then imported into ICEM CFD, a meshing program within the ANSYS platform. The model had a length of  $L = 5050 \text{ mm}$ , a height of  $H = 2325 \text{ mm}$ , and a width of  $W = 1800 \text{ mm}$ . The inlet flow section was placed  $3L$  upstream of the model front, while the outlet flow section was placed  $10L$  downstream of the model rear end. The computational domain, depicted in Figure 54, was defined as:

$$14L \times 4H \times 3.5W$$

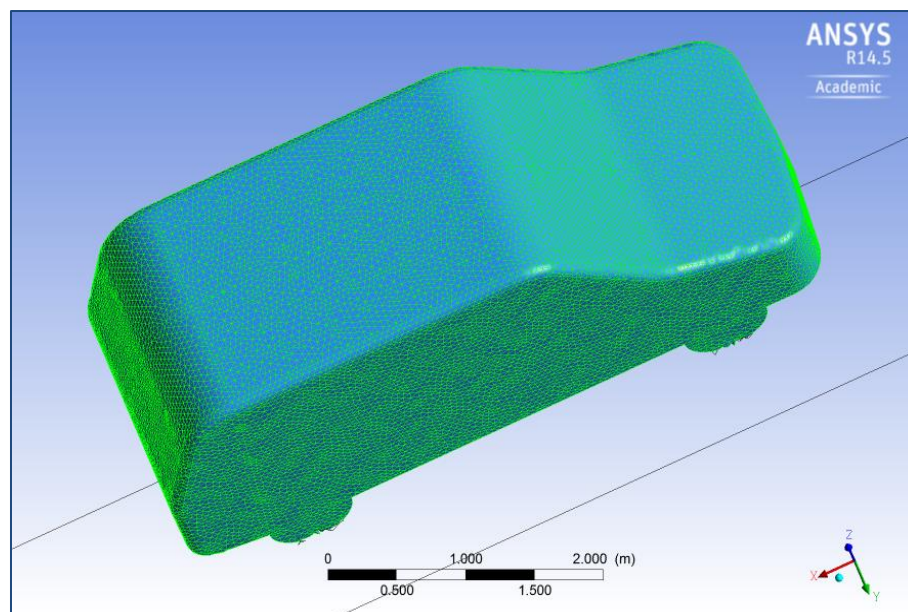


**Figure 53.** Simple tow vehicle model

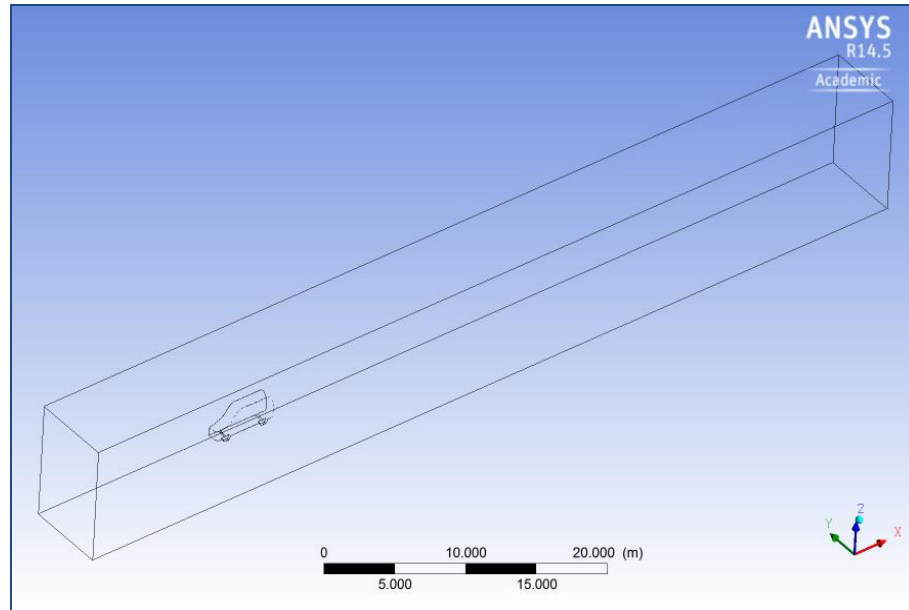


**Figure 54.** Computational domain

### 5.5 Boundary Condition and Grid Layout

A Newtonian viscous fluid model was adopted, with a flow speed of  $U_{\infty} = 15 \text{ m/s}$  and a kinematic viscosity of  $\nu = 14.75 \times 10^{-6} \text{ m}^2/\text{s}$  (air at 288K). The Reynolds number (based on the model length) was  $Re = 5.14 \times 10^6$ . At the inflow section, a uniform axial velocity profile  $U_{\infty}$  was imposed, while a free slip wall boundary condition at the ground was prescribed. The boundary condition for the car itself was selected to be no slip wall. Moreover, the symmetry boundary condition was considered based on the symmetry of the car and by neglecting the side wind flows while an opening boundary condition, used in the cases of simultaneous inflow and outflow at a single location, was selected for the top and side section of the domain. Finally, a static pressure of 0 Pa was considered for the outlet section of the domain. The grid layout is illustrated in Figure 55.

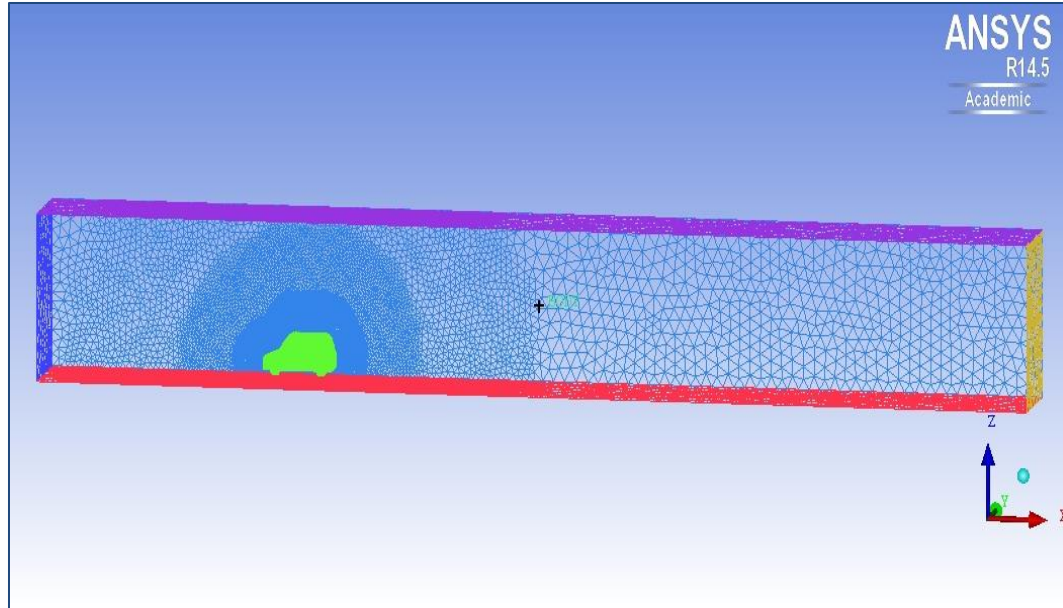


**Figure 55.** Boundary condition and grid layout

The meshing process was performed with the ANSYS ICEM CFD. It involved using an unstructured mesh utilizing tetrahedral generation, using the Octree mesh method, and addition of 18 inflation layers of prismatic elements. The imposed grid is illustrated in Figure 56. In order to have faster computation, Octree algorithm ensures refinement of the mesh where necessary while maintaining larger elements where possible. When the “root” tetrahedron, which encloses the whole geometry, has been initialized, Tetra subdivides the root tetrahedron until the point that all element size requirements are met [81]. At this stage, the Tetra mesher balances the mesh in a way that elements sharing an edge or face do not vary in size by more than a factor of two. At the next step, Tetra makes the mesh conformal, which guarantees that each pair of adjacent elements will share an entire face. As the mesh does not yet match the given geometry, the mesher next rounds the nodes of the mesh to the prescribed points, prescribed curves or model surfaces [81]. Next, Tetra "cuts away" all of the mesh, which cannot be reached by a user-defined material point without intersection of a surface. At the final stage, the mesh is

smoothed by moving nodes, merging nodes, swapping edges and in some cases, deleting bad elements [81].

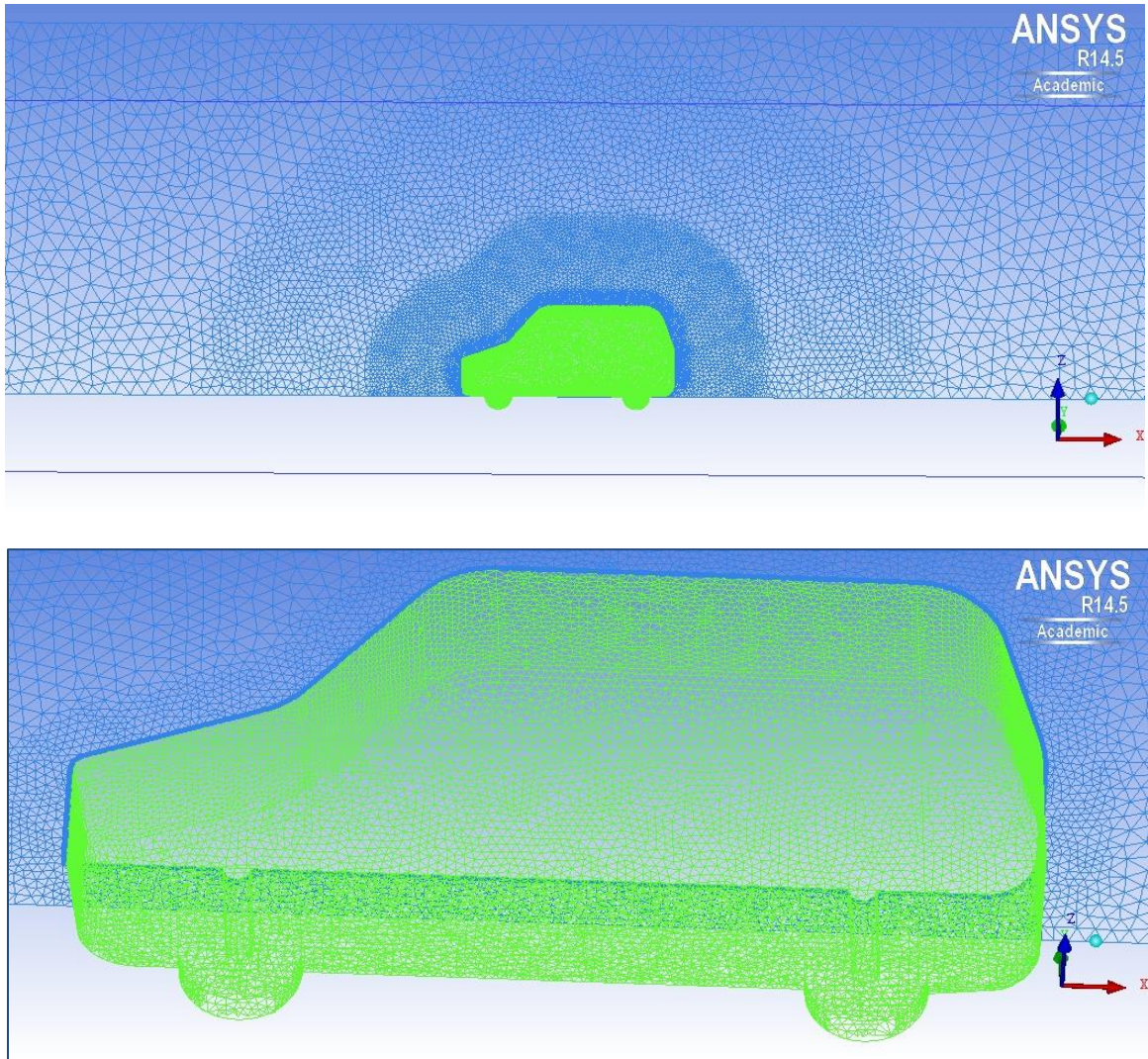


**Figure 56.** Unstructured Octree mesh

The more accurate the mesh and boundary conditions, the more accurate the converged solution will be. In this study, for the case of a steady state simulation, the solution satisfied conditions of an acceptable residual RMS error value and a steady state solution for the values of our monitor points. The convergence criteria type was selected to be residual RMS with the target of  $10^{-6}$ . The convergence control was set to 2000 for

maximum iterations, a high resolution advection scheme was chosen, and a conservative auto fluid timescale control was selected. It should be mentioned that although the monitor points reached a steady state, there was a small and steady fluctuation in the residual RMS.

## 5.6 Results and Discussions

As can be seen from Figure 57, the negative velocity region on the rear of the car, illustrated in blue color, depicts the extent of the wake. It is obvious that fortunately, the axis of rotation of the wind turbine would not be affected by the extent of the wake directly. However, once the actual mast, wind turbine, and the trailer itself are considered in the simulation, the result and pertinent flow pattern may alter.

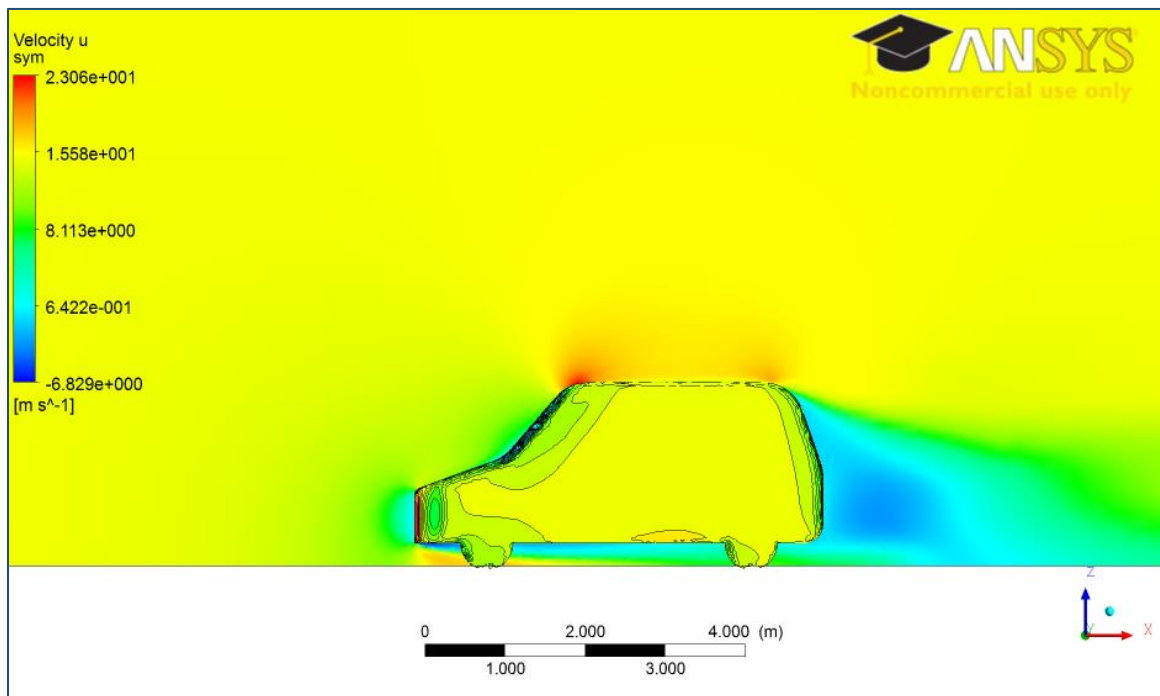


**Figure 57.** Velocity contour

Another observation that can be discussed regarding the tow vehicle contour of velocity is the existence of some high velocity regions, colored in red ink in Figure 57. Pressure

contour was also obtained as depicted in Figure 58. These results can be used to obtain a general view of the flow pattern behind the van that will be used to tow the trailer in terms of pressure and velocity. However, a wiser practice would be to gain a more specific understanding of the velocity profile in the regions that are of high interest for experimental work (e.g. turbine rotor disc area).

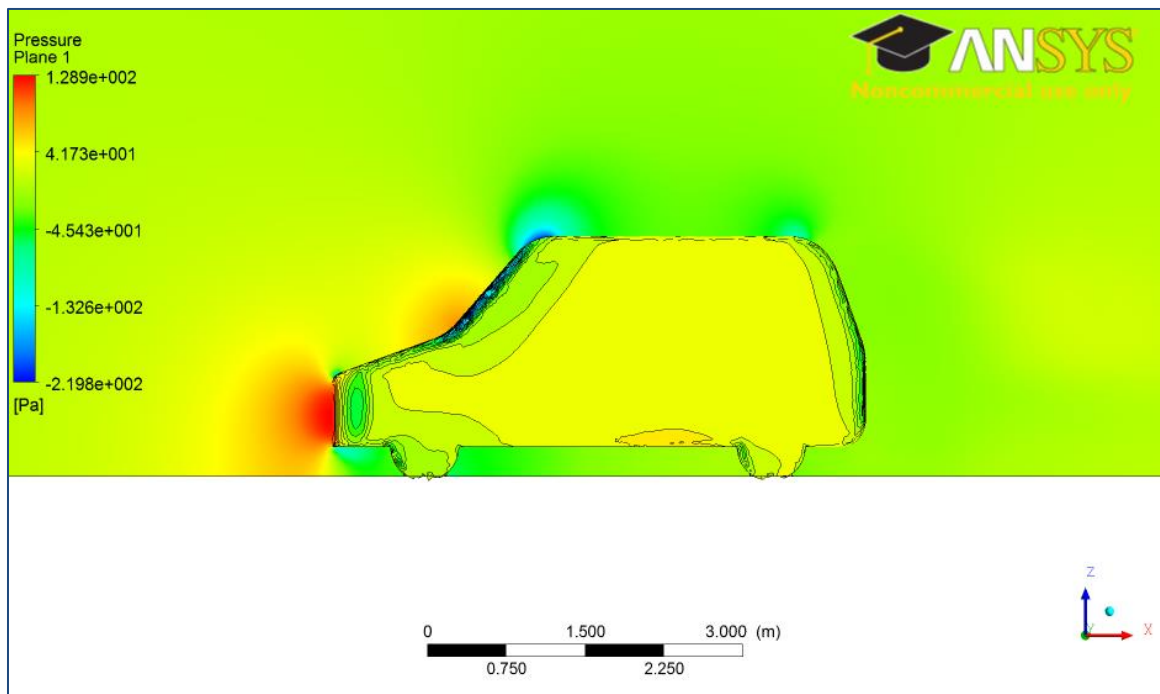


**Figure 58.** Pressure contour

In order to achieve the above-mentioned goal, the actual location of the rotor was determined based on the actual physics of the test rig. The tower of the wind turbine will be located 1.8 m at the rear of the tow vehicle (in x direction) and the radius of blades is 87.5 cm (in y direction). Moreover, the erectable telescoping tower height can be varied between 4.98 and 9.55m (in z direction).

A new parameter was defined to analyze the inflow more effectively. This parameter was  $U_{RATIO}$ , the ratio of the local velocity with respect to the inlet velocity. Considering the

circular area defined earlier, the relative velocity profile was obtained. Ideally, this ratio should be close to unity to ensure uninfluenced wind inflow feeding the turbine rotor. The location of the actual axis of rotation and velocity ratio contour at that location are depicted in Figure 59.

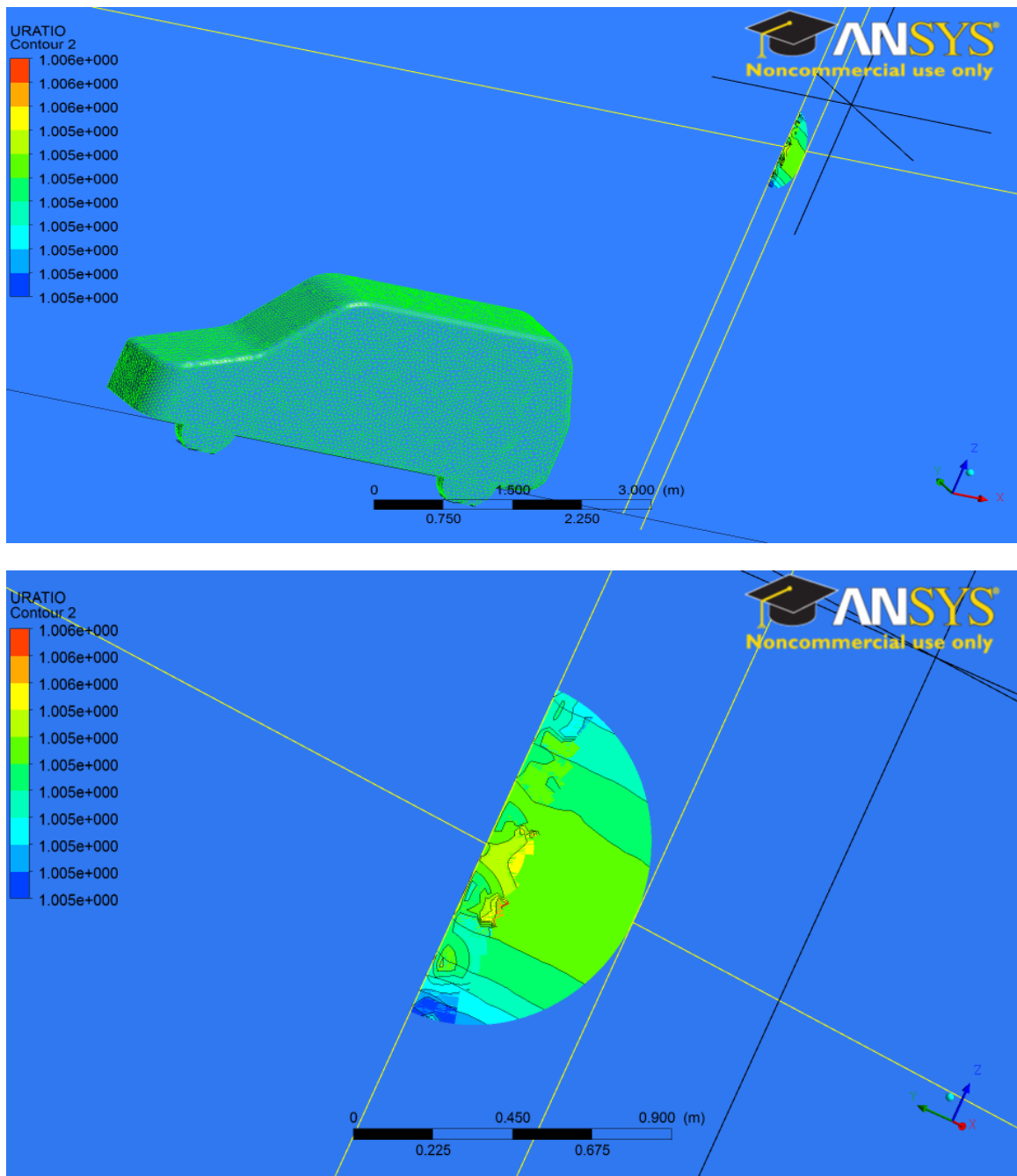


**Figure 59.** Wind velocity ratio profile at the turbine rotor

As can be seen in Figure 59, the velocity that the rotor blades will be confronting is uninfluenced by the wake generated at the rear of the tow vehicle. Based on these findings, the velocity would increase only 0.005 % as it reaches the axis of rotation. Moreover, the blades are receiving the velocity with a tiny variation throughout the circular region. An interesting point is the non-uniform pattern on the left hand side of the profile and near the center where the velocity ratio variation was up to 0.006 %. The reason behind this non-uniform pattern could be using the assumed symmetry boundary condition.

In summary, the effects of a 3D steady state flow of air around a van that will be used to tow the wind turbine rig were investigated. Among various turbulence modeling methods, SST was selected based on its accuracy for separation prediction. The velocity and pressure contour plots were obtained to determine the extent of the wake. A dimensionless velocity profile was defined. It was concluded that the axis of rotation will be located out of the region affected by the wake and disturbances. The obtained velocity profile at the rotor position showed only a 0.005 % to 0.006 % increase in the inlet velocity as the flow reaches the rotor.

## Chapter 6: Controlled Velocity Track Tests

As explained in previous chapters, the instrumentation of the test rig was completed and a LabVIEW-based closed-loop control system was implemented to provide a platform for real-time speed control. This chapter will present the experimental results of the very first set of controlled-velocity experiments successfully conducted using the test rig.

### 6.1 Test Site and Weather Conditions

Track tests were conducted on November 10, 2014 on Martindale Road, a paved road located in Saanichton, 17 km north of Victoria, British Columbia, Canada. This location, illustrated in Figure 60, was selected primarily due to the characteristics required to conduct a close-to-ideal steady state experiment. Flat open fields on either side of the road were free of big trees and buildings (power line poles were the only objects on one side of the road).

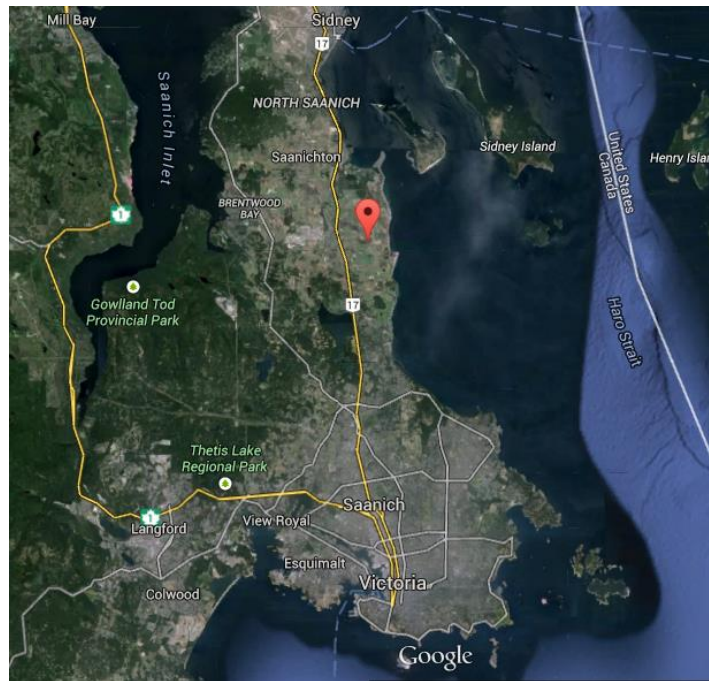


Figure 60. Test site

During the track tests, the weather was mainly calm and sunny without rain or snow. The mean measured temperature, pressure, and relative humidity were 14 C°, 1028 hPa, and 65 % respectively.

## **6.2 Test Method**

As illustrated in Figure 61, controlled velocity track tests were conducted by towing the trailer-based test rig behind a van being driven in three steps, namely: acceleration, constant speed (controlled velocity), and deceleration. During the tests, the car was accelerated to the desired controlled wind speed reported by the cup anemometer on the LabVIEW GUI in real time, and was then driven with constant speed before decelerating to stop at the end point. The rotor spin up (throttle/motor mode) was conducted before and during the acceleration step. As described in Chapter 4, the speed control system utilizes generator/motor torque supply (power production mode using the regenerative braking) and demand (throttle) using the LabVIEW-based closed loop control system paired with the EV controller, PMAC generator and 48 VDC battery bank. This control system enhanced a reliable fixed rotational speed operation in experiments conducted to obtain turbine's actual power coefficient versus tips speed ratio performance curve.

A test matrix consisted of multiple fixed rotational speeds ranging from 200 rpm to 450 rpm and relative wind speeds up to 17 m/s was utilized to collect sufficient data representing a broad range of tip speeds as well as controlled wind speeds. These towed tests were mostly conducted four times for each rotational speed and controlled wind speed case in periods from 20 seconds to 70 seconds, resulting in a total of 28800 seconds of collected data. The length of the track tests was limited between two power line crossings.

**Table 29.** Nominal targets of track test runs

Test run #	Rotor speed setpoint (RPM)	Controlled vehicle velocity (km/h)
1-5	200	30
6-9	250	30
10-13	300	25
14-18	350	25
19-22	400	20
23-26	450	45-60

The closed loop control gains and inputs were adjusted in real time to achieve desired functionality. Overall, the control system responded well to both negative net torque portion of the runs (mostly during acceleration), where the throttle power was fed to the motor to reach set speed, and positive net torque, where the regenerative braking was actuated to store the power back to the battery bank or dump it through heat using the dump load controller. The regenerative braking system was successfully capable of stopping the rotor instantly prior to the end of the deceleration part of the runs.

**Figure 61.** Controlled velocity track tests (towed scenario)

According to the CFD study presented in Chapter 5, the turbine rotor and wind sensors were out of the turbulent wake region behind the towing van, which is typically considered as a main challenge in velocity controlled track tests. In addition to the turbulent wake impacts, the road condition plays a key role in uncertainty associated with data collection using this test method. The selected paved road was mainly smooth with some small bumps and inconsistencies on the road surface. However, the road vibrations through the suspension introduced some towerhead motion.

### **6.3 Test Results and Discussions**

The main objective of the first set of experiments conducted utilizing the test rig was to assess the power coefficient versus tip speed ratio performance curve of the turbine (at a fixed yaw of zero) to validate the simulation results that were obtained using the BEM method. A total of 18 experiments were used for this purpose. Experiments were clustered based on the demanded fixed rotational speed maintained by the speed control system described in Chapter 4. Raw data was collected from LabVIEW-generated .tdms files. Subsequently, it was input into the MATLAB program to post-process and analyze the results.

As stated in Chapter 3, rotor rotational speed, cup wind speed, mechanical torque, and thrust force, temperature, and relative humidity data was primarily collected at 50 Hz while ultrasonic and pressure measurements were collected at 20 Hz and 1.8 Hz respectively. The rotor rotational speed, cup wind speed, mechanical torque, and thrust force were input into the developed MATLAB data analysis tool to post-process the raw data to analyze calculable parameters and their corresponding total uncertainty. In the steady state portion of each run, where rotor speed was held constant, the mechanical

torque was equal to the aerodynamic torque. As such mechanical torque was used to calculate the power output as formulated in Equation (3.61). Power coefficient, thrust coefficient, and tip speed ratio were calculated using the Equations (3.81), (3.91) and (3.99) respectively. Moreover, temperature, relative humidity, and pressure mean data was used to calculate the air density as explained in 3.6.2.

Data filtering of the rotor speed, cup wind speed, mechanical torque, thrust force, and calculable parameters (i.e. power, power coefficient, thrust coefficient, and tip speed ratio) included three steps. Initially, data pertaining to acceleration and deceleration portions of the runs was discarded. Secondly, four-second averaged data points were obtained. Finally, the total mean value corresponding to each parameter was averaged over a number of these four-second averaged data points (e.g. three data points), associated with an acceptable power coefficient range. Detailed automated uncertainty quantification, based on the equations presented in Chapter 3, were then used as part of the MATLAB tool to estimate the extent by which these sample mean values can represent the mean values of the actual populations under study.

As for the temperature, relative humidity, and pressure sensor, the mean values corresponding to each full run (at a set rotational speed) were simply used to calculate the air density. This platform has the capability of calculating the air density at finer intervals depending on the application requirements as well as potential design pattern modification in LabVIEW to better integrate the I/O signals from various types of sensors and transducers.

Shown in Figure 62, purely raw measured data collected from an extreme sample run (i.e. 450 RPM and 50 km/h) is presented prior to the analysis of the final performance curve. This experiment was conducted at 450 RPM (above rated) while the vehicle controlled velocity of around 13 m/s was maintained over a period of 23.2 seconds. As can be seen in Figure 62 (a), wind speed inflow controlled by the driver can be assumed relatively constant in a selected steady state section of the run (e.g. between 8 and 20 s). Although the illustrated data has no filtering, it suggests that calm atmospheric conditions and maintaining a constant towing vehicle velocity are fundamental to enable a (quasi) steady state test. The vehicle's cruise control can also be utilized at higher velocities to improve the accuracy in track testing.

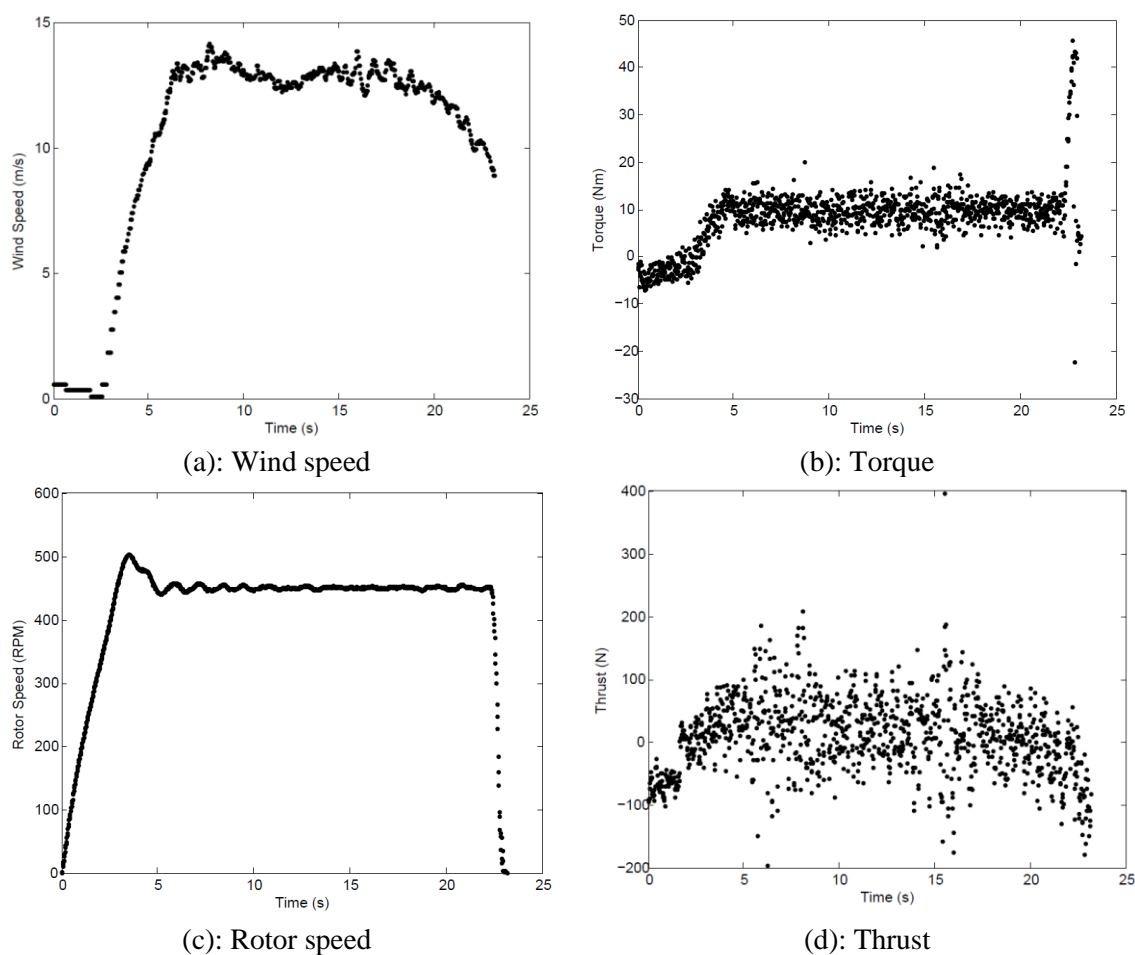


**Figure 62.** A full track test raw measured data at 50 Hz

Shown in Figure 62 (b), purely raw mechanical torque readings measured by the multi-axial loadcell is presented. As stated, in an assumed constant rotational speed portion of a run, this mechanical torque can be assumed to be equal to the aerodynamic torque. In Figure 62 (c), rotor rotational speed controlled by the closed loop system described in Chapter 4 is illustrated. As shown, demanded rotor speed of 450 RPM was successfully tracked. Relatively high rise and settling times observed in this extreme case were expected, given the generator torque supply and demand limitations imposed by the EV controller. As illustrated in Figure 62 (d), purely raw measured thrust data is scattered over a broad area. This scatter was predictable considering the direct impacts of road conditions and the considerable fore/aft movements of the tower head.

Raw power data, calculated using the torque and rotational speed data presented, is depicted in Figure 63. As shown, neglecting the acceleration and deceleration portions of the run, purely raw calculated power data points lay within a 200-Watt-wide area.

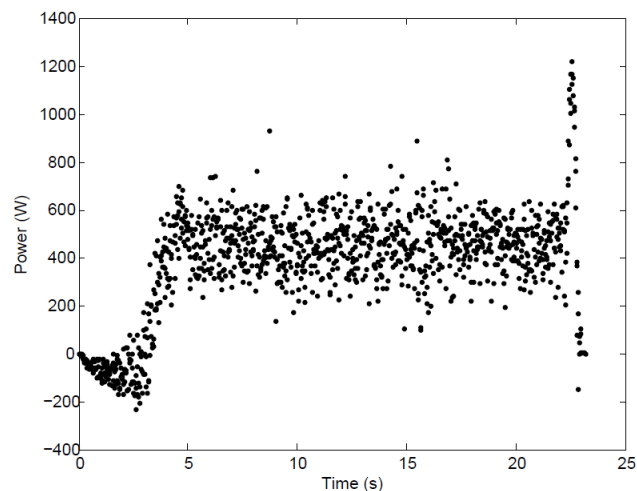


**Figure 63.** A full track test calculated power data

To elaborate on the procedure by which each experimental data point in the final performance plot was obtained, data filtering of the exact experiment introduced is presented in Figure 64. Four-second-averaged data points shown here, represent the mean (a) wind speed, (b) torque, (c) rotor speed, and (d) thrust values of samples of size 200. Discarding the acceleration and deceleration data provided three four-second-averaged data points which were then used to calculate the total mean values of the measurands.

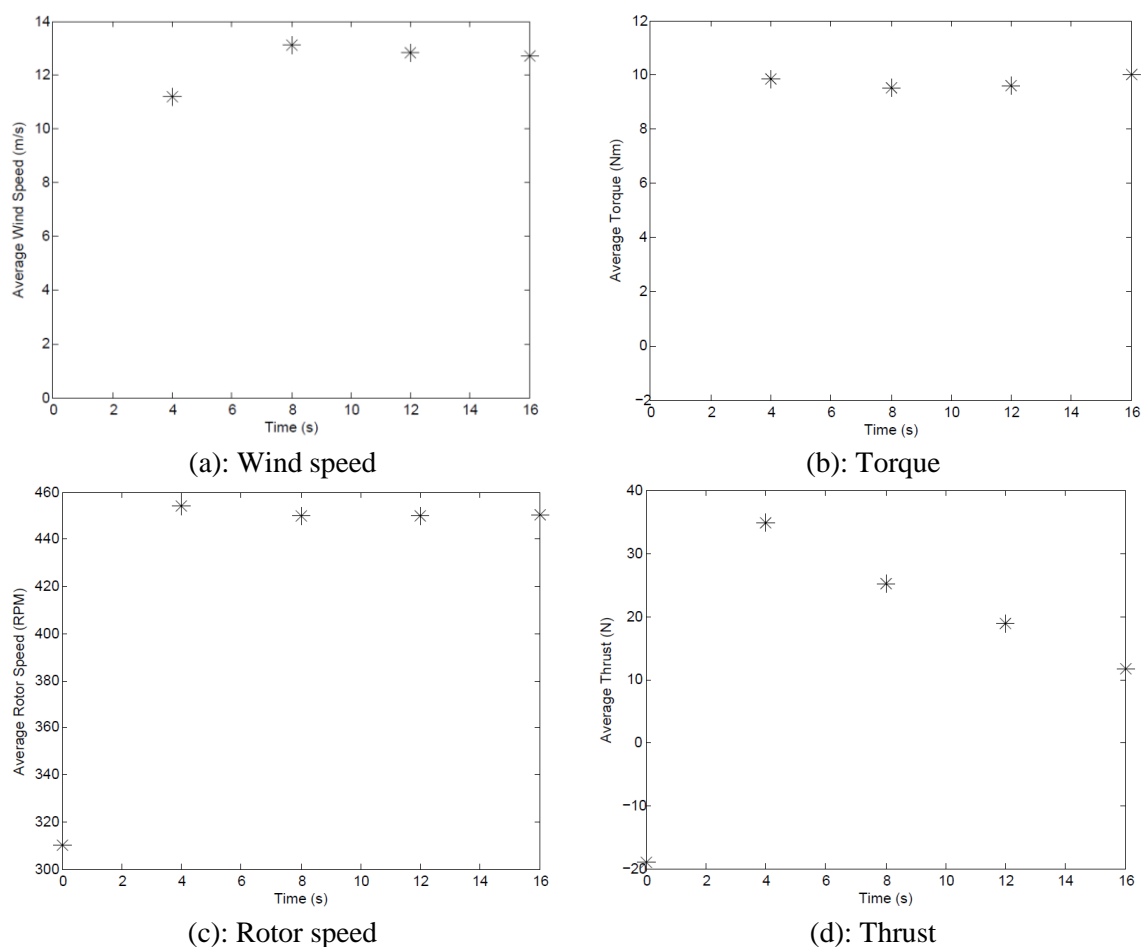


**Figure 64.** Average wind speed, torque, rotor speed, and thrust

In addition to these four directly measured parameters, calculable parameters such as power were averaged following the same principle. The four-second-averaged power data points are illustrated in Figure 65.

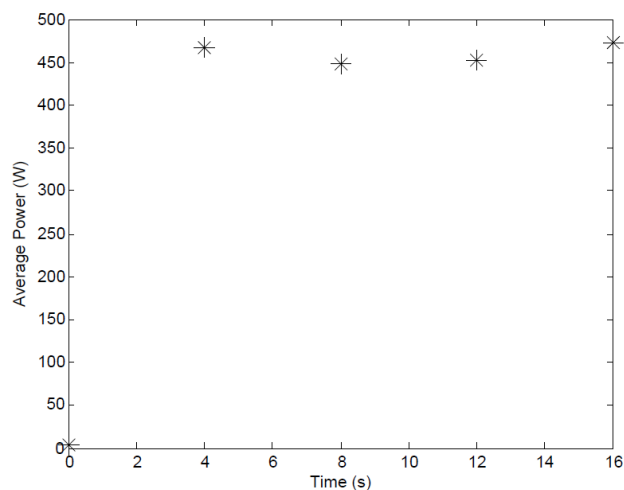


**Figure 65.** Average power

Upon conducting full uncertainty quantification on both measurable and calculable parameters (based on the SEM2-based approach as explained in Chapter 3) utilizing the developed data analysis tool, final propagated total uncertainty in the total mean power coefficient as well as tip speed ratio associated with each run were assessed. For the sample experiment under discussion, this information is summarized in Figure 66.

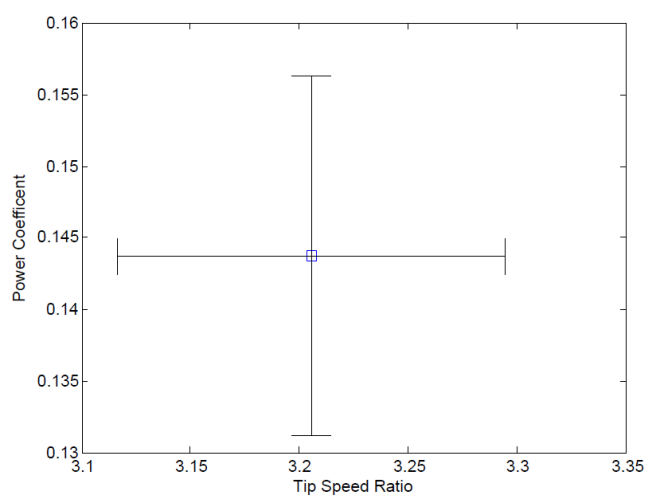


**Figure 66.** Total uncertainty bounds in mean power coefficient vs tip speed ratio

For a total of 19 experiments, the documented procedure was repeated to obtain final power coefficient versus tip speed ratio data points to construct the aggregate performance curve of the turbine rotor. As depicted in Figure 67, a final performance curve was constructed using these data points, classified in three rotor speeds of 200, 300, and 450 RPM. As mentioned, each data point represents a full experiment, accompanied with the total uncertainty assessment obtained using both bias and precision uncertainty components.

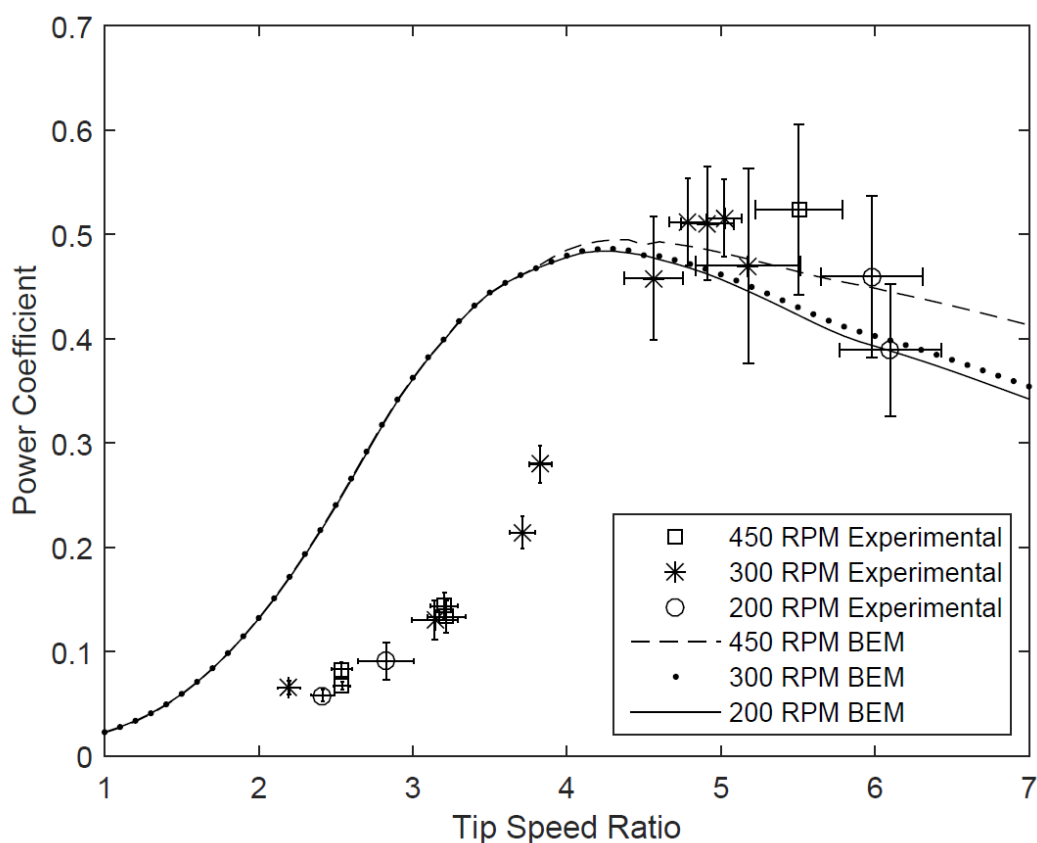


**Figure 67.** Power coefficient vs. tip speed ratio performance curve

As can be seen in Figure 67, three sets of BEM-generated simulation curves were compared against experimental data. Overall, above the peak power coefficient, the experimental and simulation results were in agreement within the experimental

uncertainty bounds, whereas below the peak, the agreement between the experimental and simulation results was questionable. When operating above the rated tip speed ratio, the simulation results roughly under predicted the actual performance. On the other hand, the simulations over predicted the actual power performance below rated.

Looking at the BEM results solely, it is apparent that the performance in low tip speed ratio region was almost identical while high tip speed ratio region revealed a discrepancy in the performance at different rotor speeds. When operating under a steady wind speed, lower tip speed ratios translate into lower rotor rotational speeds, leading to higher angles of attack, and hence causing the blades go into stall. Moreover, the BEM lacks the ability to model much of the flow physics in terms of stall characteristics of the airfoils to predict the angle of attack distribution in the presence of stall accurately.

According to Figure 67, total quantified uncertainty bounds in experimental data were more significant in above optimum tip speed ratio region compared to the area pertaining to lower tip speed ratios. Assuming a constant wind speed, high tip speed ratios correspond to low rotor speeds. As such, the larger uncertainty bounds could be caused by a potential increase in sensitivity to the road conditions, resulting in a decrease in the signal to noise ratio.

To further investigate the actual contribution of the bias (epistemic) and precision (aleatoric) components to the total uncertainty bounds, these elements were analyzed and depicted in Figure 68 and Figure 69 for the power coefficient and the tip speed ratio respectively.

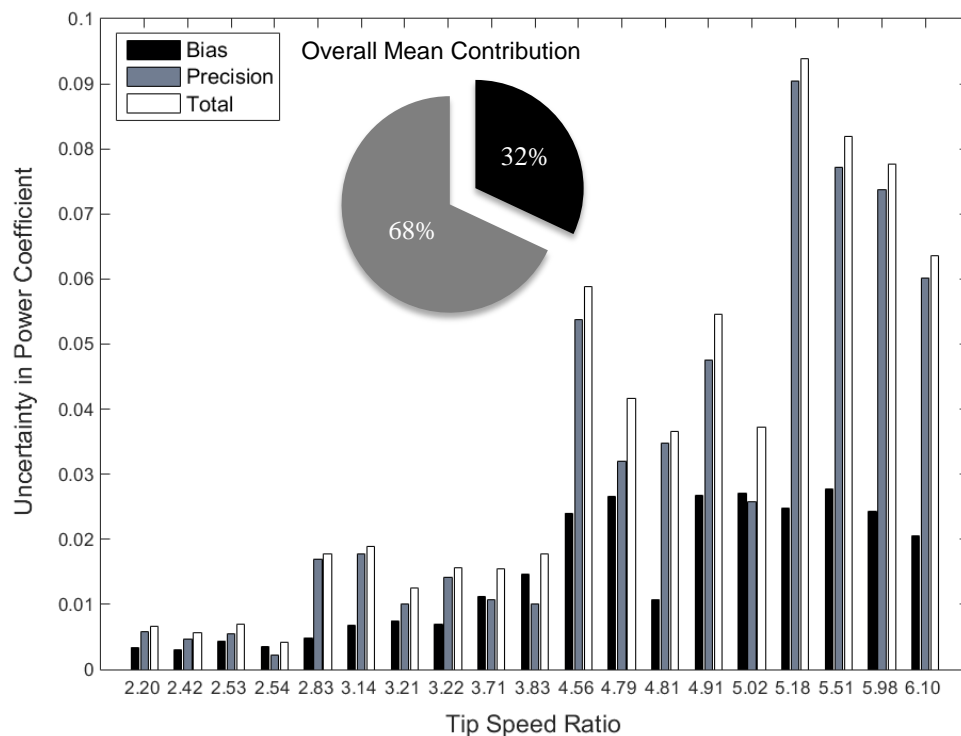


**Figure 68.** Uncertainty components of the power coefficient measurement

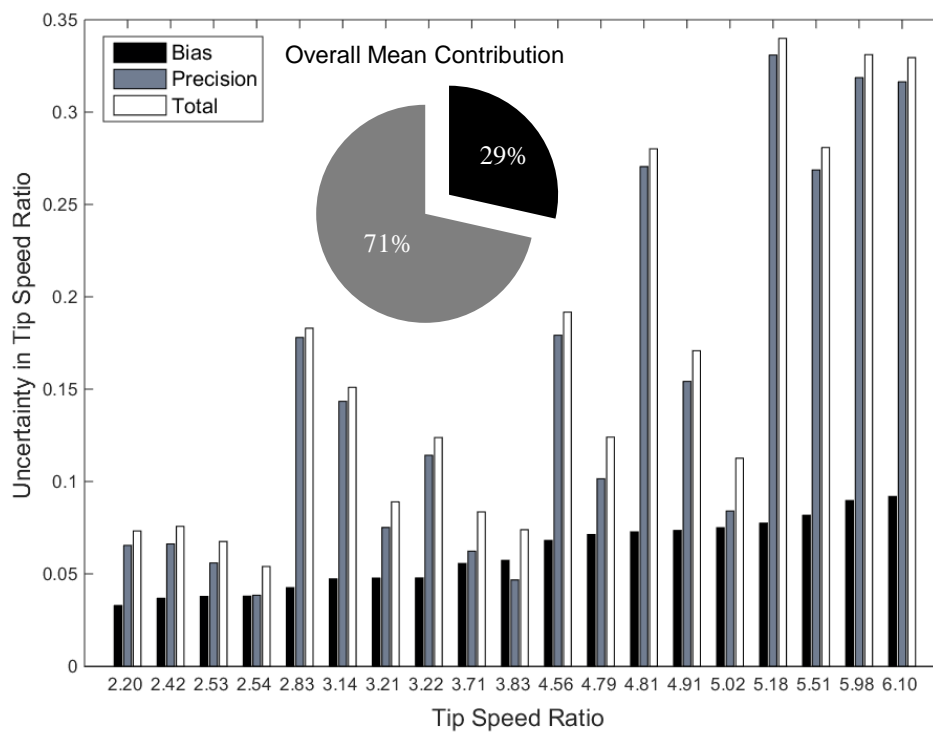


**Figure 69.** Uncertainty components of the tip speed ratio measurement

In Figure 68, the uncertainty components in the power coefficient measurements were plotted for various tests, identified by the mean tip speed ratio maintained throughout each run. As illustrated in Figure 69, these components were also analyzed for the tip speed ratio itself. Overall, the precision component had a higher contribution to the total uncertainty. Averaging over all the test runs, this contribution was estimated to be 68% of the total uncertainty in the power coefficient and 71% of the tip speed ratio measurements. On the other hand, bias elemental sources were estimated to cause only 32% and 29% of the total uncertainty in the power coefficient and the tip speed measurements respectively.

## Chapter 7: Conclusion and Recommendations

In this final chapter, the conclusion and recommendations for future work regarding the documented test rig will be presented.

### 7.1 Conclusion

The instrumentation of a custom trailer-based small wind turbine test rig was modified to facilitate small wind turbine experimental work. The instrumentation includes a multi-axial loadcell, an ultrasonic and cup anemometers, a wind vane, a temperature and relative humidity probe, a pressure sensor, a shaft encoder, and an active yaw mechanism.

A LabVIEW-based control system paired with a PMAC generator and a 48 VDC battery bank, was designed and implemented using an NI CRIO and an EV controller enhanced with the regenerative braking technology to enable full variable-speed control in real-time. The control system development process was completed in five steps, namely: system modeling in Simulink, system identification, control system design and analysis, control system implementation in LabVIEW, and PID controller Real-Time tuning. Furthermore, a custom GUI was developed to effectively interface the system.

A CFD analysis was also conducted to assess the potential impact of towing vehicle's disturbance on the free stream available to the rotor disc. It was found that the velocity profile at the rotor disc is uninfluenced by the wake generated at the rear of the tow vehicle given the hub height of the turbine. The test rig was then successfully and safely tested. A thorough uncertainty analysis was conducted to approximate the uncertainty

bounds associated with both aleotoric and epistemic components in measurable and calculable parameters. Finally, for a total of 19 experiments, the aggregate power coefficient versus tip speed ratio performance curve of the turbine was constructed. This experimental data was then compared with three sets of BEM-generated simulation curves. The comparison revealed that above the peak power coefficient, the experimental and simulation results were in agreement within the experimental uncertainty bounds, whereas below the peak power coefficient, the agreement between the experimental and simulation results was questionable.

This test rig which allows testing of up to 1kW wind turbines will now be used as a platform for real-time speed control. It can be towed behind a vehicle to conduct steady state tests or it can be parked in an open area to collect unsteady field data.

## **7.2 Recommendations for Future Work**

As pointed in 2.3.4, due to time constraints and mechanical issues, experiments in the current study were conducted in a fixed-yaw position. Upon mitigating the mechanical issues, another closed-loop control system can be added to the main GUI to control the yaw actively. Wind vane data can be used for traction of the setpoint position. The main LabVIEW project is structured in a way that the yaw control system can also be accessed through the existing GUI. More details regarding this potential modification is discussed in Appendix B.

As discussed in Chapter 4, the current LabVIEW-based control system's capability is constrained to the EV controller's internal actions. As such, a Sevcon Gen4 PC-based programming kit can be utilized to actually program and monitor the EV controller

performance in real-time. This will allow the future users to use the conversion constants more accurately and re-tune the PI controller accordingly.

The current platform has also the capability of implementing new control strategies to conduct unsteady experiments such as the optimum tip speed ratio traction. In order to maintain the optimum tip speed ratio, the current closed loop speed (torque) control system can be used within a broader closed loop algorithm coupled with the wind speed data to effectively vary the rotational speed as the wind inflow velocity changes.

In order to have a more rigorous CFD assessment of the towing vehicle's wake, the actual turbine can be added to the simulation using an actuator disc model. In addition, the boundary conditions of the symmetry and ground can be modified from the free-slip wall boundary condition to a no-slip moving boundary condition at the ground which, in turn, is moving with the same stationary velocity. Another alternative would be utilizing the LES techniques rather than the currently used RANS.

Furthermore, the cross talk compensation documented in 3.5.1 can be added to the main LabVIEW project or the developed post processing tool to reduce the uncertainty in multi-axial loadcell measurements. Due to time constraints of the inherent multi-faceted research work, the conversion data was only used from the manufacturer cross talk data presented in Appendix A.

For the results documented in Chapter 6, the cup anemometer was used for the wind speed measurements primarily to enable an alternative test scenario of mounting the ultrasonic anemometer at the rear of the turbine to capture the wake data. In addition, deterministic timing consideration was the second reason behind using cup data. The cup

wind speed block was placed inside the same Timed Loop synchronized to the scan engine of the CRIO within the LabVIEW program. The details regarding the Producer Consumer architecture used for the data acquisition via the GUI is explained in Appendix B. On the other hand, the ultrasonic wind speed block which was placed inside a separate While loop parallel to the main Timed Loop communicating in serial, was used as a reference for the wind speed measurements only. Initial comparison revealed approximately a 1 m/s discrepancy between the measured wind speeds from the two sensors.

Future work could include using a third reference anemometer to characterize the ultrasonic and cup anemometers performance. Once the optimum tip speed ratio traction control algorithm is added, the ultrasonic anemometer can be used as shown in Figure 5. In this configuration, the cup anemometer measurement is fed back to the controller, while the ultrasonic anemometer captures the wake passing the rotor disc.

## Bibliography

- [1] Wind Energy Foundation. (2014). [Online]. Available:  
<http://www.windenergyfoundation.org/about-wind-energy/history>
- [2] O. Edenhofer et al., “Renewable energy sources and climate change mitigation: special report of the Intergovernmental Panel on Climate Change,” Potsdam Institute for Climate Impact Research (PIK). 2012. Cambridge University Press. ISBN 978-1-107-60710-1.
- [3] Global Wind Energy Council. (2014). [Online]. *Global Wind Report, Annual Market Update 2013*. Available: [http://www.gwec.net/wp-content/uploads/2014/04/GWEC-Global-Wind-Report\\_9-April-2014.pdf](http://www.gwec.net/wp-content/uploads/2014/04/GWEC-Global-Wind-Report_9-April-2014.pdf)
- [4] Canadian Wind Energy Association. (2014). [Online]. Available:  
<http://canwea.ca/wind-energy/installed-capacity/>
- [5] Wind turbines - Part 2: Small wind turbines, IEC 61400-2 ed3.0, 2013.
- [6] American Wind Energy Association. (2014). [Online]. Available:  
<http://www.awea.org/Issues/Content.aspx?ItemNumber=4592&navItemNumber=723>
- [7] Canadian Wind Energy Association. (2014). [Online]. Available:  
<http://canwea.ca/communities/small-wind-energy/>
- [8] Distributed Wind Energy Association. (2014). [Online]. Available:  
<http://distributedwind.org/home/learn-about-distributed-wind/what-is-distributed-wind/>
- [9] Wind turbines - Part 12-2: Power performance of electricity-producing wind turbines based on nacelle anemometry, IEC 61400-12-1 ed.1.0., 2013.
- [10] D. Corbus and M. M. Nrel. (2005). [Online]. *Small Wind Research Final Report*. Available: <http://www.nrel.gov/docs/fy06osti/38550.pdf>
- [11] M. Refan and H. Hangan, “Experimental and Theoretical Study on the Aerodynamic Performance of a Small Horizontal Axis Wind Turbine,” ASME 2010 Power Conference. Paper No. POWER2010-27174, pp. 629-635.  
 doi:10.1115/POWER2010-27174.
- [12] H. Matsumiya et al., “Field Operation and Track Tests of 1-kW Small Wind Turbine Under High Wind Conditions,” *J. Sol. Energy Eng.* 132(1), 011002. 2009.  
 doi:10.1115/1.4000330.

- [13] Small Wind Turbine Testing Options. Small Wind Certificate Council. (2014). [Online]. Available: <http://smallwindcertification.org/for-applicants/small-turbines/application-process-small/field-testing-small/>
- [14] S. Larwood et al., “Controlled Velocity Testing of an 8-kW Wind Turbine,” *AWEA WindPower 2001 Conference*. Washington, D.C. NREL/CP-500-30299.
- [15] Q. Song and W. D. Lubitz, “BEM Simulation and Performance Analysis of a Small Wind Turbine Rotor,” *Wind Eng.*, vol. 37, pp. 381–400, 2013.
- [16] H. Mamur, “Design , application , and power performance analyses of a micro wind turbine,” *Turk J Elec Eng Comp Sci*, pp. 1–19, 2015.
- [17] J. Elizondo et al., “Experimental study of a small wind turbine for low- and medium-sind regimes,” *Int. J. energy Res.*, vol. 33, pp. 309–326, 2008. doi: 10.1002/er.1482.
- [18] H. Grassmann et al., “A partially static turbine-first experimental results,” *Renew. Energy*, vol. 28, pp. 1779–1785, 2003.
- [19] A. Magni, “Development of a trailer based small wind turbine experimental rig,” University of Victoria, Canada, MECH 498 Rep, 2012.
- [20] Stratasy Fortus 400mc Systems. (2014). [Online]. Available: <http://www.stratasy.com/3d-printers/production-series/fortus-360-400mc>
- [21] Novatech F233 Load cell. (2014). [Online]. Available: <http://www.novatechloadcells.co.uk/ds/f233.htm>
- [22] 81000 Young ultrasonic anemometer manual. (2014). [Online]. Available: <http://www.youngusa.com/products/6/3.html>
- [23] Gill Instruments. (2014). [Online]. Available: <http://www.gillinstruments.com/products/anemometer/principleofoperation.htm>
- [24] RM Young 81000 ultrasonic anemometer. (2014). [Online]. Available: <http://www.youngusa.com/products/6/3.html>
- [25] B. Bailey et al., “*Wind resource assessment handbook: Fundamentals for conducting a successful monitoring program*,” Prepared for National Renewable Energy Laboratory. AWS S.,Inc., Albany, NY (US). (1997). NREL Subcontract No. TAT-5-15283-01.
- [26] NRG Systems #40C Anemometer. (2014). [Online]. Available: <http://www.nrgsystems.com/sitecore/content/products/1900.aspx>
- [27] NRG Systems Interface 892E. (2014). [Online]. Available: <http://www.renewablenrgsystems.com/products/2041/interface-40-logic-level-speed-amp.aspx>

- [28] NRG Systems aligning wind vanes application note. (2014). [Online]. Available: <https://www.renewableenergysystems.com/FileLibrary/06ca5884670a408a876628ed105da095/anvanealign.pdf>
- [29] Natural Resources Canada magnetic declination calculator. (2014). [Online]. Available: <http://geomag.nrcan.gc.ca/calc/mdcal-eng.php>
- [30] NRG Systems. (2014). [Online]. Available: <http://www.nrgsystems.com/sublayouts/C2ECFSpecificationGlossary.aspx?pid=SPEC-I:1904%20G:5%20S:181>
- [31] NRG Systems NRG #200P Wind Direction Vane. (2014). [Online]. Available: <http://www.nrgsystems.com/sitecore/content/Products/1904.aspx>
- [32] RM Young Barometric Pressure Sensor. (2014). [Online]. Available: <http://www.youngusa.com/products/3/22.html>
- [33] Campbell Scientific HC2-S3-L temperature and relative humidity probe. (2014). [Online]. Available: [https://s.campbellsci.com/documents/ca/brochures/component/hc2-s3-l\\_br.pdf](https://s.campbellsci.com/documents/ca/brochures/component/hc2-s3-l_br.pdf)
- [34] Campbell Scientific Gill radiation shield brochure. (2014). [Online]. Available: [https://s.campbellsci.com/documents/ca/brochures/component/41003\\_br.pdf](https://s.campbellsci.com/documents/ca/brochures/component/41003_br.pdf)
- [35] Global Encoder IH103 manual. (2014). [Online]. Available: <https://www.inverterdrive.com/file/Global-Encoder-IH103-Manual>
- [36] Midwest Motion Products. (2014). [Online]. Available: <http://www.midwestmotion.com/products/brushed.html>
- [37] A. Magni “Wind Turbine Test Rig Electrical Design,” University of Victoria, Canada, Rep, 2012.
- [38] Motenergy Brushless PMAC ME0907. (2014). [Online]. Available: <http://www.thunderstruck-ev.com/motenergy-brushless-pmac-me0907.html>
- [39] Sevcon Gen4 motor controller manual. (2014). [Online]. Available: [http://www.thunderstruck-ev.com/Manuals/Gen4\\_Product\\_Manual\\_V3.0.pdf](http://www.thunderstruck-ev.com/Manuals/Gen4_Product_Manual_V3.0.pdf)
- [40] MK 8A27 DEKA battery. (2014). [Online]. Available: <http://www.mkbattery.com/images/8A27-DEKA.pdf>
- [41] MorningStar TriStar controller. (2014). [Online]. Available: <http://www.morningstarcorp.com/wp-content/uploads/2014/02/TriStar-Datasheet-English.pdf>
- [42] Midwest Motion Products brushed DC gear motor. (2014). [Online]. Available: <http://www.midwestmotion.com/products/brushed.html>

- [43] National Instruments LabVIEW for CompactRIO developer's guide: recommended LabVIEW architectures and development practices for control and monitoring applications. (2014). [Online]. Available: <http://www.ni.com/pdf/products/us/fullcriodevguide.pdf>
- [44] National Instruments operating instructions and specifications for CompactRIO. (2014). [Online]. Available: <http://www.ni.com/pdf/manuals/375102d.pdf>
- [45] A. Mills and B. Chang, "Error analysis of experiments: a manual for engineering students," University of California, 2004.
- [46] A. Wheeler and A. Ganji, "Introduction to Engineering Experimentation," 3rd ed. Upper Saddle River, NJ, Prentice Hall, 2010.
- [47] Test uncertainty, Part 1, ASME PTC 19.1 – 1998.
- [48] National Instruments. Determining the accuracy of your strain gage measurements. (2014). [Online]. Available: <http://www.ni.com/white-paper/8909/en/#toc2>
- [49] National Instruments operating instructions and specifications for NI 9237. (2014). [Online]. Available: <http://www.ni.com/pdf/manuals/374186e.pdf>
- [50] National Instruments operating instructions and specifications for NI 9201. (2014). [Online]. Available: <http://www.ni.com/pdf/manuals/373783g.pdf>
- [51] National Instruments operating instructions and specifications for NI 9263. (2014). [Online]. Available: <http://www.ni.com/pdf/manuals/373781e.pdf>
- [52] D. Schrand, "Cross-Talk Compensation Using Matrix Methods," *Sensors & Transducers*, vol. 79, no. 5, pp. 1157–1163, 2007.
- [53] G. Purves. (2013, Feb. 25). *Cross-talk data for F233-Z4147* [Online]. Available e-mail: [info@novatechloadcells.co.uk](mailto:info@novatechloadcells.co.uk)
- [54] NRG Systems #40C Anemometer uncertainty application note. (2014). [Online]. Available: <https://www.renewablenrgsystems.com/FileLibrary/88b3a4199c8349eaaf2ca8128a94a564/an40Uncertainty.pdf>
- [55] R. V Coquilla and J. Obermeier, "Calibration uncertainty comparisons between various anemometers," Otech Engineering, Inc., Davis, CA, 2008.
- [56] T. Burton et al., *Wind Energy Handbook*, 2nd ed. John Wiley & Sons, Ltd. 2011.
- [57] Z. Farkas, "Considering air density in wind power production," arXiv:1103.2198 [physics.gen-ph], pp. 1–6, 2011.

- [58] A. Picard et al., "Revised formula for the density of moist air (CIPM-2007)," *Metrologia*, vol. 45, no. 2, pp. 149–155, Apr. 2008.
- [59] B. Wu et al., *Power Conversion and Control of Wind Energy Systems*. Hoboken, N.J. : Piscataway, NJ: Wiley ; IEEE Press, 2011.
- [60] A. Wright, "Modern Control Design for Flexible Wind Turbines," National Renewable Energy Laboratory, Golden, Colorado, NREL/TP-500-35816, 2004.
- [61] Ampair 600 wind turbine manual. Remote Power Inc. (2007). [Online]. Available: [http://www.remotepowerinc.com/documents/Ampair\\_600\\_manual.pdf](http://www.remotepowerinc.com/documents/Ampair_600_manual.pdf)
- [62] US DOE, "20% wind energy by 2030: increasing wind energy's contribution to US electricity supply," US Department of Energy, Washington, DC, 248 pp. DOE/GO-102008-2567, 2008. Available: <http://www.nrel.gov/docs/fy08osti/41869.pdf>
- [63] J. Jonkman, "TurbSim user's guide: version 1.50," National Renewable Energy Laboratory, Golden, Colorado, NREL/TP-500-46198, 2009. Available: <http://www.nrel.gov/docs/fy09osti/46198.pdf>
- [64] P. Moriarty and A. Hansen, "AeroDyn theory manual," National Renewable Energy Laboratory, Golden, Colorado, NREL/TP-500-36881, 2005. Available: <http://www.nrel.gov/docs/fy05osti/36881.pdf>
- [65] J. Jonkman and M. Buhl, "FAST user's guide," National Renewable Energy Laboratory, Golden, Colorado, NREL/EL-500-38230, 2005. Available: <http://wind.nrel.gov/public/bjonkman/TestPage/FAST.pdf>
- [66] S. Mueeen et al., "Wind turbine modeling," *Stability Augmentation of a Grid-Connected Wind Farm*. London: Springer, Ch. 2, pp. 37-73, 2009.
- [67] A. Rolan et al., "Modeling of a variable speed wind turbine with a permanent magnet synchronous generator," in *Industrial Electronics, 2009. ISIE 2009. IEEE International Symposium on*, 2009, pp. 734-739.
- [68] M. Jardin, "Improving mass moment of inertia measurements," MathWorks. (2014). [Online]. Available: <http://www.mathworks.com/company/newsletters/articles/improving-mass-moment-of-inertia-measurements.html>
- [69] L. Ljung, "System Identification Toolbox™ user's guide," R2014b, The MathWorks, Inc. Natick, MA, 2014. Available:
- [70] Control Design, MATLAB and Simulink for control design acceleration, MathWorks Training Services, 2011.
- [71] National Instruments LabVIEW™ PID and Fuzzy Logic Toolkit user manual. 372192D-01, 2009. Available: <http://www.ni.com/pdf/manuals/372192d.pdf>

- [72] National Instruments PID Theory Explained. (2011). [Online]. Available: <http://www.ni.com/white-paper/3782/en/>
- [73] Control tutorials for MATLAB and Simulink, "Introduction: PID Controller Design," 2014. [Online]. Available: <http://ctms.engin.umich.edu/CTMS/index.php?example=Introduction&section=ControlPID>
- [74] G. Franck et al., "Numerical simulation of the flow around the ahmed vehicle model," 2009.
- [75] P. Bearman and T. Morel, "Effect of free stream turbulence on the flow around bluff bodies," *Prog. Aerospace Sci.*, vol. 20, pp. 97-123, 1983.
- [76] P. Bearman, "Bluff body flow research with application to road vehicles," *The aerodynamics of heavy vehicles ii: trucks, buses, and trains*, Lecture Notes in Applied and Computational Mechanics, Volume 41, 2009, pp 3-132009.
- [77] G. Eggenspieler, "Turbulence modeling," ANSYS Inc. (2011). [Online]: Available: <http://www.ansys.com/staticassets/ANSYS/Conference/Confidence/San%20Jose/Downloads/turbulence-summary-4.pdf>
- [78] R. Strachan et al., "The vortex structure behind an Ahmed reference model in the presence of a moving ground plane," *Exp. Fluids*, vol. 42, pp. 659–669, 2007.
- [79] F. Menter, "Two-equation eddy-viscosity turbulence models for engineering applications," *AIAA Journal*, 1994; doi: 10.2514/3.12149.
- [80] F. Menter et al., "Ten years of industrial experience with the SST turbulence model," *Turbul. Heat Mass Transf.* 4, vol. 4, pp. 625–632, 2003.
- [81] ANSYS CFX Help (2013). Available: <http://www.ansys.com/Products/Simulation+Technology/Fluid+Dynamics/Fluid+Dynamics+Products/ANSYS+CFX>

## Appendix

### Appendix A. Loadcell Crosstalk Data and Certificate of Test and Calibration



Cross-talk data for F233-Z4147, S/N 45778

	Fz output mV	Tz output mV	Mx output mV	My output mV
Fz+ load		-0.2204	-0.3059	-0.0324
Fz- load		0.1997	0.2091	0.2922
Tz+ load	-0.0099		-0.0373	0.1324
Tz- load	0.0060		-0.0450	-0.1930
Mx+ load	-0.2074	0.0306		-0.0571
Mx- load	0.2133	0.0292		0.0649
My+ load	-0.0506	0.0114	0.0133	
My- load	-0.0246	-0.0485	0.0530	

06/06/2012



### Certificate Of Test & Calibration

Customer:	University of Victoria		
Customer order:	Ref: Alan Magni		
Works order:	17288	Nominal range:	900N
Loadcell type:	F233-Z4147	Serial number:	45778
Special features:	FZ Axis		

#### Loadcell Connections

	Connector	Wire colour
Power supply - positive		red
Power supply - negative		blue
Comp. signal high*		yellow
Comp. signal low*		green
Screen		Orange (thick)

\* Reverse for tension only loadcells

Loadcell supply:	10.000V	Insulation resistance:	>500Mohms
Zero balance:	-0.350mV	Input resistance:	757ohms
Range calibrated	900N		

Applied Load N	Loadcell Output mV			
	Compression		Tension	
	Increase	Decrease	Increase	Decrease
000.0			0.000	0.001
450.0			3.490	3.492
900.0			6.981	
Output	mV/V		0.6981mV/V	

Calibration engineer: D Shipton

Date: 31/05/2012

Inspector: Michael Blake

Date: 07:06:12

This loadcell has been calibrated in a dead weight rig using standards that are traceable to European Standards.

Novatech Measurements Limited  
 83 Castleham Road, St. Leonards-on-Sea, East Sussex, TN38 9NT.  
 Tel: 01424 852744 www.novatechloadcells.co.uk Fax: 01424 853002



### Certificate Of Test & Calibration

Customer:	University of Victoria		
Customer order:	Ref: Alan Magni		
Works order:	17288	Nominal range:	900N
Loadcell type:	F233-Z4147	Serial number:	45778
Special features:	FZ Axis		

#### Loadcell Connections

	Connector	Wire colour
Power supply - positive		red
Power supply - negative		blue
Comp. signal high*		yellow
Comp. signal low*		green
Screen		Orange (thick)

\* Reverse for tension only loadcells

Loadcell supply:	10.000V	Insulation resistance:	>500Mohms
Zero balance:	-0.366mV	Input resistance:	757ohms
Range calibrated	900N		

Applied Load N	Loadcell Output mV			
	Compression		Tension	
	Increase	Decrease	Increase	Decrease
000.0	0.000	0.000		
450.0	-3.402	-3.403		
900.0	-6.802			
Output	-0.6802mV/V		mV/V	

Calibration engineer: D Shipton

Date: 01/06/2012

Inspector: *Michael Blake*

Date: *07:06:12*

This loadcell has been calibrated in a transfer standard rig using standards that are traceable to European Standards.

Novatech Measurements Limited  
 83 Castleham Road, St. Leonards-on-Sea, East Sussex, TN38 9NT.  
 Tel: 01424 852744 www.novatechloadcells.co.uk Fax: 01424 853002



### Certificate Of Product Test / Calibration

Customer:	University of Victoria		
Customer order:	Ref: Alan Magni		
Works order:	17288	Nominal range:	75Nm
Loadcell type:	F233-Z4147	Serial number:	45778
Special features:	Tz Axis		

#### Transducer Connections

	Connector	Wire colour
Power supply - positive		violet
Power supply - negative		black
Signal high		brown
Signal low		white
Screen		Orange (thick)

Transducer supply:	10V	Insulation resistance:	>500Mohms
Zero balance:	-0.134mV	Input resistance:	756ohms
Range calibrated	75Nm		

Applied Torque Nm	Transducer Output mV			
	Tz+		Tz-	
	Increase	Decrease	Increase	Decrease
00.0	0.000	0.005	0.000	0.001
37.5	5.298	5.299	-5.294	-5.306
75.0	10.605		-10.601	
Output	1.0605mV/V		-1.0601mV/V	

Calibration engineer: D Shipton

Date: 06/06/2012

Inspector: Michael Blake

Date: 07-06-12

Novatech Measurements Limited  
 83 Castleham Road, St. Leonards-on-Sea, East Sussex, TN38 9NT.  
 Tel: 01424 852744 www.novatechloadcells.co.uk Fax: 01424 853002

TTC0208



### Certificate Of Product Test / Calibration

Customer:	University of Victoria		
Customer order:	Ref: Alan Magni		
Works order:	17288	Nominal range:	75Nm
Loadcell type:	F233-Z4147	Serial number:	45778
Special features:	Mx Axis		

#### Transducer Connections

	Connector	Wire colour
Power supply - positive		orange
Power supply - negative		turquoise
Signal high		pink
Signal low		grey
Screen		Orange (thick)

Transducer supply:	10V	Insulation resistance:	>500Mohms
Zero balance:	0.136mV	Input resistance:	387ohms
Range calibrated	75Nm		

Applied Torque Nm	Transducer Output mV			
	Mx+		Mx-	
	Increase	Decrease	Increase	Decrease
00.0	0.000	0.009	0.000	-0.006
37.5	5.347	5.349	-5.306	-5.319
75.0	10.684		-10.612	
Output	1.0684mV/V		-1.0612mV/V	

Calibration engineer: D Shipton

Date: 06/06/2012

Inspector:

Michael Blake

Date:

07:06:12

Novatech Measurements Limited  
 83 Castleham Road, St. Leonards-on-Sea, East Sussex, TN38 9NT.  
 Tel: 01424 852744 www.novatechloadcells.co.uk Fax: 01424 853002



### Certificate Of Product Test / Calibration

Customer:	University of Victoria		
Customer order:	Ref: Alan Magni		
Works order:	17288	Nominal range:	75Nm
Loadcell type:	F233-Z4147	Serial number:	45778
Special features:	My Axis		

#### Transducer Connections

	Connector	Wire colour
Power supply - positive		red/blue
Power supply - negative		white/red
Signal high		yellow/red
Signal low		green/brown
Screen		Orange (thick)

Transducer supply:	10V	Insulation resistance:	>500Mohms
Zero balance:	0.136mV	Input resistance:	387ohms
Range calibrated	75Nm		

Applied Torque Nm	Transducer Output mV			
	My+		My-	
	Increase	Decrease	Increase	Decrease
00.0	0.000	0.005	0.000	-0.004
37.5	5.363	5.386	-5.293	-5.318
75.0	10.749		-10.650	
Output	1.0749mV/V		-1.0650mV/V	

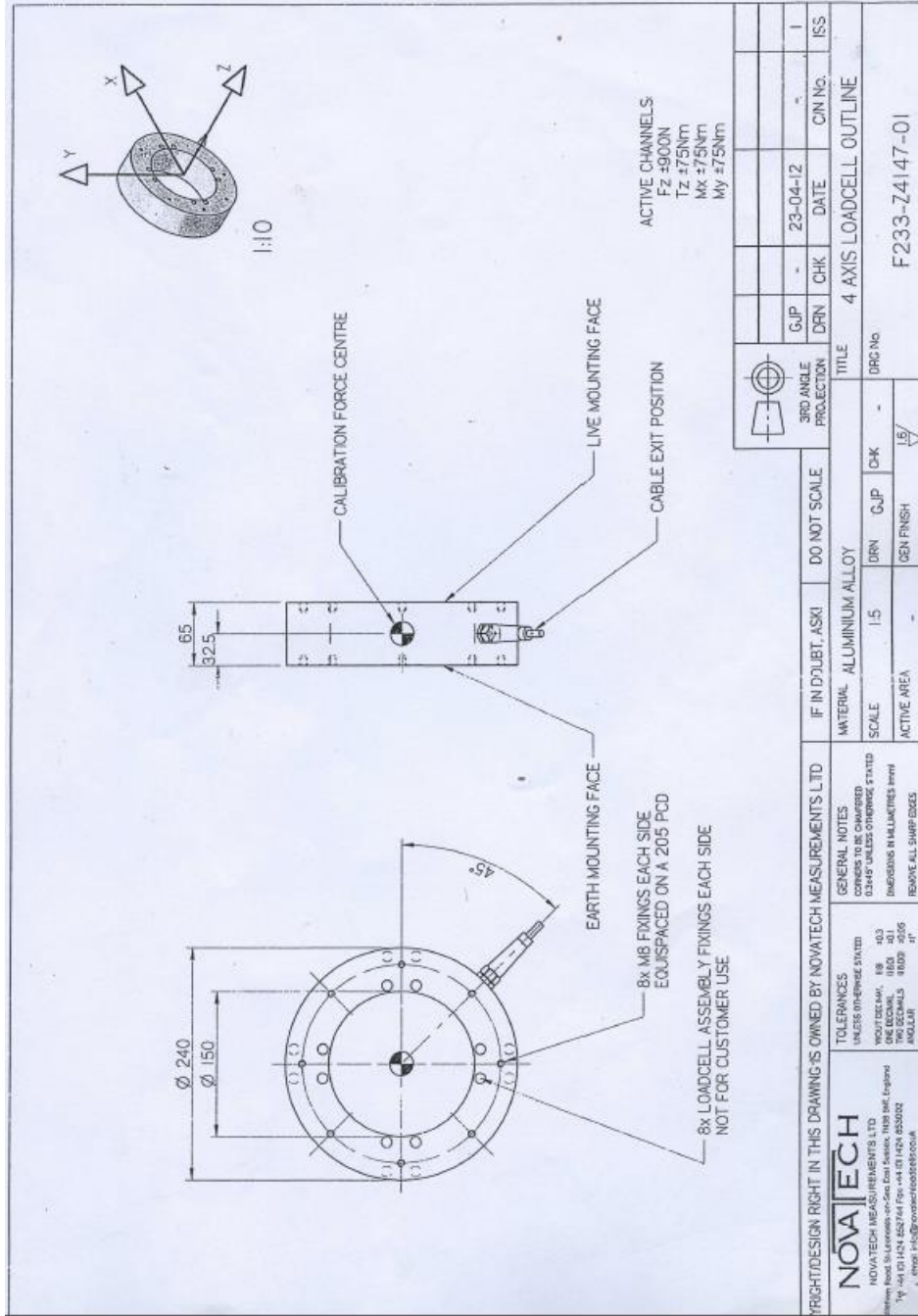
Calibration engineer: D Shipton

Date: 06/06/2012

Inspector: Michael Blake

Date: 07:06:12

Novatech Measurements Limited  
 83 Castleham Road, St. Leonards-on-Sea, East Sussex, TN38 9NT.  
 Tel: 01424 852744 www.novatechloadcells.co.uk Fax: 01424 853002



## **Appendix B. Test Rig Operational Work Instructions**

Since this thesis is also meant to be used as a manual for the operation of the test rig developed, this section will cover work instructions for both custom LabVIEW GUI developed to control, monitor, and effective data acquisition as well as the control cabinet interface.

### **B.1 LabVIEW Graphical User Interface (GUI) Work Instruction**

The majority of the project time was spent on the instrumentation and LabVIEW application development using a range of digital, analog, and serial modules within the CRIO platform. As illustrated in Figure 27, a GUI was developed to interface the whole system, adjust the control system inputs and monitor operational parameters in real-time.

As a reusable solution, a custom LabVIEW real-time producer/consumer design pattern was utilized to develop the main LabVIEW VI (code) coupled with the GUI shown in Figure 27. In general, when using LabVIEW Real-time and LabVIEW FPGA, there are two programming modes that can be used to develop an application using CRIO, namely: FPGA Interface, and Scan Interface. A hybrid mode can also be used as a combination of these two modes.

When high speed data acquisition is not a key objective in an application, the scan interface can be utilized which provides a range of benefits such as ease of programming (i.e. I/O variable scan be directly dragged and dropped into LabVIEW real-time vi during development), ability to dynamically detect I/O modules, fault engine, and diagnostics and debugging (i.e. using Distributed System Manager, current values and faults can be viewed while the program is running) [43].

Based on the specifics of the application to effectively interface the test rig through the available CRIO modules, the application was programmed in scan mode using three sets of producer and consumer loops placed in a four-step flat sequence structure. A producer loop is responsible to acquire and send data between sensors and CRIO deterministically while a consumer loop receives and logs data to disc. Data can be transferred between these two loops using Real-time first-in-first-out buffers known as RT FIFOs that behave deterministically. Other techniques available in [43] can also be utilized to implement a range of design pattern development for CRIO applications.

The first set of producer and consumer loops shown in Figure 70, was constructed using a deterministic timed loop synchronized to the scan engine of the CRIO as well as a consumer while loop. All non-serial data acquisition and controls are being done within these loops. The speed control system discussed in Chapter 4 is also placed within this first producer loop.

Due to the inherently different functionality of serial communications, two additional sets of producer/consumer loops were developed to communicate with the two serial sensors of the test rig. The second set of producer/consumer loops depicted in Figure 71, is responsible for the ultrasonic anemometer measurements while the third set, shown in Figure 72, is only in charge of pressure measurements.

It is worth mentioning that the application was developed such that once the mechanical and connection issues associated with the yaw system are removed; the NI 9505 module provided to control the yaw drive (only programmable in FPGA mode) can be easily added to the application. Final application can then be structured in a hybrid mode as

explained in [43], essentially having the NI 9505 module in FPGA and all other modules (i.e NI 9237, NI 9263, NI 9201, NI 9411, and NI 9870) in scan mode.

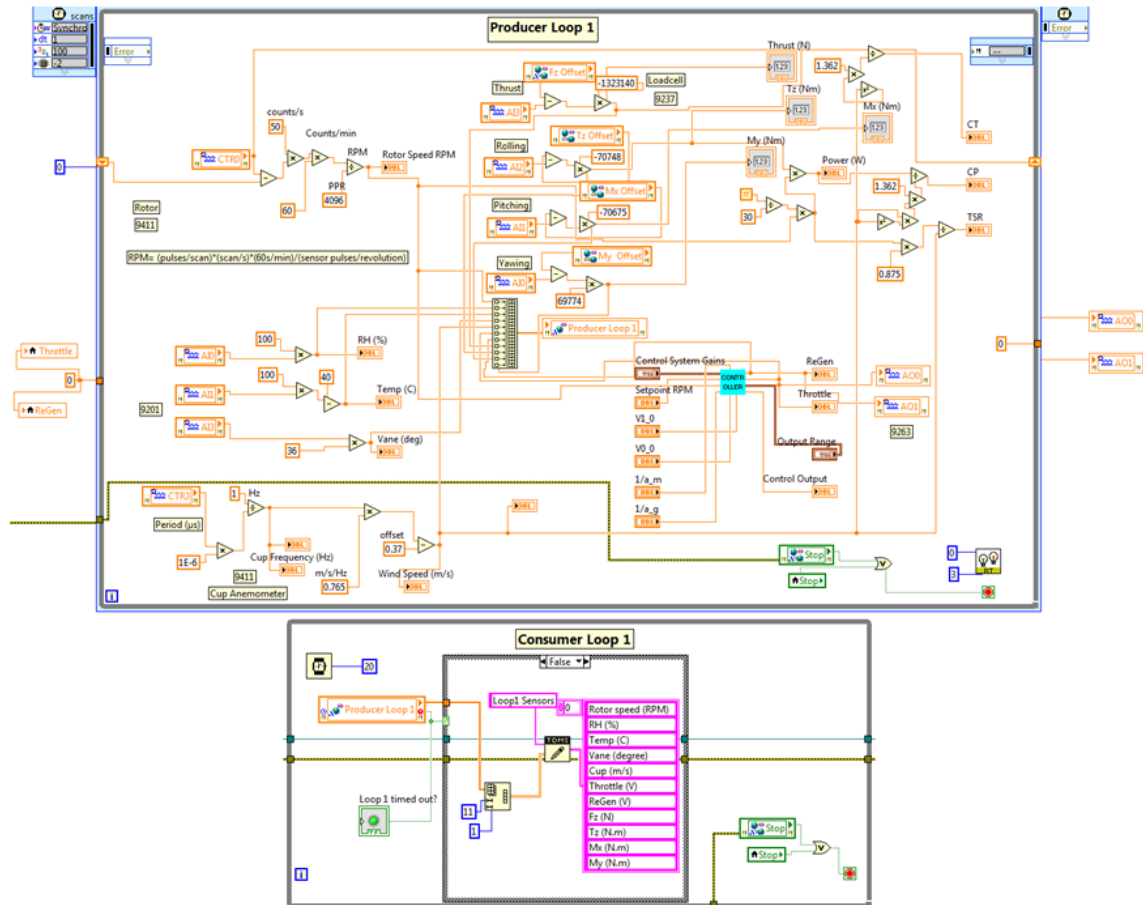


**Figure 70.** Producer/consumer loop one

The following steps can be followed to interface the test rig using the developed GUI shown in Figure 27:

1. Power the CRIO and other subsystems (as will be explained in 4.10.2).
2. Connect the CRIO to the host PC using the Ethernet cable.
3. Open NI Measurement and Automation Explorer (MAX) and confirm that the CRIO is detected under ‘Remote Systems’.

4. On the block diagram, go to the TDMS open VI and define the file path. On the front panel (GUI), set the TDMS operation to 'create'. This will create a .tdms file to be logged on the CRIO.
5. Click 'Run' to launch the application. All the loops described earlier will be executed in parallel (a priority will be given to the timed loop). This GUI is primarily designed to provide the operator with an interface to monitor the operating parameters as well as to adjust control systems' gains and setpoints when necessary. Hence, speed and yaw control systems are the only sections that might require input(s) from the user. Serial communication settings for the serial devices (i.e. ultrasonic anemometer and pressure sensor) are pre-defined and can be altered if the corresponding sensors are programmatically changed.
6. Click 'Stop'. This stop action will stop all applications running under this main program. Loop timed out LEDs indicate whether loops are executed properly. 'Error Out' is wired to the TDMS close VI, which closes the .tdms file you created, when the program is terminated. 'Code Out', 'Source out', and 'No Error/Error' icons, used within a simple error handler VI, indicate whether an error occurred. If error occurred, these icons return description of the error. This information is particularly useful when contacting National Instruments service support to troubleshoot any potential issue.
7. Open Max once again, under 'Remote Systems', right-click on the CRIO and click file transfer to transfer the .tdms file from CRIO to the host PC.
8. Power off the CRIO and other subsystems (as will be explained in 4.10.2).

- Extract required data for further processing using the MATLAB script developed to post-process experimental data.

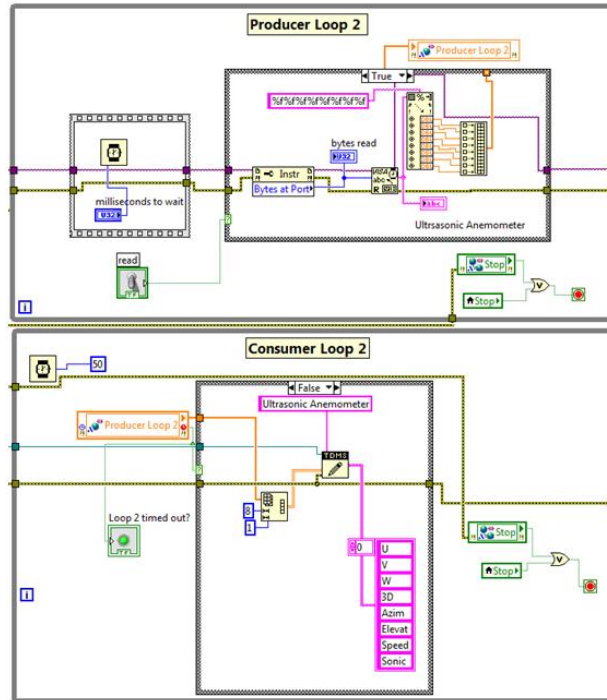


**Figure 71.** Producer/consumer loop two

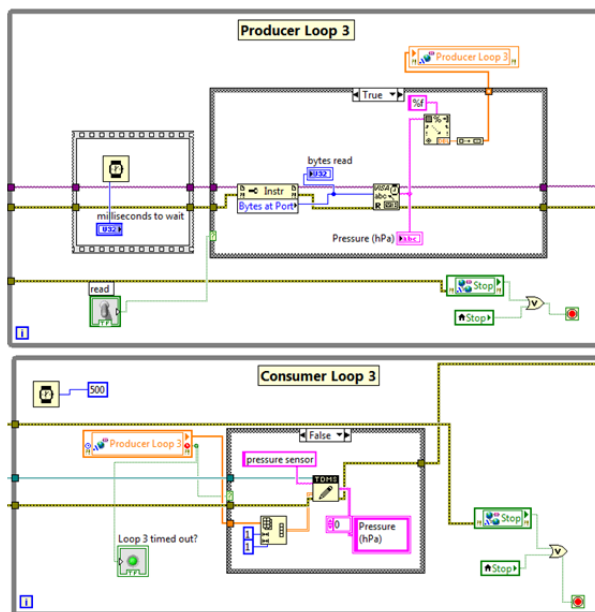


**Figure 72.** Producer/consumer loop three

## **B.2 Control Cabinet (CTRL) Interface Work Instruction**

Control cabinet interface of the test rig is depicted in Figure 73. Prior to outlining a step-by-step procedure of how to use this interface, two main safety switches will be introduced in this section, namely: battery bank disconnect switch and turbine switch.

Battery bank disconnect switch (shown top-left), which is a 350 A continuous current capacity single pole, single throw (SPST) switch, should be used to connect/disconnect the battery bank to/from the rest of the electrical system. Operators need to make sure that this switch is turned off during storage or while work is being done on the electrical system (e.g. modifying the CRIO modules' integration, wind sensor installation, etc.).

Turbine switch (shown on top-right), which is a 350 A continuous capacity double pole, single throw (DPST) switch, has two modes: fly mode (off) and park mode (on).

Throughout normal operation or storage, this switch must be kept off. In case of an emergency, when all other controls (i.e. regenerative braking, passive pitch mechanism, yaw control, software-based stop switch) and frictional resistance fail, this switch must be turned on (park). In park mode, this switch essentially shorts out all three phases of the generator. When activated in high speeds, this emergency action can lead to structural and physical damage to the turbine components.

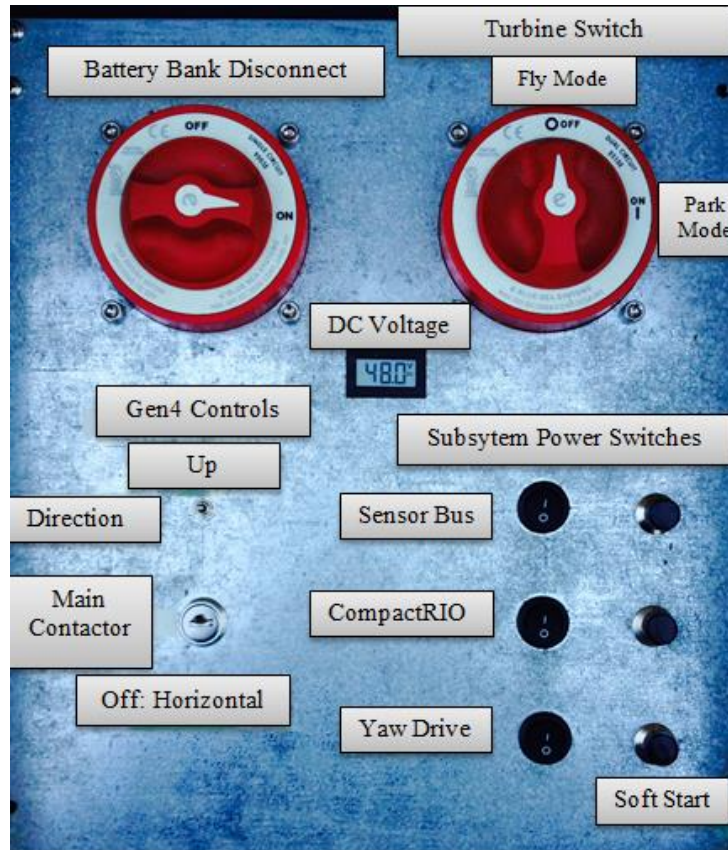


**Figure 73.** Control cabinet interface

To perform a typical operation, below procedure can be followed by the operator:

1. Turn on the battery bank disconnect SPST switch. The DC voltage meter indicates the actual battery bank voltage level. If below 48 VDC, battery bank charger, shown in Figure 19 (b), can be used to ensure efficient power distribution to the instrumentation as well as to maintain sufficient battery state of charge.
2. Use subsystem power switches to deliver proper power to individual subsystems. These subsystems are divided into CRIO, yaw drive, and sensor bus, which is responsible to power all the instrumentation except the CRIO and yaw drive. The soft start buttons (shown bottom-right) must be used before any of these subsystem power switches are activated.

3. On the Gen4 controller section of the interface, turn on the main contactor using the key provided with the test rig key set.
4. Turn the direction vertical toggle switch upward to dictate the spin direction to the controller.
5. Run the LabVIEW GUI to start the controlled operation of the turbine system and data acquisition (as explained in 4.10.1).
6. Stop the LabVIEW GUI using the main stop button.
7. Open NI Measurement and Automation Explorer (MAX) from the host Laptop's desktop. Under the Remote Systems, right click on the CRIO detected and select File Transfer. Transfer the TDMS file logged to the CRIO disc to the host desktop.
8. Put the direction toggle switch back in neutral position.
9. Turn off the main contactor (horizontal).
10. Use the soft start again, this time to power off each of the subsystems.
11. Turn off the battery bank disconnect switch. Before closing the cabinet, make sure all the switches are properly turned off.